Ultrasound-Responsive Microcapsules for Localized Drug Delivery Applications

Rachel Diane Field

Submitted in partial fulfillment of the
requirements for the degree of
Doctor of Philosophy
under the Executive Committee
of the Graduate School of Arts and Sciences

COLUMBIA UNIVERSITY

2022

Abstract

Ultrasound-Responsive Microcapsules for Localized Drug Delivery Applications

Rachel Diane Field

Over the last six decades, the field of drug delivery has advanced considerably, from sustained oral release technology to pH-responsive polymers. Innovation in the space has progressed alongside the development of new categories of drugs, as well as improvements in electronics and material science which have enabled new modalities of external stimulation. Nevertheless, the traditional challenges of drug delivery persist, including the need to reduce off-target toxicity, minimize invasiveness of administration, and bypass biological barriers; these challenges are particularly apparent for drug delivery applications in difficult-to-reach areas of the body, such as tumors or areas beyond the blood-brain barrier. Furthermore, as therapeutics become more targeted, the need for corresponding delivery methods becomes even more vital to ensure treatment effectiveness with minimal side effects. In this dissertation, we aim to demonstrate a new strategy for on-demand and localized drug delivery which is easy to fabricate and delivers a large payload relative to device size, is responsive to external stimulation for triggered release, and can be integrated into a system for real-time actuation during a physiological process.

In Aim 1, we developed a microfluidic fabrication technique for making biphasic microcapsules loaded with model drug. This method relied on microfluidic droplet methods, with sufficient interfacial tension between two on-chip phases to cause droplet formation. Typically, these systems rely on an aqueous-oil interface for sufficient interfacial tension; to fabricate a

biocompatible microcapsule, we formed biphasic microcapsules composed of an aqueous-based inner and outer phase, without an oil intermediate phase, with aqueous two-phase system properties. Additionally, we incorporated on-chip photopolymerization, designing the microfluidic chip and light source to minimize refracted ultraviolet exposure. The resulting drug-loaded microcapsules were stable, with minimal background leakage. This fabrication technique can produce a high-throughput supply of monodisperse microcapsules, which can be modified for a variety of therapeutic payloads and easily injected in targeted region in the body.

In Aim 2, we adapted these drug-loaded microcapsules for ultrasound-triggered release. Focused ultrasound (FUS) is a minimally-invasive method of stimulating release from a device, which can penetrate deep within the body and is compatible with a variety of materials; when applied at sufficient intensity and duration, it can induce heating, cavitation, or both. We tuned the applied ultrasound parameters to minimize temperature increases in surrounding tissue phantoms, while inducing steplike release profiles from the microcapsules over the course of multiple cycles of pulsed FUS. Under these applied conditions, we detected acoustic signatures consistent with inertial cavitation and visually observed structural breakdown of the microcapsules corresponding to cavitation-related effects. This release strategy is highly targeted, inducing drug release from microcapsules within a narrow focal area with minimal risk to surrounding tissue.

Finally, in Aim 3, we performed *in vitro* demonstrations of drug-loaded actuators, as initial demonstrations towards a system of integrated sensors, actuators, and adaptive learning algorithms for closed-loop control over physiological processes involved in wound healing. We experimented with both the aforementioned microcapsules and with a liposome-loaded scaffold as drug-loaded

actuators, and tested both actuators with three ultrasound transducers which offered a range of portability, intensity ranges, and imaging capacities. Next, we developed *in vitro* testing setups incorporating the actuators with either a cell monolayer or a three-dimensional cell construct, mimicking a wound site, and validated ultrasound-triggered drug-release with minimal cell damage. To demonstrate cell uptake of the released therapeutic agents, we modified the microcapsules' payload, performed the *in vitro* release experiments, and then observed correlating cell response over the following week of culturing. These demonstrations have provided guidance towards a more integrated system, which will validate the impact of the localized actuators in stimulating enhancing wound healing rates. More broadly, the eventual integrated system, incorporating both sensors and the adaptive algorithm, will be able to sense and respond to physiological changes within a wound in real-time.

This work explores how wireless, deep-tissue devices coupled with external control modalities will facilitate interventions with high spatiotemporal accuracy; when combined with sensing and regulating algorithms, it will empower real-time monitoring and interventions in physiological processes. Aim 1 focused on the fabrication of such implantable microcapsule devices and Aim 2 demonstrated a method for triggering the devices using an external control modality. In Aim 3, we investigated a use case for these microcapsules to promote rapid wound healing, alongside flexible electronics, sensors, and additional actuators. To provide additional context on implantable microdevices and biocompatibility, we provide a framework for designing medical microrobotics in Appendix I and an application of a thermally-responsive hydrogel coating in Appendix II. Overall, the sum of this work illustrates the potential impact of soft

microdevices for localized and on-demand applications, towards a future of spatiotemporally-targeted biological interventions.

Table of Contents

List of Figures

List of Tables

Acknowledgments

Thank you to my advisor, Dr. Samuel Sia.

He has given me guidance, time, space, course-corrections, inspiration, and motivation.

Thank you to my committee – Dr. Clark Hung. Dr. Helen Lu, Dr. Parag Chitnis, and Dr. Milan Stojanovic.

They have given me their time, expertise, and guidance.

Thank you to my cohort -- Dr. Priya Andanukamaran, Dr. Alex Colburn, and Dr. Siddarth Arumugam.

They have done heavy lifting -- in lab, to/from apartments, and emotionally – to make this experience so much lighter.

Thank you to my lab partner, Margaret Jakus.

In addition to being a creative and persistent research collaborator, she has been generous with her friendship, her stories, her time, and her baked goods.

Thank you to the rest of my labmates, past and present -- Dr. Samiksha Nayak, Dr. Nicole Blumenfeld, Vira Behnam, Harshit Harpaldas, Abigial Ayers, Kelia Human, Terry Chern, Darragh Kennedy, and Autumn Greco.

They have given me their help, encouragement, and pop culture knowledge.

Thank you to the masters and undergraduate students who I have had the pleasure of working with – Kavitha Prasannan, Audrey Lee, Matthew Wester, Emily Chen, Christine Sison, Eve Fishinevich, and Sajan Bar.

They have given me their patience as I learn what it means to mentor.

Thank you to Helene Montagna and to the Columbia BME department staff for all of their assistance.

They have been so supportive over the years, addressing innumerable quandaries and making this process so much smoother.

Thank you to Dr. Katherine Reuther, Dr. Aaron Kyle, and Dr. X. Edward Guo.

In allowing me the opportunities to TA their classes, they gave me the opportunities to grow and to remember how I ended up here.

Thank you to my fellow student collaborators on the DARPA BETR project, including Jack Rogot, Lauren Lisiewski, Xiaoyu Chen, Jakub Jadwiszczak, Prashant Muthuraman, and Georgios Theocharidis.

They have generously taught me so many new skills and learned alongside me, as we pursued ambitious project aims in an interdisciplinary space.

Thank you to the TL1 Precision Medicine team, particularly Dr. Henry Ginsberg and Dr. Krzysztof Kiryluk.

They have expanded my opportunities during my graduate studies, introduced me to a diverse peer group, and prepared me for challenges ahead.

Thank you to my TL1 co-advisor, Dr. Azra Raza.

She has shown me the humanity in science.

Thank you to my friends – in California, New York, Boston, and elsewhere.

They have given balance to my daily life, and celebrated the victories, minor and major.

Thank you to my fiancé.

He has supported me through every step of these years, from applications through defense, and patiently provided endless feedback and advice. Being with him has made everything more joyous, and ensured many hours of thoughtful playlists.

Thank you to my family.

They have never doubted that this is where I should be. They encouraged, listened, and reminded me to never lose perspective.

Rachel Diane Field

September 2021

New York City

Dedication

This is for my parents,

who read me

Oh, the Places You'll Go!

so long ago.

Chapter 1: Introduction

The goal of this thesis is to illustrate a method for wireless, deep-tissue drug delivery, which enables on-demand therapeutic distribution within a localized area of the body. We first demonstrate a scalable microfluidic technique for the fabrication of biocompatible drug-loaded microcapsules. These microcapsules respond to the application of focused ultrasound, which triggers temporally- and spatially-controlled release from the capsules. Finally, we integrate the drug-loaded capsules with other surface and implantable devices, towards a closed-loop system for addressing wound healing. The overall objective is to demonstrate a new implantable drug-loaded device, which can be loaded with a variety of therapeutics and be spatiotemporally controlled using focused ultrasound.

1.1 Advances in drug delivery systems

Effective drug delivery technology converts drug therapeutics into impactful therapies, but challenges remain with respect to many forms of disease treatment [42-45]. While current delivery methods range from oral to transdermal or interveinal, many therapeutics continue to have limitations due to risks of off-target side effects, slow onset of action, non-specific delivery, and low level of macromolecular absorption [46]. Oral and parenteral injections are the most common delivery methods; oral delivery is easy to use and has consistent transit times, but is limited due to inefficiency and low bioavailability (the fraction of administered dosages that reaches systemic circulation), while injection methods have complete bioavailability but include

risk of infection, come as a shock to the system, and have a short half-life within the blood stream [47, 48].

The introduction of the first sustained release formulation in in 1952 initiated development of the first generation of drug delivery systems, composed of a range of sustained and controlled release systems [49]. This first generation of technologies provided ‘sustained release’ solutions for oral and transdermal drug delivery, allowing patients to have once or twice per day dosing frequency for medications, an improvement from the prior three or four doses per day [50]. These delivery techniques improved ease of use and, correspondingly, patient compliance. During this era, researchers established four dominant controlled release strategies: ion-exchange, osmosis, diffusion, and dissolution [51].

During the second generation of drug delivery technology, beginning in the mid-1980s, research focused on methods for ‘smart delivery systems.’ These systems often relied upon environmentally-responsive hydrogels and other polymers, which reacted to pH or temperature within the body, or on nanoparticles, which attracted interest because of the large surface area-to-volume ratio that can be manipulated to attain a desired drug dispersion rate [52]. Additionally, consideration was paid to drug release profiles, and particularly to zero-order release profiles, which provide a steady drug concentration over time, rather than first-order release, as was typical of first-generation release drug delivery technology [49].

More recently, strategies for drug delivery have diversified, propelled alongside the diversifying therapy types including antibodies, nucleic acids, and cells, in addition to traditional small molecule drugs [45]. Furthermore, recent advances in materials engineering and electronics have introduced new techniques for external stimulation of localized drug delivery, such as improved magnetic control systems, more affordable and powerful ultrasound transducers, and a range of micro-electromechanical systems (MEMS) [53-56]. Nevertheless, the fundamental challenge of transporting and releasing the drug, passively or actively, to a target site in the body remains unresolved for many medical conditions, particularly for applications in difficult-to-reach locations, such as: a tumor deep within the body, a chronic wound site, or an area behind the blood-brain barrier [57-59].

New technologies for localized drug delivery could provide the means of wireless delivery deep within tissue. A localized and controlled release strategy may extend the active use time frame and efficacy of a drug treatment compared to traditional methods. For a given treatment type, there is a minimum effective dose, below which the drug concentration is too low for an effective therapeutic effect, as well as a toxic limit, a concentration above which the drug induces observable adverse effect; the concentration range between these values is the therapeutic window [48]. Intravenous injections typically enter the body at concentrations above the toxic limit and are rapidly cleared from the blood stream, effectively decreasing the concentration to below the minimum effective dose. In comparison, a localized delivery system that provides a method of controlled release can deliver a drug without an initial shock-level of dose and can remain at an effective concentration level for a relatively long period of time (**Fig.**

1). Moreover, by integrating a method for pulsatile or triggerable payload release, controlled drug delivery vehicles have an additional level of functionality compared to traditional delivery methods [60, 61]. The development of a viable localized delivery technology involves consideration of a variety of factors, namely: targetability to the desired delivery site; biocompatibility of the drug and carrier device, so as to evade an overwhelming immune response or effort to the clear the carrier; payload capacity within the carrier material or device; and predictability of drug release from the carrier, whether as a sustained release or in triggerable increments [46, 62].

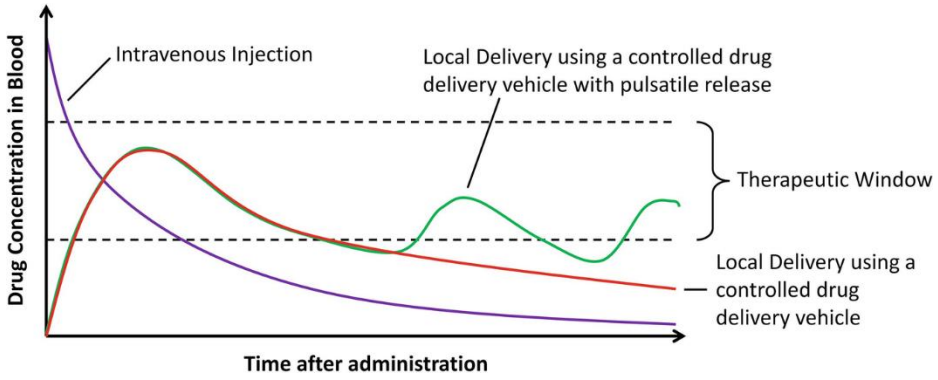

Figure 1: Comparison of drug concentration in blood over time for various methods of drug delivery (from [48], reprinted with permission).

Microcapsules, microparticles, and nanoparticles have increased in popularity as tools for targeted drug delivery in the last few decades. They can be made from a variety of materials, in various geometries; loaded with different types of drugs; designed to respond to either internal or extracorporeal stimuli; and can be steered or administered to precise locations [63-65]. While a variety of macro-scale drug delivery systems (DDS) are available for targeted payload release, micro-scale DDS are of particular interest because they can be injected directly to – and will

remain in – the region of interest and they can be designed to have controllable release characteristics, all in a noninvasive manner [63, 66].

When assessing methods of external control or stimulation of DDS, ultrasound has become a commonly-considered method because it involves a noninvasive, widely-available, low-cost tool which can be tuned for high depth of penetration and precise spatial resolution. Broadly, ultrasound is a mechanical, longitudinal wave at frequencies greater than 20 kHz which can have various effects on tissue or on implanted devices based on the material properties and ultrasound parameters [67]. Ultrasound is noninvasive, commonly accessible in standard medical settings, and has deep penetration depths compared with other noninvasive stimulation modalities [13]. Ultrasound-induced payload release from microparticles (MPs) combines the advantages of ultrasound as a method of noninvasive external control and of MPs as versatile payload carriers. Often, these are designed to be responsive to cavitation – the oscillations of gas microbubbles in an ultrasonic field. These oscillating microbubbles can cause particle rupture, increased particle porosity, and increased convective release from the particles [68, 69].

Furthermore, ultrasound can act as a control modality for ultrasound-responsive implanted devices within a drug delivery system. Three different schemes of control modality for responsive drug-loaded devices are possible: a manually controlled extracorporeal control system, an automated extracorporeal control system, and an automated internal control system (**Fig. 2**)[13]. A primary consideration is the location of the controller, the element that processes signals from sensors and sends instructions for locomotion or functionality back to the implanted

device. The controller can be either extracorporeal (outside the human body) or intrinsic (embedded within the device). Most approaches for localized drug-delivery devices rely on extracorporeal controllers as they are less constrained by space and power. Extracorporeal control is also versatile, allowing for manual intervention, as well as machine-learning algorithms for closed-loop operation (i.e., automation of the implanted device without manual intervention). On the other hand, an intrinsic controller – functionally similar to a cell, micro-organism, or organ – enables a compact and autonomous system. While extracorporeal ultrasound is currently a manual control modality, an intrinsic, or closed-loop, DDS that incorporate ultrasound as a control modality are increasingly possible. Furthermore, as improvements in machine learning for precision medicine applications expand our understanding of biomarkers, there is increasingly the capacity to analyze biological processes using fine-grained spatiotemporal data for patterns that inform diagnostic and therapeutic decisions [70-72]; as these datasets increasingly inform and integrated with DDS, it is increasingly feasible to develop a closed-loop DDS in which a triggered drug release occurs in response to locally-sensed information. Devices such as the ultrasound-responsive microcapsules are intended for eventual integration into such a closed-loop system, with algorithmically-driven release points.

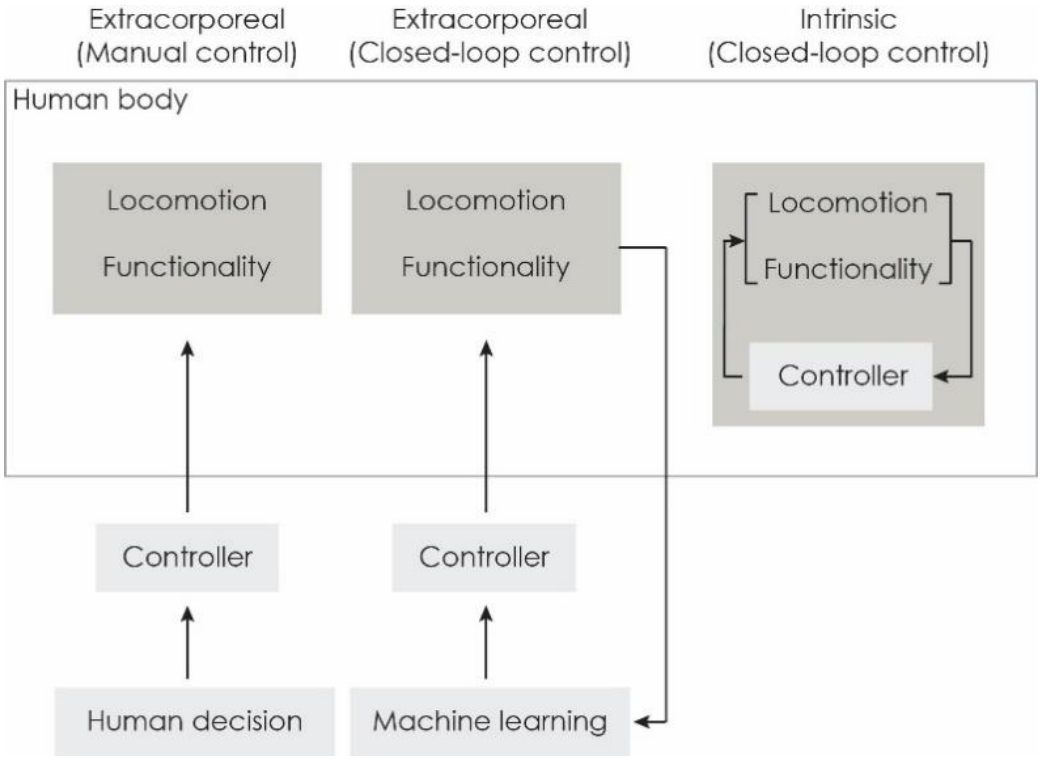

Figure 2: Mechanisms for feedback and control of a localized delivery system. Three strategies are considered, with two involving a controller outside of the body and a third strategy in which the controller mechanism is implanted within the body and/or integrated within the device (from [13], reprinted with permission).

Thus, in this thesis we aim to develop a technique for controlled, localized drug delivery and to demonstrate a relevant use case. In Chapters 2 and 3, we demonstrate a microfluidic method for fabricating drug-loaded biocompatible microcapsules which respond to ultrasonic external stimulation. In Chapter 4, we develop initial demonstrations of the microcapsules integrated within a system designed to promote wound healing with a high level of spatiotemporal control.

1.2 Outline of work

Our goal is the development of a stimulus-responsive drug delivery system that integrates into platforms for closed-loop localized interventions, in which the therapeutic device releases a dose which is dependent upon locally-sensed diagnostic information. Towards this end, we first develop a robust microfluidic fabrication method for highly drug-loaded microcapsules (Aim 1). Next, we demonstrate and refine a method of external stimulation of the microcapsules, based on resulting effects from the application of focused ultrasound (Aim 2). We then integrate this technology with sensors and other actuators to demonstrate the relevance of this technology for enabling spatiotemporally-precise interventions within a wound site, towards promoting improved healing time (Aim 3). Lastly, Appendix A summarizes a framework for considering recent advances in the medical microrobotics space, while Appendix B provides a summary of prior work developing a drug-coated balloon for localized delivery within peripheral blood vessels.

Aim 1. Microfluidic fabrication of multiphased microcapsules as base functional structures. In Aim 1, we seek to develop a robust microfluidic-based fabrication method to make biocompatible microcapsules, which can be adapted for a range of therapeutic and diagnostic applications. We first explore methods for microfluidic droplet formation and then demonstrate methods for overcoming low interfacial tension to make two-phased aqueous droplets. Finally, we demonstrate multiple polymerization methods, including dual on-chip polymerization techniques. Currently, these microcapsules can be loaded with a payload, for

potential localized drug delivery applications, with other potential loading and surface modification strategies discussed in the future works. My role in this work was the development of project conception and design, leading the experiments to develop the range of microcapsules, data analysis and synthesis of results, and writing the manuscript.

This work is completed. A manuscript that incorporates a subset of the microfluidic techniques described herein has been submitted for peer review. We continue to research variations on the microcapsules, as described in future works. Additionally, I was awarded a TL1 predoctoral fellowship in relation to this work (TL1TR001875).

Aim 2. Ultrasound-stimulated drug release from microcapsules for pulsatile and localized delivery. In Aim 2, we seek to develop a method of releasing a drug payload from a targeted microcapsule by applying focused ultrasound, for localized drug delivery with precise spatiotemporal control. First, we set up a benchtop system for ultrasound generation and monitoring, and then experiment with exposing microcapsule samples to a wide range of ultrasonic test parameters. We monitored the samples during applications of pulsed focused ultrasound (FUS), to detect when the two methods of material response to ultrasound – cavitation and thermal – occur. Next, we tested cumulative release and release rate of microcapsules under a range of parameters, to optimize for maximum responsiveness with minimum needed amount of ultrasound applied. My role in this work was the development of project conception and design, assembly of relevant ultrasonic equipment, running experiments for optimizing ultrasonic conditions, data analysis and synthesis of results, and writing the manuscript.

This work is completed. The findings from this work were included in the manuscript referenced in Aim 1, which is submitted for peer review. We have also prepared a review manuscript discussing micro- and nano-material design for ultrasound-triggered drug delivery, which is in the final stages of revision. Additional FUS-related demonstrations are planned as future work within the research group.

Aim 3. Integration of ultrasound-responsive devices, including microcapsules, for initial demonstration towards a closed-loop method of improving wound healing. The responsive microdevices have the potential for closed-loop integration of sensing and actuating devices within a small volume, allowing for highly localized monitoring and interventions. In Aim 3, we seek to provide initial demonstrations of such a system, with a use case of reducing healing time for chronic or blast wounds. Within an *in vitro* test setup, we assess the effect of multiple ultrasound transducers on the system's sensors and actuators, along with testing the effectiveness of the actuators when in the integrated system. Additionally, we test effect of the microcapsules and of direct ultrasound on a mock-wound cell construct. Finally, we fabricate the actuators with biologically-relevant payloads and in a sterile environment, and test for any adjustment of drug release profile. My role in this work was to contribute towards experimental design for the *in vitro* experiments, to develop the *in vivo* protocol design, and complete the preparatory practice procedures.

Work on this aim is ongoing; we are planning a publication focused on the *in vitro* and microcapsule-related *in vivo* findings, and a publication planned upon completion of the complete *in vivo* demonstration.

Appendix A: Soft medical microrobots: Design components and system integration. In Appendix A, we discuss recent advances in medical microrobots and the relevant design parameters to consider for full functionality of such devices. In particular, we outline the primary four considerations in the design and fabrication of medical microrobots: locomotion, feedback and control, functionality, and biocompatibility. This work resulted in a published co-first author review paper: *Field, R. D., *Anandakumaran, P. N., & Sia, S. K. (2019). Soft medical microrobots: Design components and system integration. Applied Physics Reviews, 6(4), 041305.

*Denotes equal contribution from authors

Appendix B: Responsive hydrogel coatings of catheter balloons for peripheral artery disease application. Drug coated balloons (DCBs) have become a common treatment method for peripheral artery disease, particularly in small blood vessels (<4 mm diameter). However, DCBs have significant drug wash-off between insertion and reaching the intended use site, which can lead to dangerous side effects including embolisms and other cytotoxicity concerns. Therefore, we aim to develop a coating for DCBs that enables efficient release of anti-proliferative drugs “on-demand”, i.e., release of the drug when it is desired, and only during the

time the release is triggered. To accomplish this, we fabricate an advanced drug-releasing balloon catheter with an electronically-actuated system consisting of stretchable electronics (that serve as localized heating elements) and thermo-responsive hydrogel membranes, and performed initial *in vitro* demonstrations. This work provided an opportunity to develop polymerization techniques and to test external stimulation and control methods.

Chapter 2: Microfluidic fabrication of two-phase microcapsules.

2.1 Background

Microparticles and microcapsules have been in use for several decades, with particular prevalence in flavor and food protection and in pesticide applications, as well as, increasingly, for biomedical applications [73, 74]. Microparticles are an attractive method for controlled drug delivery. They can be fabricated in a variety of sizes and from a variety of biodegradable materials with tunable properties [65], show improved circulation time compared to more traditional delivery techniques such as intravenous infusion [75], and can be layered to protect the internal payload and to enable multiple drug loading [76]. Cavitation-responsive microparticles may be a suitable strategy for wireless drug delivery systems (DDS) which can provide targeted delivery to deep tissue areas. However, there are many considerations for such devices, including the need for higher encapsulation efficiency, minimal or controlled background release, biocompatibility, and precise control of payload release at ultrasound parameters safe for *in vivo* use.

Droplet microfluidics is an increasingly common technique for fabricating microcapsules due to the low necessary reagent volume, high control of each individual droplet, and high surface area to volume ratio of the droplets. Furthermore, for implantable biomedical applications, the spherical geometry produced by microfluidic fabrication techniques tends to elicit a minimal immune response [13]. Thus, for our intended application purpose of

controllable localized delivery, a drug-loadable spherical microcapsule provides a useful fundamental base structure and microfluidic fabrication provides a method for producing microcapsules of consistent geometry with very efficient material usage.

As is broadly applicable in microfluidics, droplet formation in the microscale occurs in a low Reynold's number regime. Moreover, droplets occur because of fluid instabilities, as an immiscible fluid enters another fluid, with the former known as the dispersed phase and the latter as the continuous phase; droplets typically form according to the regimes of: tip-streaming, tip-multi-breaking, jetting, dripping, and squeezing [77-79]. Droplets form as the dispersed and continuous phases meet at an immiscible interface, the interface deforms into an unstable stage, and then the unstable interface fragments into disconnected droplets. To best understand the interfacial tension, the capillary number, *Ca* – the ratio of viscous to capillary or interfacial forces – is calculated as:

$$Ca = \frac{U\mu}{\gamma}$$

where U is the flow velocity, γ is the interfacial surface tension, and μ is the fluid viscosity. In most of microfluidic systems, $10^{-3} < Ca < 10$. For droplet formation, the ratio of $Ca_{dispersed}$: $Ca_{continuous}$ provides insights into which of the aforementioned droplet regimes will occur on-chip, or whether there will be a lack of equilibrium [80].

For our intended application of drug-loaded microcapsules, we have pursued methods for a core-shell-based geometry, so that the core (or inner phase) can be loaded with a relatively

large drug payload, relative to the volume, and the shell (or outer phase) assists in stabilizing the microcapsule, for easier to transport and for the ability to store the microcapsules for multiple days without complete drug leaching. Given the need for biocompatibility, we have pursued the fabrication of an all-aqueous microcapsule, which provides a level of novelty to the fabrication design. While water/oil methods for microfluidic droplets are quite common, there are very few demonstrations of water/water/oil methods in microfluidic systems, due to the low interfacial tension between sequential aqueous phases; many of the prior demonstrations have incorporated an active method of perturbation, such as a pulsatile pump or solenoid [79]. In contrast, our method relies on aqueous two-phase separation behavior to form water/water/oil droplet without relying on perturbation.

2.2 Methods

2.2.1. Bulk material analysis

2.2.1.A. Material properties of solutions of interest

We measured the respective viscosity of materials of interest, listed in **Table 1**, using viscometers in sizes 2 and 2B (Cannon; State College, PA). Furthermore, we considered molecular weight and hydrophobicity based on available documentation.

Phase	*Material*	*Catalog #*	*Manufacturer*
Dispersed	Ultrapure (UP) MVG alginate	4200121	Pronova
	PEGDA 10k Da	26279	Polysciences
	PEGDA 575 Da	437441	Sigma-Aldrich
	dextran from Leuconostoc spp.,Mr 450,000-650,000	31392	Sigma-Aldrich
	FITC-dextran, 20k Da	15759	Polysciences
	Poly(vinyl alcohol), MW 13000-23000, 87-89% hydrolyzed	363170	Sigma-Aldrich
Continuous phase	Sunflower seed oil	S1929	Spectrum Chemical
	Mineral oil	AC415080010	Sigma-Aldrich
	Light mineral oil	8042-47-5	Sigma-Aldrich
	Fluorinert FC-40	F9755	Sigma-Aldrich
Surfactant	Span 80	S6760	Sigma-Aldrich

Table 1: Considered materials for microfluidic-based fabrication of microcapsules.

2.2.1.B. PEGDA pore size

To calculate the expected pore size of Poly(ethylene glycol) diacrylate (PEGDA) at a range of molecular weights and concentrations, as listed in **Table 2**, we prepared sample discs of PEGDA at both 10k Da and 575 Da molecular weights, in a range of concentrations, with 10 mm diameter and 70 µL volume. We added 2.5% w/v Darocure 2959 to each sample. We used a custom-made PDMS well to contain these samples while exposing the samples to UV light, at an

intensity of 1008 W/sec for 5 seconds, with a 1” spacer between the UV light source and the sample.

Sample #	***PEGDA 575 Da (%)***	***PEGDA 10k Da (%)***
1	50	
2	30	
3		40
4		20
5		10
6	30	20
7	15	20
8	30	10
9	15	10

Table 2: Compositions of PEGDA prepared for material testing

Once the samples were photopolymerized (DI), we allowed samples to soak in 1000 µL of deionized water in a 24-well plate for 24 hours, to wash off all unpolymerized monomers on the surface. We changed the water 6 times to facilitate removal of all unpolymerized material. After the washing period, we pipetted out wash water from wells and placed the prepared plate in the vacuum desiccator overnight to allow for drying. We kept samples in a vacuum for up to 24 hours to ensure complete drying. We then weighed each sample to determine the dry weight, and subsequently placed the samples into fresh wells in a 24-well plate with 400 µL DI water. Then, at designated timepoints, we removed each sample from the surrounding solution, removed

excess water by blotting with a Kimwipe, and weighed the PEGDA disc. Each disc was then placed back into a well of DI water, and the weighing procedure was repeated twice a day for three days, until an equilibrium was confirmed, to observe swelling of the PEGDA structures over time.

For the diffusion assessment, we prepared samples by weighing out 10 µg of 20k Da FITC-dextran into 1.5 mL tubes, and then adding 500 µL of each solution from above into a corresponding FITC-filled tube. We prepared photopolymerized samples of each PEGDA composition by pipetting 70 µL of solution into a 10mm PDMS well and exposing the sample to ultraviolet (UV) light for 5 seconds, with exposure occurring at 1" distance from UV lamp and at 42% intensity. We then placed each sample into a well of a 24-well plate with 1 mL of DI water and allowed for 30 minutes of leaching. We replaced the DI water and then collected the sample at the t = 0 timepoint, replacing the volume collected with fresh DI water; we repeated this sampling step at each timepoint (1, 2, 4, 20, 24, 48, 72, and 96 hours). For each timepoint, we collected 3x 50 µL samples of the surrounding solution and placed the samples into a 284-well plate for plate reading.

2.2.1.C. Aqueous phase separation

To assess what concentration of the dextran and Polyethylene Glycol Diacrylate (PEGDA) phases are necessary to achieve two-phase separation rather than a single phase, we pipetted stock samples of dextran (15% dextran 500k Da) and PEGDA (30% PEGDA 575 Da or

40% PEGDA 10k Da) into 200 µL flat cap tubes at a range of ratios (**Table 3**). We stored the samples for 24 hours at room temperature, in a dark environment, and then visually assessed for phase separation.

a dextran 500k Da and PEGDA 575 Da

Initial dextran Concentration	Initial PEGDA 575 Da Concentration	Initial dextran volume (µL)	Initial PEGDA 575 Da Volume (µL)	Effective dextran Concentration	Effective PEGDA 575 Da Concentration
0.15	0.5	50	50	0.075	0.25
0.15	0.5	45	55	0.0675	0.275
0.15	0.5	40	60	0.06	0.3
0.15	0.5	35	65	0.0525	0.325
0.15	0.5	55	45	0.0825	0.225
0.15	0.5	60	40	0.09	0.2
0.15	0.5	65	35	0.0975	0.175
0.15	0.5	70	30	0.105	0.15
0.15	0.25	50	50	0.075	0.125
0.15	0.25	45	55	0.0675	0.1375
0.15	0.25	40	60	0.06	0.15
0.15	0.25	35	65	0.0525	0.1625
0.15	0.25	55	45	0.0825	0.1125
0.15	0.25	60	40	0.09	0.1
0.15	0.25	65	35	0.0975	0.0875
0.15	0.25	70	30	0.105	0.075
0.3	0.5	50	50	0.15	0.25
0.3	0.5	45	55	0.135	0.275
0.3	0.5	40	60	0.12	0.3
0.3	0.5	35	65	0.105	0.325
0.3	0.5	55	45	0.165	0.225
0.3	0.5	60	40	0.18	0.2
0.3	0.5	65	35	0.195	0.175
0.3	0.5	70	30	0.21	0.15
0.075	0.25	50	50	0.0375	0.125
0.075	0.25	45	55	0.03375	0.1375
0.075	0.25	40	60	0.03	0.15
0.075	0.25	35	65	0.02625	0.1625
0.075	0.25	55	45	0.04125	0.1125
0.075	0.25	60	40	0.045	0.1
0.075	0.25	65	35	0.04875	0.0875
0.075	0.25	70	30	0.0525	0.075
0.0375	0.25	50	50	0.01875	0.125
0.0375	0.25	45	55	0.016875	0.1375
0.0375	0.25	40	60	0.015	0.15
0.0375	0.25	35	65	0.013125	0.1625
0.0375	0.25	55	45	0.020625	0.1125

0.0375	0.25	60	40	0.0225	0.1
0.0375	0.25	65	35	0.024375	0.0875
0.0375	0.25	70	30	0.02625	0.075

b dextran 500k Da and PEGDA 10k Da

Initial dextran Concentration	Initial PEGDA 10k Da Concentration	Initial dextran volume (µL)	Initial PEGDA 10k Da Volume (µL)	Effective dextran Concentration	Effective PEGDA 10k Da Concentration	Initial dextran Concentration
0.075	0.4	50	50	0.0375	0.2	3.75
0.075	0.4	45	55	0.03375	0.22	3.375
0.075	0.4	40	60	0.03	0.24	3
0.075	0.4	35	65	0.02625	0.26	2.625
0.075	0.4	55	45	0.04125	0.18	4.125
0.075	0.4	60	40	0.045	0.16	4.5
0.075	0.4	65	35	0.04875	0.14	4.875
0.075	0.4	70	30	0.0525	0.12	5.25
0.075	0.2	50	50	0.0375	0.1	3.75
0.075	0.2	45	55	0.03375	0.11	3.375
0.075	0.2	40	60	0.03	0.12	3
0.075	0.2	35	65	0.02625	0.13	2.625
0.075	0.2	55	45	0.04125	0.09	4.125
0.075	0.2	60	40	0.045	0.08	4.5
0.075	0.2	65	35	0.04875	0.07	4.875
0.075	0.2	70	30	0.0525	0.06	5.25
0.0375	0.4	50	50	0.01875	0.2	1.875
0.0375	0.4	45	55	0.016875	0.22	1.6875
0.0375	0.4	40	60	0.015	0.24	1.5
0.0375	0.4	35	65	0.013125	0.26	1.3125
0.0375	0.4	55	45	0.020625	0.18	2.0625
0.0375	0.4	60	40	0.0225	0.16	2.25
0.0375	0.4	65	35	0.024375	0.14	2.4375
0.0375	0.4	70	30	0.02625	0.12	2.625
0.075	0.1	50	50	0.0375	0.05	3.75
0.075	0.1	45	55	0.03375	0.055	3.375
0.075	0.1	40	60	0.03	0.06	3
0.075	0.1	35	65	0.02625	0.065	2.625
0.075	0.1	55	45	0.04125	0.045	4.125
0.075	0.1	60	40	0.045	0.04	4.5
0.075	0.1	65	35	0.04875	0.035	4.875

0.075	0.1	70	30	0.0525	0.03	5.25
0.0375	0.1	50	50	0.01875	0.05	1.875
0.0375	0.1	45	55	0.016875	0.055	1.6875
0.0375	0.1	40	60	0.015	0.06	1.5
0.0375	0.1	35	65	0.013125	0.065	1.3125
0.0375	0.1	55	45	0.020625	0.045	2.0625
0.0375	0.1	60	40	0.0225	0.04	2.25
0.0375	0.1	65	35	0.024375	0.035	2.4375
0.0375	0.1	70	30	0.02625	0.03	2.625

Table 3. Concentrations of dextran 500k Da and PEGDA 575 Da (a) or 10k Da (b) tested during bulk phase separation experiments.

2.2.2. Microfluidic droplet formation

2.2.2.A. Microfluidic chip design and fabrication

Positive microfluidic chip molds were designed using SolidWorks CAD Software (Solidworks; Concord, MA) and fabricated using a Objet30 Pro 3D printer (Stratasys; Plymouth, MN). The molds were constructed from VeroWhite resin with SUP706 support material; the support material was removed post-printing by placing the molds into an agitating bath of caustic acid for 4 hours, and then baked in an oven at 65˚C for 1 hour.

The Polydimethylsiloxane (PDMS) prepolymer base of Sylgard 184 (Dow Corning; Midland, MI) was combined with the curing agent at a weight ratio of 8:1. After hand mixing and 5 minutes of centrifuging at 3000 rpm, the PDMS was poured into the aforementioned mold, degassed for 45 minutes, and then cured for 3 hours at 65˚C. Once fully cured, the cured PDMS was then removed from the mold, the inlet and outlet holes were punched with a 1.25 mm biopsy

punch, and the chip was bonded via oxygen plasma treatment to a cleaned glass slide with a 100 µm layer of PDMS that had been deposited by spin coating. The bonded microfluidic chip was then heated at 90˚C for 1 hour.

2.2.2.B. Droplet fabrication

To determine a rough guide for appropriate flow rates, we flowed in both dispersed and continuous phases at a variety of concentrations to a microfluidic chip with a basic flow-focusing chip design; we assessed flow rates of 0.2, 0.5, 1, 5, 10, 25, 50, and 100 µL/min for both phases of the chip.

2.2.3. Biphasic droplet fabrication

All channels had square cross-sections. The channel dimensions for the inlet channels were 500 microns on each side, while the nozzle sides were 400 µm; the serpentine outlet channel was 600 µm on each side.

During droplet formation, we observed the microfluidic chips in real time on an inverted fluorescent microscope with a DFC7000 camera (Leica Microsystems; Buffalo Grove, IL). The discrete phases entered the PDMS chip via tygon tubing.

2.2.4. Polymerization of droplets into microcapsules

We relied on free-radical-initiated chain polymerization to photopolymerize the PEGDA phase and, thus, added 2.5% w/v 2-Hydroxy-4′-(2-hydroxyethoxy)-2-methylpropiophenone (Irgacure 2959, Sigma Aldrich; St. Louis, MO) [81]. To crosslink the PEGDA phase of the dextran-PEGDA microcapsules, we applied UV over the serpentine area of the microfluidic chip; the chip was oriented so that the glass slide portion of the chip was closest to the UV source. To minimize photopolymerization of the PEGDA by ambient light and to eliminate any safety risks from viewing UV light, we applied the UV light only while running the microfluidic chip within an enclosed black plastic container. The device power was set to a 10% of the total available power of 30 W/cm^2, and increased until beads were observed to polymerize. We confirmed sufficient polymerization by performing three washes of the resulting microcapsules with DI water and soaking the samples in a water-filled petri dish; droplets which polymerized into microcapsules sufficiently were stable after the washing and soaking process.

To more precisely control the area and time of photopolymerization on-chip, we designed a custom-constructed ultraviolet (UV) light system featuring an SBM-120-UV light-emitting diode (LED) array with a surface emitting area of 12 mm^2 (Luminus; Sunnyvale, CA). We controlled the custom UV LED board with an Uno Rev3 (Arduino; Somerville, MA) and continuously monitored the LED temperature using a mounted 47k NTC thermistor (Murata Electronics; Smyrna, GA). The LED and associated circuitry (**Table 4**) was housed in a custom

laser-cut enclosure designed to fit over the microfluidic chip while on an inverted microscope stage, with an incorporated heat sink.

Part Name	*Quantity*	*Description*	*Supplier*	*Supplier Part Number*
Luminus SBM-120-UV	1	LED UV emitter with star array	Mouser	896-SBM120UVR34H365
Mean Well HLN-60H-15A	1	Adjustable power supply	Mouser	709-HLN60H-15A
ATSEU-077D-C1-R0	1	Heat sink	Mouser	984-ATSEU-077D-C1-R0
Inline power switch	1	DPST rocker switch in casing	Amazon	n/a
Qualtek 311007-01	1	AC power cord	Mouser	562-311007-01
NHD-0216K3Z-NSW-BBW-V3	1	LCD I2C display	Digikey	NHD-0216K3Z-NSW-BBW-V3-ND
Murata Electronics NXRT15WB473FA3A016	1	47k NTC thermistor	Digikey	NXRT15WB473FA3A016
STMicroelectronics L78S75CV	1	Linear regulator for arduino	Digikey	497-14164-ND
Vishay K104K15X7RF5TL2	1	Smoothing capacitor for linear regulator (0.1 µF ceramic capacitor)	Digikey	BC1084CT-ND
Arduino Uno Rev3	1	Arduino Uno for monitoring	Arduino	A000066
Stackole RSMF2JTR100	1	Shunt resistor for current measurement (0.1 Ω, 2W)	Digikey	RSMF2JTR100CT-ND
Emitter switch	1	DPST rocker switch	n/a	
10 kΩ Resistor	1	For thermistor voltage divider	Digikey	
2.7 MΩ Resistor	2	For shunt measurement voltage divider	Digikey	
1 MΩ Resistor	2	For shunt measurement voltage divider	Digikey	

Table 4: Required electronic components for the construction of circuit to control and power the 144 mm^2 surface LED UV lamp.

2.2.5. Microcapsule characterization and tuning

After on-chip fabrication, microcapsules flowed into a 35 mm diameter petri dish at the outlet, which was prefilled with deionized (DI) water, so that the microcapsules sank out of the oil phase and into the DI water. We then repeatedly washed the microcapsules with DI water, to remove as much oil and surfactant as possible.

We characterized the resulting microcapsules for overall diameter and inner phase diameter using ImageJ image analysis software (U. S. National Institutes of Health; Bethesda, MD). Additionally, the structure of the beads was further investigated using confocal microscopy, to better understand the geometry of the inner and outer phases.

The fluorescent values from effluent collected at regular timepoints, from the petri dishes with fabricated microcapsules stored in DI water, were measured using a plate reader (Biotek; Winooski, VT) and were assessed by using a standard curve created using at 0.5% w/v FITC-dextran 20k Da stock solution.

2.2.6. Material modification and doping in microcapsules

We fabricated alginate-PEGDA microcapsules using a two-chip strategy, with a cleansing stage between the two microfluidic chip phases. The first chip produced crosslinked alginate microcapsules, by initiating a controlled release of Ca^{2+} ions from Ca-EDTA upon exposure to an acidic environment. The microfluidic chip had a flow-focusing junction, followed

by a serpentine pattern area. The microfluidic channels were 500 µm x 250 µm over the serpentine crosslinking channel, with a 100 x 100 µm nozzle of length 1750 µm.

Post-crosslinking, the microcapsules exited the chip while still in an oil suspension and were collected in a 1.5 mL centrifuge tube which was already filled with 1 mL of deionized (DI) water. The tube was centrifuged at 3000 rpm for 60 seconds and then 1 mL of solution was removed and replaced with fresh DI water. After three cycles of centrifuging and replacing the wash liquid, the remaining water was removed and replaced with aqueous PEGDA (of the same composition as used for the dextran-PEGDA microcapsules). We loaded the resulting suspension of alginate microcapsules in a PEGDA prepolymer solution into a 1 mL syringe, to be flowed via syringe pump into the second microfluidic chip. The second chip had 1000 µm-wide channels and a 500 µm-wide nozzle with 500 µm channel height throughout, and had a similar design of a single flow-focusing junction preceding a serpentine pattern area. For this second chip, similar to the dextran-PEGDA case, the UV light source was aligned over the serpentine area for continuous photopolymerization.

2.2.7. Image collection and analysis

A Leica DMI 6000B inverted microscope with 4x and 10x objectives, equipped with a motorized stage (Leica Microsystems, Bannockburn, IL) and Leica DFC9000 GT and DFC7000 T was used to acquire fluorescence and brightfield images. Leica LAS X software was used for

image acquisition. Cropping, color adjustments and contrast enhancements of images as well as Z-stack projections were performed in ImageJ.

2.2.8. Statistical analysis

All statistical testing was performed using Graphpad Prism 9 software (GraphPad, San Diego, CA). Where data was assumed to be normally distributed, values were compared using a one-way ANOVA for single variable with a Sidak post-hoc test applied for multiple comparisons. Where data was assumed to be normally distributed, values were compared using a two-way ANOVA for more than one variable with a Tukey post-hoc test applied for multiple comparisons. Error bars represent standard deviation with n = 3.

2.3 Results

2.3.1. Bulk material analysis

2.3.1.A. Material properties of solutions of interest

Understanding the viscosities of the various solutions considered for on-chip usage is important because viscosity, as a measure of a fluid's internal flow resistance, provides some proxy for capillary number values; due equipment constraints, we were not able to measure interfacial tensions between fluid phases, so as to directly calculate the *Ca*. Rather, we measured the viscosity of fluids of interest, as a proxy for the capillary numbers. Measuring the viscosity of

oil- and aqueous-based fluids demonstrated a wide range of values (**Table 5**), with the viscosity of the aqueous PEGDA and alginate solutions tunable depending on concentration. Dynamic viscosity, μ, is the internal resistance of the fluid to flow and is based on the fluid density, ρ, and kinematic viscosity, ν:

$$\mu = \nu * \rho$$

We chose to limit our testing to non-fluorinated oils. While fluorinated oils are common in droplet microfluidics, particularly when using cells on-chip, we did not pursue these types of oils because of additional challenges with wetting and pretreatment required for using fluorinated oils on PDMS chips.

Fluid	*Density (g/mL)*	*Kinematic Viscosity at room temperature (cSt)*	*Dynamic viscosity (mPa s)*
Mineral oil	0.877		
Light mineral oil	0.840		
Sunflower oil	0.900	61.996	55.796
Mineral oil + 1% Span 80	0.877	168.289	147.590
Mineral oil + 3% Span 80	0.877	170.524	149.549
Light mineral oil + 3% Span 80	0.840	31.459	26.425
Light mineral oil + 1% acetic acid	0.840	27.983	23.506
3% Alginate	1.030	135.093	139.145
Ca-EDTA 1.5% Alginate	1.015	19.7904	20.087
Mineral oil + 1% Acetic acid	0.877	158.891	139.347
Ca-EDTA 3% Alginate	1.030	80.687	83.107
6% Alginate	1.060	1131.391	1199.275
PEGDA400 in 2:3 ratio with PBS	1.050	5.923	6.219

Table 5: Material properties of compositions of interest.

2.3.1.B. PEGDA pore size

While hydrogels are, by definition, able to maintain a three-dimensional polymeric structure even when swollen by water, many past demonstrations of hydrogel-based drug delivery systems have had high background release rates, correlating to the structural mesh size relative to the loaded drug. Therefore, our interest in selecting PEGDA as an outer phase of the

microcapsules was because it is a biocompatible hydrogel which can form structures with very small pore sizes, depending on PEGDA concentration, molecular weight, and photopolymerization process.

We considered the literature values for porosity, which we found to be sufficiently small as to largely contain model drugs with 20k Da molecular weight (**Table 6**). Echogenicity was not significantly different from that of water (1500 m/s), and thus inconclusive as to how visible the microcapsules might be using ultrasound imaging, which will be discussed further in Chapter 3.

Characteristic	**Value from literature**
Shell Polymer	Poly(ethylene glycol) diacrylate 10K, 30% (w/v)
Thickness	1200, 1800, 2400 ± 100 nm
Young's modulus	> 1.8 ± 0.4 MPa
Echogenicity: Speed of sound Characteristic impedance	> 1589 ± 10.42 m/s ([15], measured for lower MW PEGDA) > 1.7 x 10^6 kg/m^2 s ([15], measured for lower MW PEGDA)
Permeability (for composition above): Diffusion Coefficient with respect to 16.7k Da biological molecule	< 5 x10^{-10} cm^2/s [20]
Mesh size	25 ± 3 Å

Table 6: Material properties of PEGDA.

We then conducted swelling and diffusion tests to determine the calculated pore sizes of PEGDA samples at known concentrations and molecular weights (MW). The material properties

of PEGDA vary considerably with concentration and molecular weight, with lower molecular weight PEGDA typically exhibiting greater stiffness and faster photopolymerization, and with higher molecular weights typically correlating to larger mesh sizes and increased swelling rates [82]. From the measured weights during the swelling test, we determined Q_m, the swelling mass ratio:

$$Q_m = [(\text{Wet weight} - \text{Dry weight}) / \text{Dry weight}] \times 100\%$$

When we fabricated a composition of only high molecular weight PEGDA, the samples swelled at a more than 10x rate, even at high concentrations (**Fig. 3a**). When measuring the release of FITC-dextran 20k Da from PEGDA samples, after the FITC-dextran compound had been mixed directly into the PEGDA prepolymer solutions, the lower molecular weight PEGDA had lower release rates than the 10k Da PEGDA (**Fig. 3b**).

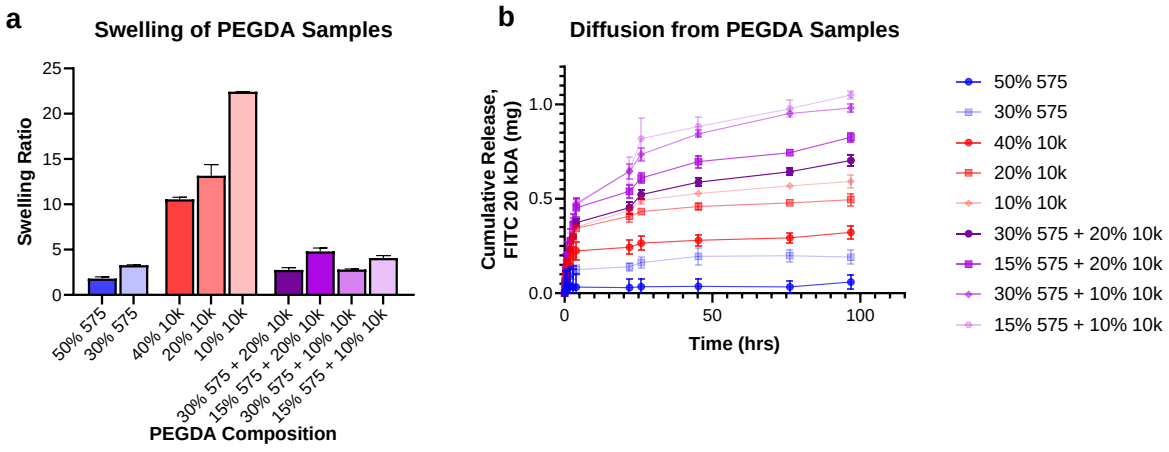

Figure 3: Material testing of varying PEGDA compositions. a) Swelling ratio over time for PEGDA at various concentrations and molecular weights. b) Concentration of diffused fluorescein from PEGDA samples over time.

Variable	Assumed value
Polymer density (ρ_p)	1.12 g/cm^3
Solute density (ρ_s)	1.00 g/cm^3
# of average molecular weight uncrosslinked polymer (M_N)	575 g/mol
Molar volume of solvent (V_1)	18 cm^3/mol
Polymer solvent interaction ratio (χ_1)	0.426
Length of carbon-carbon bond (l)	0.146 nm
Flory characteristic ratio (C_n) for PEG	4.0
Polymer repeat unit (M_R)	44 g/mol

Table 7: Known values for PEGDA prepolymer.

Based on known values from literature (**Table 7**) and the measured values of swelling mass ratio, Q_m, we calculated pore sizes for polymerized PEGDA at both 10k and 575 MW. Firstly, the swelling mass ratio, Q_m, converts to a volume swelling ratio, Q_v:

$$Q_v = 1 + \frac{\rho_p}{\rho_s}(Q_m - 1)$$

Furthermore, the specific volume of PEGDA in amorphous state, v_2 is calculated as:

$$v_2 = 1/Q_V$$

We then calculated the molecular weight between crosslinks, M_C as:

$$\frac{1}{M_C} = \frac{2}{M_N} - \frac{\frac{\rho_s/\rho_P}{V_1}(\ln(1 - v_2) + v_2 + \chi_1 v_2^2)}{v_2^{1/3} - \frac{v_2}{2}}$$

where M_N is the average molecular weight of the uncrosslinked polymer, V_1 is the molar volume of the solvent, v_2 is the polymer volume fraction as calculated as the inverse of the volume swelling ratio, and χ_1 is the polymer-solvent interaction parameter [83-85]. The pore size ξ was then estimated as:

$$\xi = Q_v^{1/3} l (C_n N_b)^{1/2}$$

where Q_v is the volume swelling ratio, l is the length of carbon-carbon bond, C_n is the Flory characteristic ratio, and N_b is the number of carbon-carbon bonds between closest crosslinking points. The resulting values are in the 0.48-0.96 nm range for PEGDA Mn 575 and 5.82-8.65 nm for PEGDA Mn 10k (**Table 8**). Although this calculation method is not applicable for PEGDA compositions of mixed molecular weights, we observed swelling trends of the mixed molecular weight polymers to closely resemble that of the PEGDA Mn 575 solutions.

Composition	***Mc, Molecular weight between crosslinks***	***Pore size (nm)***
50% PEGDA 575 MW	78.64 ± 20.19	0.48 ± 0.08
30% PEGDA 575 MW	202.23 ± 1.38	0.96 ± 0.006
40% PEGDA 10k MW	3389.13 ± 45.64	5.82 ± 0.08
20% PEGDA 10k MW	3823.67 ± 159.38	6.66 ± 0.35
10% PEGDA 10k MW	4511.94 ± 0.45	8.65 ± 0.002

Table 8: Calculated molecular weight between crosslinks and pore sizes.

2.3.1.C. Aqueous phase separation

Fabricating a biocompatible microcapsule with multiple aqueous-based layers is traditionally challenging because of the low interfacial tension between aqueous phases [78]. To overcome this challenge, one strategy that we pursued was to incorporate aqueous two-phase solutions (ATPS), a liquid-liquid fractionation method that relies on the incompatibility of two aqueous solutions, typically polymer-polymer or polymer-salt solutions. In ATPS, phase separation occurs because of incompatibility between the polymer pairs, due to noncovalent interactions between water and the polymers and between parts of the polymers; temperature, pH, and concentration can also impact whether phase separation occurs [86]. In particular, we tested dextran-PEGDA and dextran-Poly(vinyl alcohol) (PVA); we tested a range of molecular weights for the PEGDA and PVA polymers. Due to the freeze-thaw technique [87] required for dextran-PVA microcapsules, our results were far less consistent than with dextran-PEGDA microcapsules, and thus we have focused our development efforts on the microcapsules with the dextran-PEGDA composition.

The spontaneous separation of two polymers above minimum polymer concentrations occurs when the enthalpy of demixing is greater than the gain in entropy of mixing, and is dependent on factors such as interfacial tension; solution temperature and pH; the presence of salts; and polymer molecular weight [88, 89]. PEGDA and dextran molecules impact the water molecules surrounding each molecule through hydrophobic and hydrophilic bonding. It has been shown that poly(ethylene glycol) (PEG) and dextran molecules have a significant impact on the

structure of surrounding water; for example, one monomer unit of PEG affects up to 16 nearby water molecules [88]. The water structures surrounding PEG and dextran molecules are incompatible; as such, above minimum concentrations of both polymers, demixing occurs. Information about the compositions and relative volumes of the two phases can be plotted on a binodal phase curve [88-90]. In comparing the necessary concentration levels needed for phase separation to occur when using PEGDA 575 Da compared to PEGDA 10k Da, we observed that phase separation occurred at lower PEGDA concentrations when using higher molecular weight PEGDA (**Fig. 4**). We observed a similar effect for high MW dextran compared to low MW dextran (data not shown). Furthermore, phases with the highest MWs and highest concentrations resulted in effective phase separation as shown by the phase diagram, and also separated quickly to enable phase separation prior to the photopolymerization region.

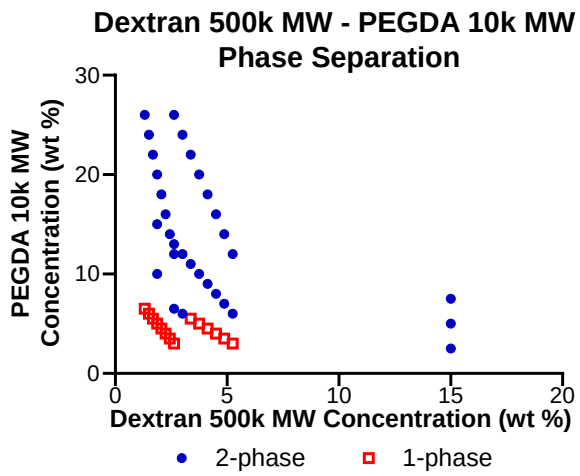

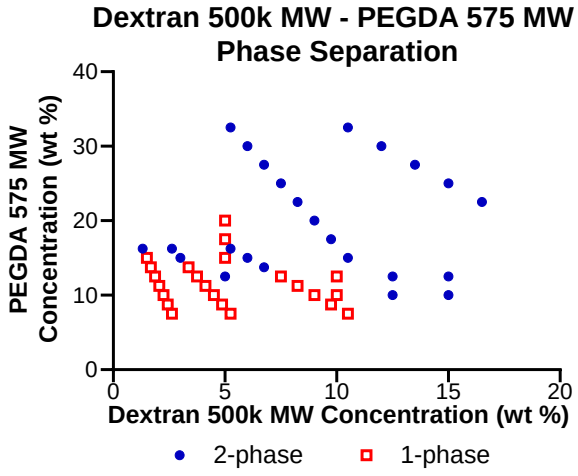

Figure 4: Single and two-phase dextran-PEGDA compositions. Single phase (not phase separated) compositions are shown demarcated as open red circles and occur at lower concentration values, while two-phase (phase separated) solutions are demarcated as closed blue circles and occur at higher concentration values. Furthermore, using a higher MW PEGDA (left) results in two phases solutions at relatively lower concentrations, compared to the same concentration values with relatively lower MW PEGDA (right).

2.3.2. Microfluidic droplet formation

2.3.2.A. Microfluidic chip design and fabrications

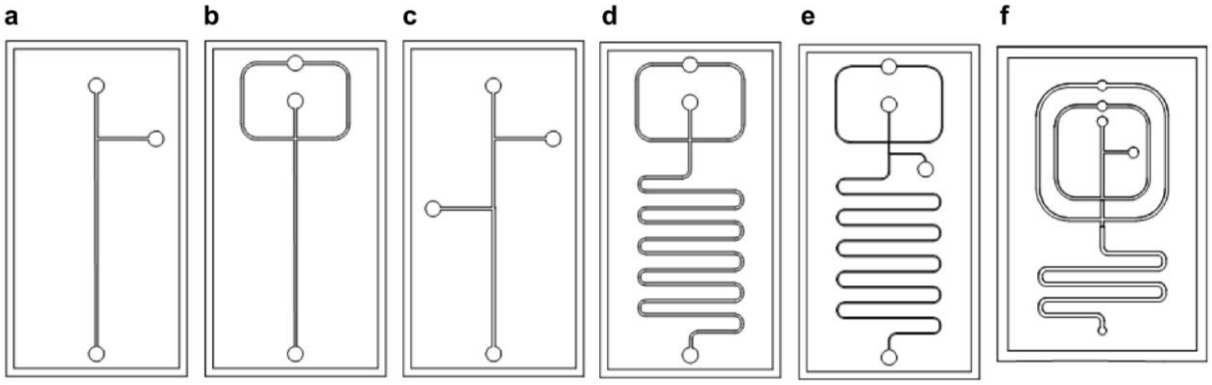

Figure 5: Assortment of initial microfluidic chip designs, with varied junction designs, including (a) chip with single T-junction, (b) single flow-focusing junction, (c) two T-junctions in series, (d) a single flow-focusing junction, followed by a serpentine area, (e) a flow-focusing junction and T-junction in series, followed by a serpentine area, and (f) a T-junction followed by two flow-focusing junctions and a serpentine area.

We fabricated a range of microfluidic chip designs with channel dimensions in the range of 200-500 µm, to determine the corresponding flow regimes for chip design at various flow rates. The two most common junction geometries for microfluidic droplet formation, when using planar chips fabricated in PDMS, are T-junction and flow-focusing junctions. In a T-junction, as

shown in **Fig. 5a** and **5c**, the inlet channel of dispersed phase intersects the main channel at an angle, typically perpendicularly, and the two phases form an interface at the junction. As fluid flow continues, the tip of the dispersed phase enters the main channel; shear forces generated by the continuous phase, and the corresponding pressure gradient, cause the tip of the dispersed phase to elongate further into the main channel. Eventually, the neck of the dispersed phase thins and breaks the dispersed phase stream into a droplet. In contrast, in a flow-focusing junction (**Fig. 5b, d**), the dispersed and continuous phases are forced to momentarily coflow through a narrow channel on the microfluidic device, during which the continuous phase exerts symmetric shearing on the dispersed phase to generate droplets composed of the dispersed phases. During initial experimentation, we achieved droplets with more consistent diameters using a flow-focusing junction as compared to a T-junction, particularly a for sub-200 μm droplets [91, 92].

Furthermore, we determined that integrating a nozzle into the design of a flow-focusing microfluidic chip allows for further control over droplet size and dispersity, as shown in **Fig. 5e** and in the third junction of **Fig. 5f**.

2.3.2.B. Droplet fabrication

While maintaining consistent geometry, we tested the varying microfluidic chip conditions, specifically viscosity and flow rates (**Fig. 6**). When in the dripping regime, the interfacial force is dominant and the inertial force is negligible. Specifically, dripping occurs when the viscous forces at the liquid interface overcome the interfacial forces, which are tending

to pull the forming droplet back towards the injection nozzle, to facilitate the formation of a droplet near the tip of the nozzle orifice. We determined that the dripping regime most commonly occurs typically at a flow rate ratio of 1:10-15 for dispersed:continuous phase, with the continuous phase occurring in the 10-16 µL/min.

Furthermore, viscosity of considered dispersed and continuous phases provided a guiding viscosity ratio, which aided in determining appropriate material characteristics to optimize for the dripping regime. Initial chip designs provided proof-of-concept demonstrations of a single dispersed phase into a continuous phase in the dripping regime. Based on runs of this initial microfluidic system, with a dispersed phase of 3% w/v alginate and a continuous phase of light mineral oil with 3% v/v Span 80, we determined that the dripping regime tends to occur with low flow rates in both regimes, particularly in the dispersed regime; these findings are confirmed by guidance from literature [80]. Furthermore, we determined that dripping most commonly occurred when the ratio of $1 < (\mu_{dispersed} : \mu_{continuous}) < 4$.

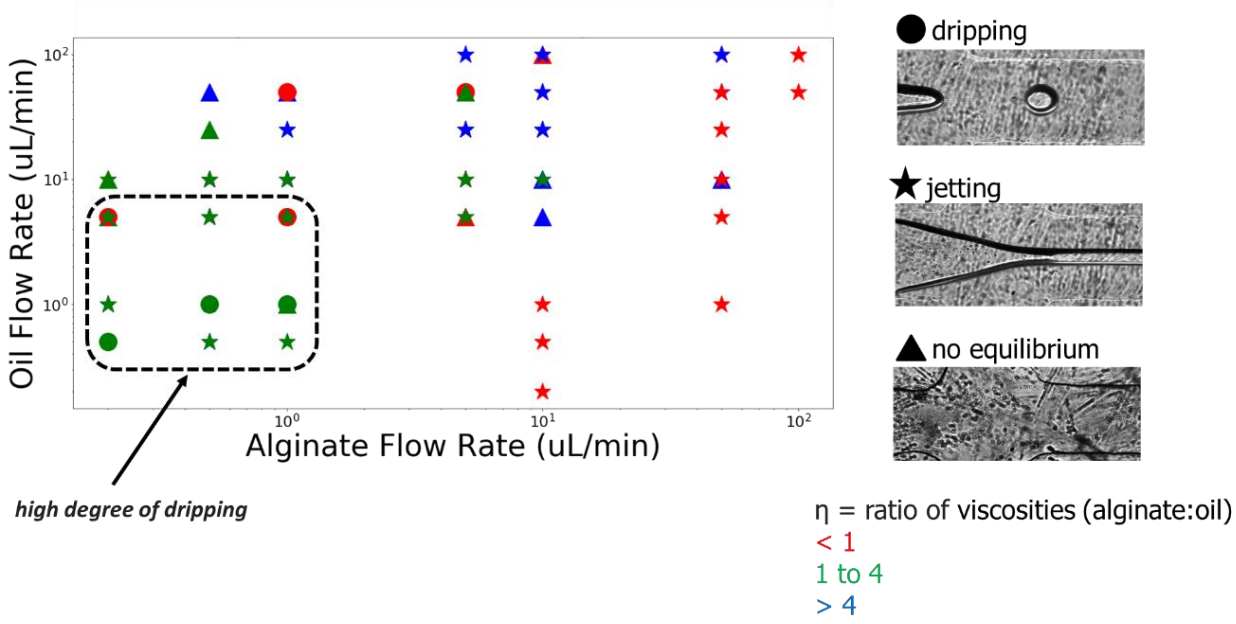

Figure 6: Dripping regimes for a microfluidic system with a single flow-focusing junction. The plot of relative flow rates demonstrates the correlation between relative flow rate, viscosity and droplet-formation regime. The brightfield microscope images on the right provide visual examples of the various regimes.

2.3.3. Biphasic droplet fabrication

To fabricate biphasic microcapsules with dextran 500k Da as the inner phase and PEGDA as the outer phase, we began by testing on a microfluidic chip with two flow-focusing junctions in series (**Fig. 7a**), using the same microfluidic chip fabrication method as previously described. The final microfluidic chip featured the two flow-focusing junctions in series followed by a serpentine region for photopolymerization (**Fig. 7b**), to produce polymerized double-emulsion microcapsules. Co-flowing occurred at the first junction (**Fig. 7c**), as we selected flow rates that resulted in the dispersed dextran solution jetting in the continuous

PEGDA phase; dripping occurred at the second junction (**Fig. 7d**). It is relevant to not that immediately after a first junction, a small amount of mixing took place between the dextran and PEGDA phases, as shown in fluorescence imaging by a slightly diffuse phase boundary, with the fluorescent compound being Fluorescein isothiocyanate–dextran (FITC-dextran), the model drug, which largely remains in the dextran-rich phase. This small amount of mixing accounts for the low amounts of fluorescent drug detected on the microcapsule surface post-fabrication and washing. The regime at each junction was based on the capillary number of the two flows, which can be manipulated by changing the viscosities of the two phases; to ensure the desired regimes, we tuned the flow rate of each phase while keeping concentrations consistent, resulting in the final flow rates and compositions listed in **Table 9.** We found the chip to consistently run continuously for up to 4 hours; after that time, the chip tended to clog, likely due to swelling of the PDMS. The overall droplet dimensions were controlled by the channel dimensions of the chip, particularly at the nozzle of the chip.

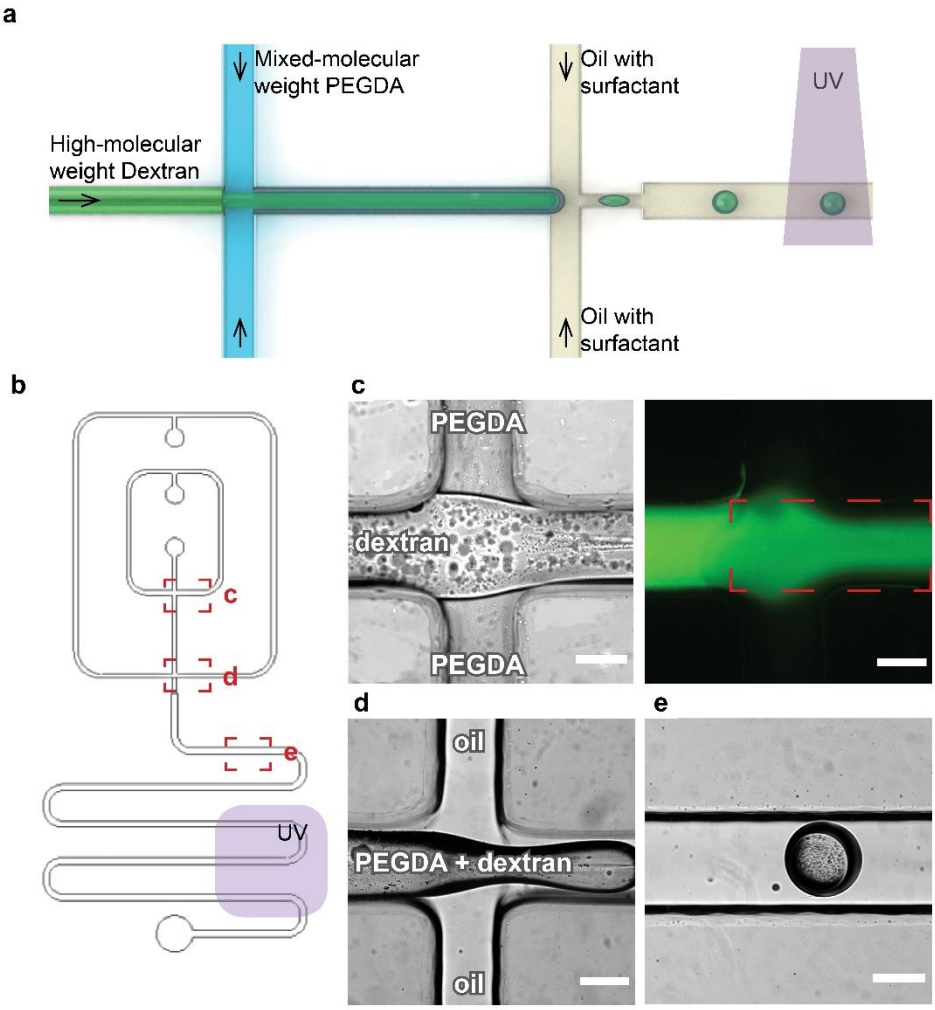

Figure 7: Microfluidic fabrication of dextran-PEGDA droplets. a) Schematic diagram of the fabrication and UV polymerization of biphasic microcapsules in a microfluidic device. Compared to other aqueous two-phase systems, a mixed high and low MW PEGDA and a high MW dextran are used as the two phases. b) Design of microfluidic chip, featuring a series of two flow-focusing junctions followed by a serpentine area that allows for sufficient time to complete phase separation and for ultraviolet exposure (shown in purple) to photopolymerize the PEGDA phase. c) Brightfield (left) and fluorescent (right) images of the first junction, where the dextran phase loaded with model drug co-flows within the outer PEGDA phase. The dotted red box in the fluorescent image indicates where mixing occurs along the boundary between the dextran and PEGDA. d) Brightfield image of the second junction, demonstrating dripping of the dextran and PEGDA phases into the continuous outer oil phase to form discrete aqueous droplets. e) Brightfield image of the dextran-PEGDA aqueous droplet, undergoing internal phase separation, in the oil phase. Scale bars are 400 µm.

Inlet port	*Composition*	*Flow rate (µL/min)*
Inner dispersed phase	3.75% dextran 450-650k Da + 2% dextran-FITC 20k Da	(0.9 µL/min)
Outer dispersed phase	PEGDA 10k Da (20% w/v) + PEGDA 575 Da (30% v/v) + 2.5% Darocure 2959 (w/v)	(0.5 µL/min)
Continuous phase	Light mineral oil + 3% Span 80 (v/v)	(12 µL/min)

Table 9: Microfluidic conditions required for the fabrication of dextran-PEGDA biphasic microcapsules.

The phase separation properties of ATPS were particularly useful for microfluidic fabrication, enabling the formation of water/water/oil (W/W/O) triple emulsions despite the low interfacial tension between the two aqueous phases [77]. The PEGDA composition was chosen because using entirely low-molecular weight PEGDA did not facilitate real-time phase separation during the microfluidic fabrication process, while the high-molecular weight PEGDA resulted in a larger pore size which would correspond to higher diffusion rates. Thus, to minimize diffusion rates while facilitating phase separation within less than a minute while on the microfluidic chip, we used of a mixture of molecular weights; this mixed-molecular weight PEGDA prepolymer resulted in minimal swelling due to the small pore size, and phase separated quickly.

The microfluidic chip with two flow-focusing junctions in series reliably produced dextran-PEGDA droplets with an asymmetrical geometry (**Fig. 7e**). When observing the droplets during the first <10 seconds post-junction, there was a visible amount of adjustment of the relative volumes between the dextran and PEGDA phases, but the droplets stabilized by the second turn of the serpentine portion of the chip. Furthermore, while the overall structure of the droplet is spherical, the dextran inner phase tends to fall to the rear of the overall aqueous droplet as the droplet progresses through the microfluidic chip, resulting in an asymmetry to the droplet; we believe that this is caused by a combination of the molecular weight mismatch between the dextran and PEGDA phases and by a difference in wetting properties between the two phases. This occurred regardless of the inclusion of a serpentine pattern of the chip.

2.3.4. Polymerization of droplets into microcapsules

The PEGDA phase of the dextran-PEGDA was successfully photopolymerized as the droplets passed through the serpentine area of the microfluidic channel. The amount of photoinitiator in the PEGDA phase was sufficient to allow for the microcapsules to photopolymerize at the flow rates needed to maintain the dripping regime and to maintain consistent spacing between droplets. While we initially tested more traditional ultraviolet LEDs, we determined that the 12 mm^2 UV LED array was necessary to supply sufficient UV intensity. This array required integration with a heat sink and a thermal sensor to monitor temperature, along with a voltage regulating circuit (**Fig. 8**). It had the distinct advantage over using a larger LED bulb of fitting into housing to ensure consistent alignment over the desired area of

exposure, and to minimize incidental UV exposure on other areas of the chip that could result in clogging.

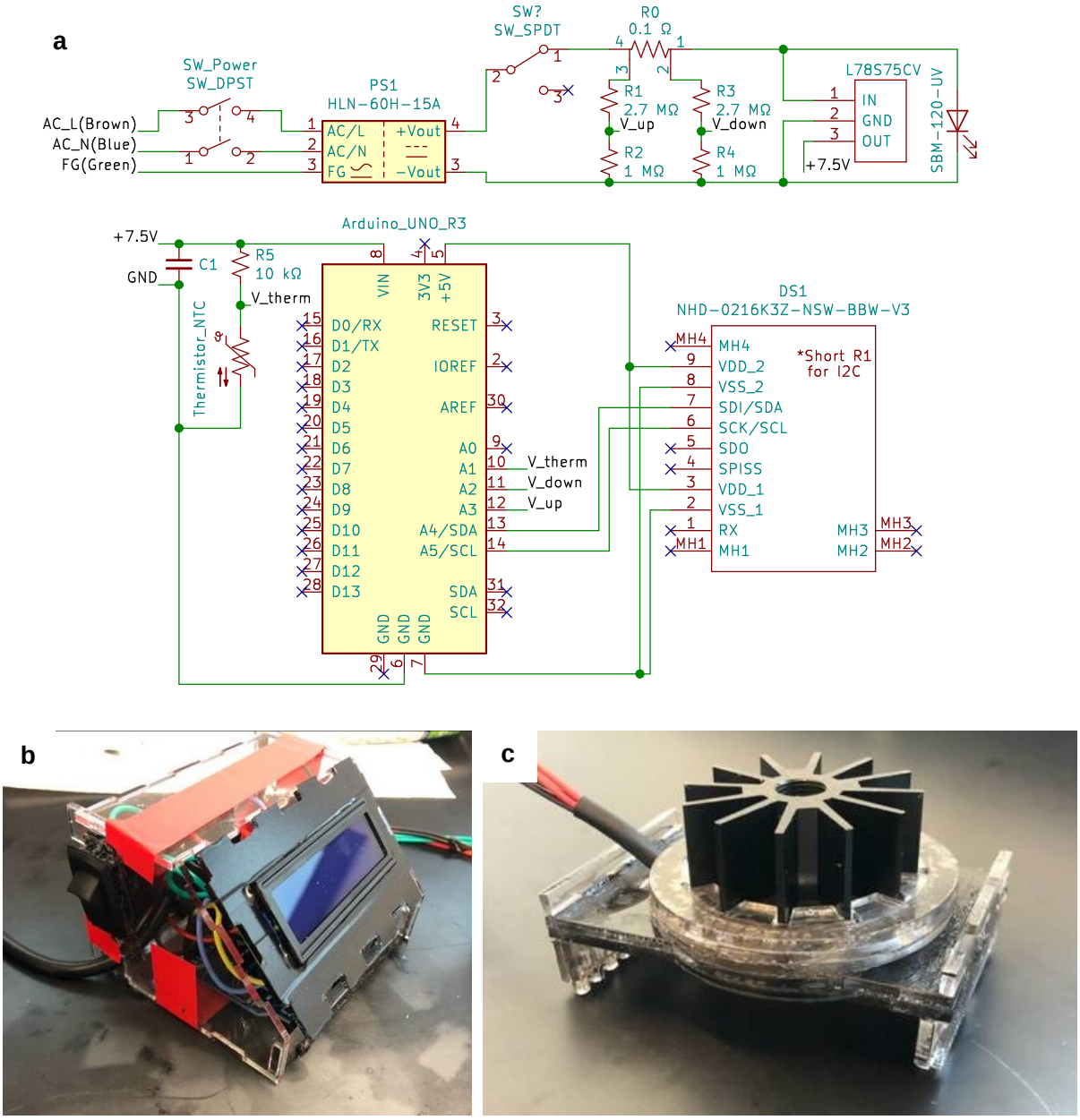

Figure 8: Custom ultraviolet-emitting system for on-chip photopolymerization process. a) Electronic circuit design. b) Monitoring and control system, which provides readout of current temperature of device, as well as current UV intensity level. c) UV emitting component, with custom-cut acrylic housing to fit over microfluidic chip with UV light source aligned over the serpentine area of our chip, and integrated heat sink to reduce risk of overheating.

2.3.5. Microcapsule characterization and tuning

We found that the resulting microcapsules were 548.7 ± 37.8 µm in diameter (**Fig. 9**), which could be tuned by adjusting flow rates or the channel dimensions of chip, particularly at the nozzle of the chip. The microcapsules maintained the asymmetric socket-based structure that has been previously discussed, as seen in **Figure 9a**, in which the inner dextran phase appears much darker than the surrounding PEGDA phase.

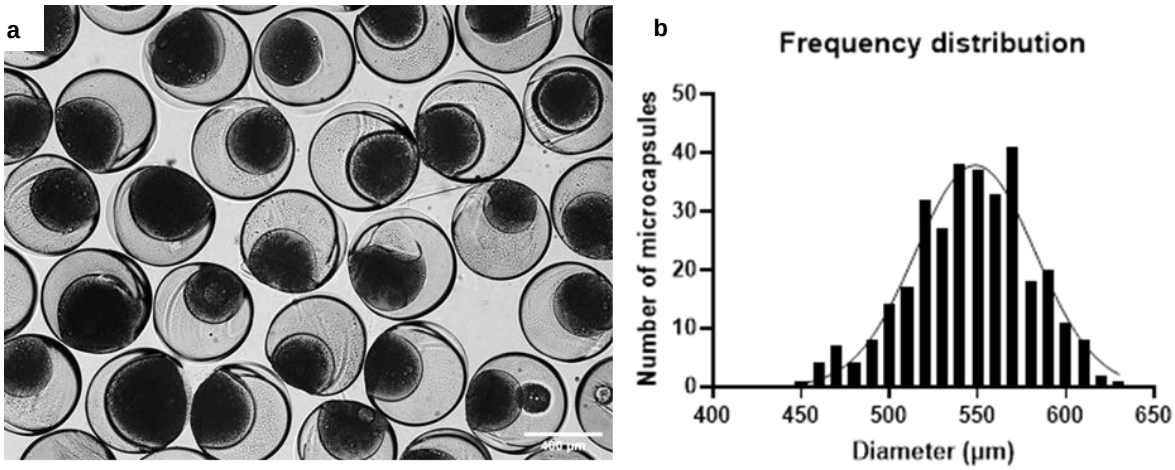

Figure 9: Characterization of polymerized and washed microcapsules. a) A monolayer of microcapsules in DI water, with portion of the inner dextran phase exposed on the surface of the microcapsules, appearing as the dark area Scale bar is 400 µm. b) The plotted dispersity of microcapsule diameter.

Fluorescent imaging of the microcapsules indicates that the FITC-dextran remains largely concentrated in the dextran region, with a minimal amount of FITC-dextran in the PEGDA phase that appears consistent with the slight migration of FITC-dextran during the first co-flowing junction on-chip (**Fig. 7d**). As the microcapsules were formed by applying the ATPS technique, the inner and outer phases of the microcapsules are dextran-rich and PEGDA-rich, respectively,

but are not exclusively each material. Thus, the dextran-rich phase has structure due to the low concentrations of PEGDA within the phase, but prior research into the correlation between PEGDA concentration and mesh size [93] indicates that the dextran-rich region has a much looser mesh than the PEGDA-rich phase; given that a portion of the dextran-rich phase is partially exposed, without a covering of the PEGDA-rich phase, due to the asymmetry of the microcapsules discussed above, we expect some background leakage. Fluorescent images after 10 days in solution indicate that there has been some reduction of FITC-dextran, particularly in the dextran phase (**Figure 10**).

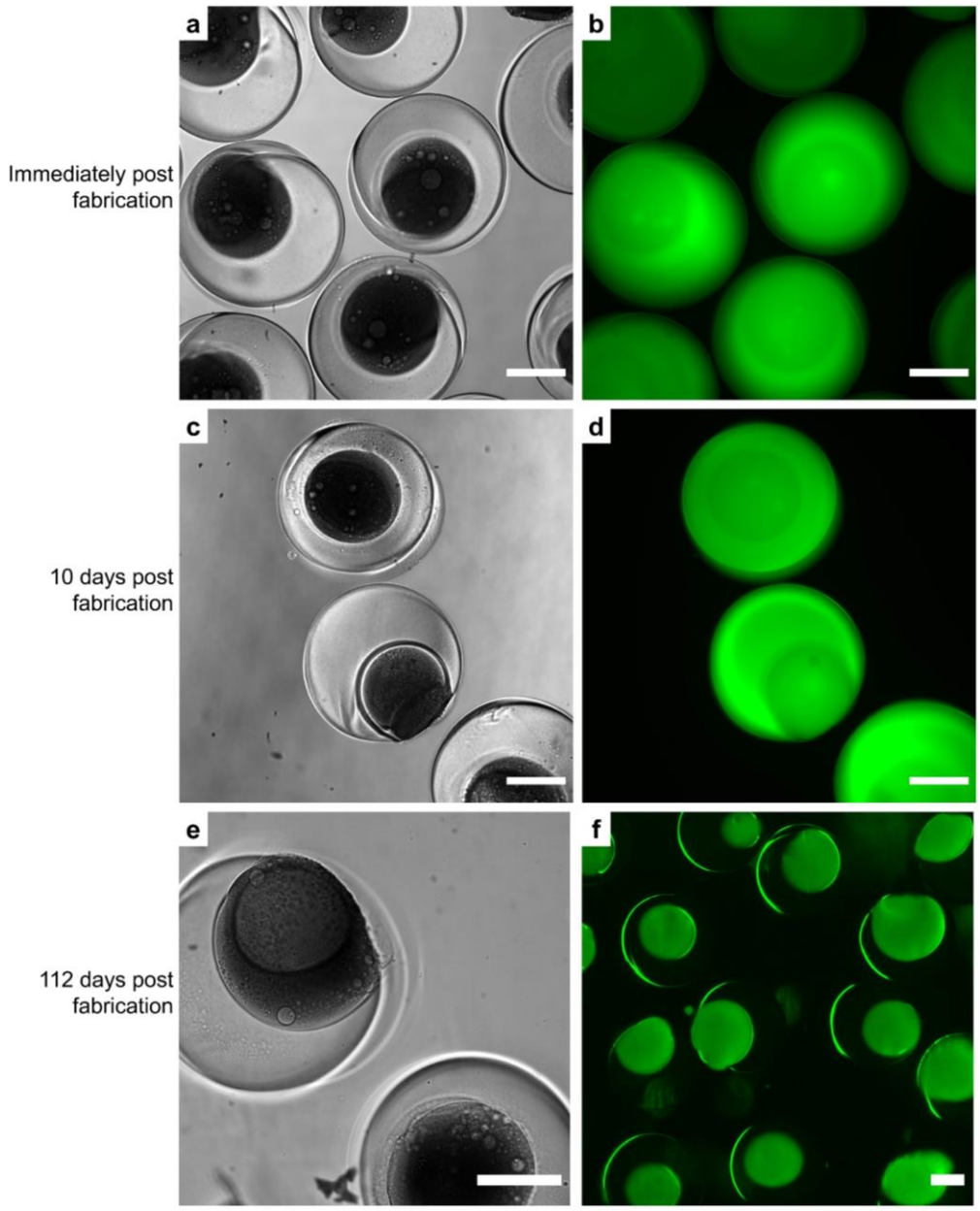

Figure 10: Assessment of loading stability of microcapsules, as imaged immediately after fabrication in brightfield (a) and fluorescence (b), after 10 days in DI water in brightfield (c) and fluorescence (d), and after 112 days in DI water in brightfield (e) and fluorescence (f). Images were taken at the same exposure settings on all days Scale bars are 200 µm.

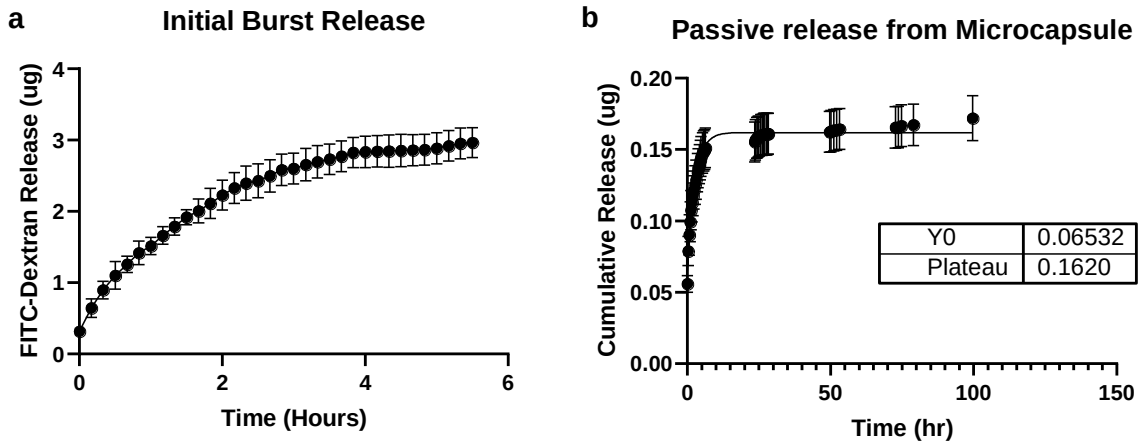

Figure 11: Passive release from microcapsules. Full release (a) and release profiles for initial 6 hrs. b) of a microcapsule when not exposed to FUS at any point.

Moreover, measuring the release profile of the microcapsules over several days showed a burst release of 0.1531 ± 0.0097 µg within the first 6 hours, with the total passive release plateauing at 0.1620 ± 0.030 µg when measured over several days (**Fig. 11**).

Varying the material compositions correspondingly changes the phase separation points. Given the asymmetry of our microcapsules, we tested different surfactant concentrations to observe the corresponding effect on microcapsule structure. Increasing the surfactant concentration should decrease interfacial tension between aqueous and oil phases, particularly in the dextran/oil interface; it adjusts contact angles and has experimentally resulted in increasing the exposed dextran surface. Complete engulfing should occur when

$$\gamma(\text{oil-dextran}) > \gamma(\text{dextran-PEG}) + \gamma(\text{oil-PEG})$$

but these conditions proved challenging to consistently achieve within the microfluidic environment [94]. Testing this on-chip, decreasing the surfactant concentration decreases interfacial tension between aqueous and oil phase, particularly dextran/oil interface; it adjusts contact angles and has experimentally resulted in decreasing the exposed alginate-dextran surface (**Fig. 12**).

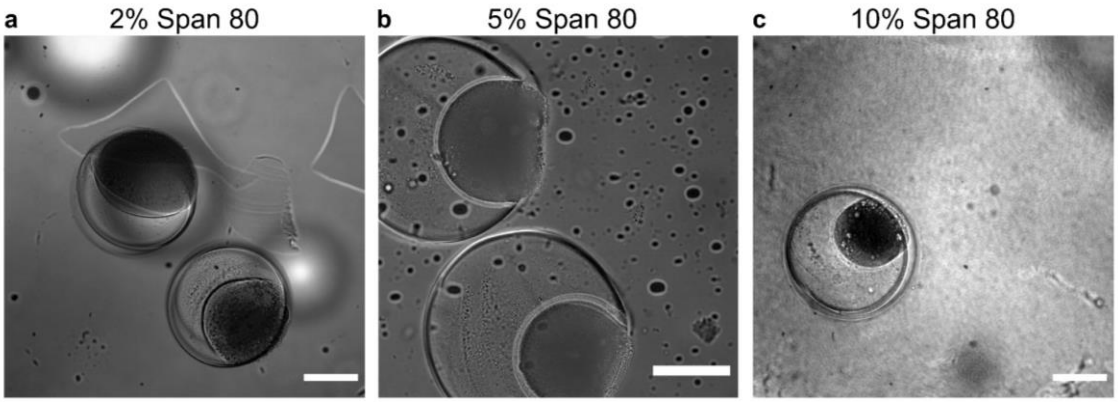

Figure 12: Brightfield images of the structure of dextran-PEGDA droplets when flow rates were kept constant but the surfactant concentration was adjusted. The dextran portion is outlined in light green and the PEGDA component is outlined in light blue. Surfactant concentrations increased from left to right, from 2% - 10%. Scale bars are 400 µm.

2.3.6. Material modification and doping in microcapsules

Due to the flow rates of the microfluidic chip, the phase separations ratios of the dextran and PEGDA phases did not directly follow the phase separation trends shown during experimentation with bulk material volumes. To further investigate the impact that the initial dextran and PEGDA compositions and concentrations have on phase separation within the microcapsule, we ran the microfluidic chip at consistent flow rates with a range of dextran and PEGDA compositions (**Table 10)**. Low concentrations of both PEGDA 575 MW and PEGDA

10k MW resulted in microcapsules where the dextran-rich phase did not have enough structure to retain the dextran, resulting in a hollow, bucket-like shape (**Fig 13b**). Reducing only the PEGDA 10k MW concentration resulted in a notable shift in the phase separation so that the dextran phase was much larger; by maintaining the 30% concentration of PEGDA 575 MW, the microcapsules still polymerized (**Fig. 13c**). Premixing the dextran and PEGDA solutions 24 hours prior to on-chip fabrication, and then loading syringes with the dextran-rich and PEGDA-rich phases, respectively, resulted in a slight shift of phase separation behavior, such that the dextran phase became larger relative to the PEGDA phase (**Fig. 13d**).

Additionally, we fabricated microcapsules with a PVA-PEGDA solution pumped into the outer aqueous phase. This was of interest because PVA, similar to PEGDA, phase separates with dextran at sufficiently high concentrations. Adding polyvinyl alcohol (PVA) to the PEGDA phase resulted in a microcapsule which appeared to have an additional inner phase (data not shown). However, undergoing five freeze-thaw cycles to polymerize the PVA phase resulted in inconsistent microcapsules, which had cracking and did not retain the FITC-dextran model drug (data not shown).

Figure	*Inner Phase*	*Outer Phase*	*Photoinitiator*	*Location where phase separation occurs*
13a	3.75% dextran 450-650k Da + 2% dextran-FITC 20k Da	20% (w/v) PEGDA 10k MW + 30% (v/v) PEGDA 575 MW	0.3% LAP (w/v)	On-chip
13b	3.75% dextran 450-650k Da + 0.6% dextran-FITC 150k Da	14% (w/v) PEGDA 10k MW + 5% (v/v) PEGDA 400 MW	2.5% (w/v) Darocure 2959	On-chip
13c	7.5% dextran + 2% FITC-dextran 20k Da	10% (w/v) PEGDA 10k MW + 30% (v/v) PEGDA 575 MW	2.5% (w/v) Darocure 2959	On-chip
13d	3.75% dextran 500k Da + 2% FITC-dextran 20k Da	20% (w/v) PEGDA 10k MW + 30% (v/v) PEGDA 575 MW	2.5% (w/v) Darocure 2959	Prior to injection into chip

Table 10: Example phase compositions tested for aqueous multilayered microcapsules.

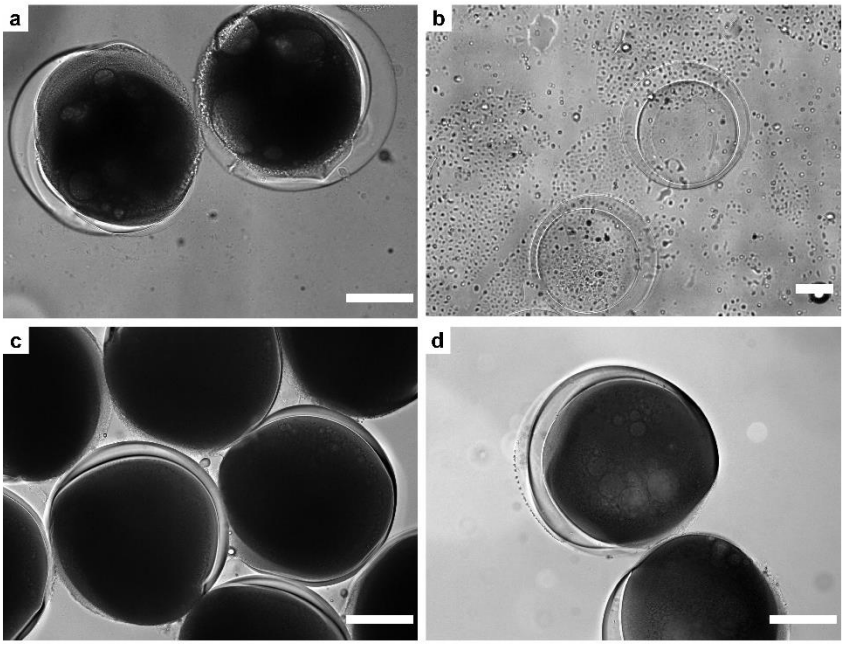

Figure 13: Variations in microcapsule composition. a) Microcapsules formed using 0.3% LAP as the photoinitiator. b) Microcapsules loaded with FITC-dextran 150k Da as model drug, as well as lowered concentrations of PEGDA in the outer phase. In the resulting microcapsules, the inner phase migrates out of the PEGDA structure. c) Higher concentration of dextran and lower concentration of PEGDA 10k MW, altering the final volumes of PEGDA-rich and dextran-rich phases. d) Microcapsules formed using dextran and PEGDA which has been premixed and allowed to phase separate prior to being pumped onto the microfluidic chip, rather than in real-time while on-chip. Scale bars are 200 µm.

The alternative microcapsule strategy of an alginate inner phase and PEGDA outer phase necessitated a fabrication strategy of two microfluidic chips in series (**Table 11**, **Fig. 14**), because the interfacial tension between the alginate and PEGDA phases was so low. Rather than introduce the alginate and PEGDA phases sequentially on a single chip, in the manner employed for the dextran-PEGDA microcapsule fabrication, we crosslinked the alginate droplets on one chip, washed the resulting alginate beads, then suspended those beads in the PEGDA prepolymer, which we flowed onto a second chip to form droplets and to photopolymerize the

PEGDA phase. This strategy ensured that the two phases stayed distinct and allowed for a biphasic aqueous-based microcapsule where the inner phase was not asymmetrically placed. However, the alginate beads did not flow in the PEGDA phase at a consistent pacing, making the resulting microcapsules inconsistent; many microcapsules consisted only of the PEGDA phase. While this method requires additional refinement, this strategy is included as a direction for future work because it does not rely on ATPS and thus does not involve an inherent molecular weight mismatch between aqueous phases and may result in fully symmetric core-shell microcapsules structures, which may have additional or alternative applications compared to the aforementioned dextran-PEGDA structures. As notable in **Fig. 14b**, though, one current limitation of this method is that the microcapsules can be challenging to completely wash free of residual oil droplets, appearing as smaller circles dispersed throughout the image

	Inlet port	*Composition*	*Flow rate (µL/min)*
Chip 1	1 (Dispersed phase)	1.5% (w/v) Medium Viscosity G (MVG) Alginate	0.55
	2 (Co-flow phase)	900 mM Ca-EDTA	0.85
	3 (Continuous phase)	Light mineral oil + 1.5% (v/v) Span 80	9
	4 (Continuous phase)	Light mineral oil + 3% (v/v) Acetic Acid + 1.5% (v/v) Span 80	9
	5 (Continuous phase)	3% (v/v) Aqueous Acetic acid	40
Chip 2	6 (Dispersed phase)	PEGDA 10k Da (20% w/v) + PEGDA 575 Da (30% v/v) + 2.5% Darocure 2959 (w/v) + Alginate microcapsules	6
	7 (Continuous phase)	Light mineral oil + 6% Span 80 (v/v)	100

Table 11: Phase compositions for first and second chips in the sequential formation of Alginate-PEGDA microcapsules.

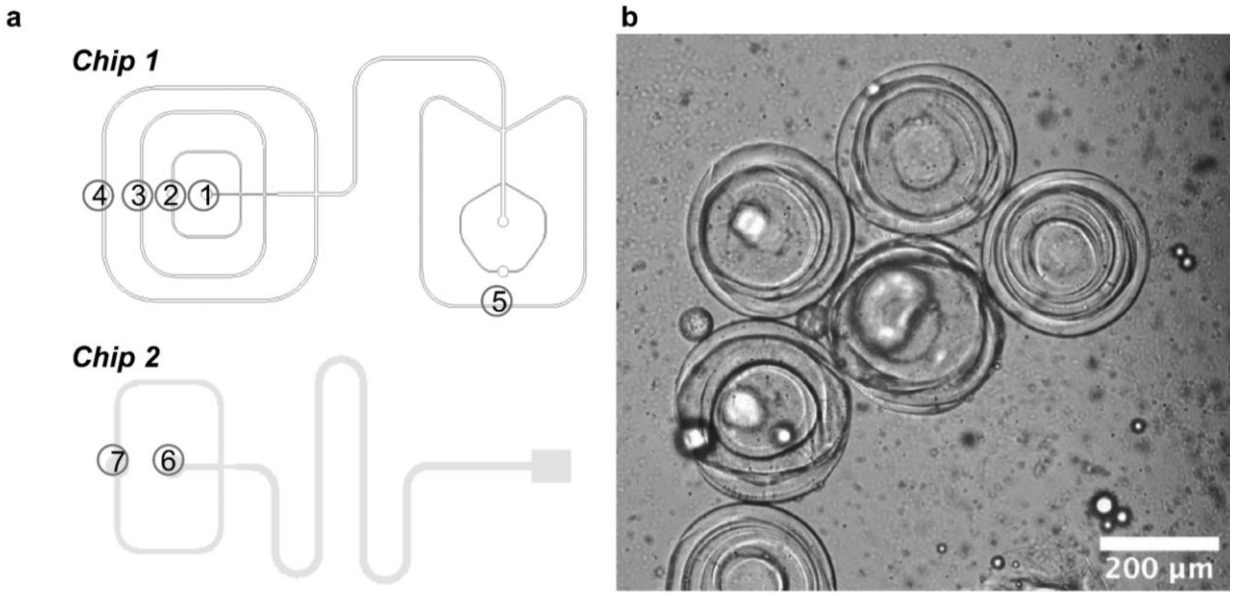

Figure 14: Alginate-PEGDA microcapsules. a) The microparticles a fabricated on two chips, with the respect inlet compositions listed in Table 11. Alginate particles crosslink on chip 1, and then a PEGDA shell forms around the alginate particles on chip 2, with photopolymerization of the PEGDA phase occurring on-chip during the serpentine region. b) The resulting two-phase aqueous microcapsules have a symmetric biphasic structure.

2.4 Discussion

We have demonstrated fabrication of microcapsules of consistent dimensions and geometry with multiple aqueous-based phases without intermediate oil phases. The fabrication technique is relatively novel in that it is among the few examples of water-in-water microcapsule fabrication which is entirely passive and thus is relatively low-cost and requires minimal equipment [79, 95]. These microcapsules were loaded were a large payload of model drug relative to overall volume, which could be passively released over the course of more than a week. Another

element of novelty is the ability to photopolymerize in real-time on a PDMS chip, with minimal refraction complications, as well as the dual-polymerization required for the alginate-PEGDA microcapsules [96].

While the dextran-PEGDA MPs have been tuned for use with ultrasound (for discussion in Chapter 3) and are included in a manuscript that has been submitted for peer review, the alginate-PEGDA capsules continue to be developed further. In addition, we intend to continue to explore methods for doping the microcapsule phases, such as with prefabricated gas vesicles or magnetic nanoparticles, as well as for implementing surface modifications, such as by adding biotin binding points to the outer PEGDA surface. We envision that such directions could add additional functionality to the microcapsules, ranging from potential propulsion to localized sensing applications.

Chapter 3: Focused ultrasound-based stimulation of hydrogel devices for extracorporeal control

3.1 Background

Localized drug delivery systems can be controlled in a variety of manners, namely through extracorporeal manual control, extracorporeal closed-loop control, and intrinsic closed-loop control systems. The most flexible strategy, generally, is to rely on extracorporeal controllers, which have less power and space constraints than the embedded alternative. Such external controller modalities may be operated manually or rely on machine-learning algorithms for closed-loop operation.

Common methods for such extracorporeal control modalities include magnetic, ultrasound, near-infrared mechanisms, as compared in **Table 12**Table 12: Feedback and control modalities. Comparison of key characteristics for the most common control modalities and mechanisms for localized delivery systems, with check marks indicating that the respective modality performs relatively well with respect to the considered characteristic [13]. We have pursued the use of ultrasound as our mechanism for actuating control release because, comparatively, ultrasound can non-invasively penetrate deep into tissue without the need to incorporate magnetic or metallic materials, which may allow for fewer issues of biocompatibility or likelihood of needing to retrieve a device post-application [58, 97]. Furthermore, ultrasound can induce two types of response modalities in materials: heating and cavitation.

	Modality		
Characteristic	***Magnetic***	***Ultrasound***	***Near-infrared (via photothermal effect)***
Depth of penetration	✓	✓	
Resolution		✓	
Equipment requirements		✓	✓

Table 12: Feedback and control modalities. Comparison of key characteristics for the most common control modalities and mechanisms for localized delivery systems, with check marks indicating that the respective modality performs relatively well with respect to the considered characteristic [13].

Ultrasonic-triggered actuation relies on ultrasound waves, which are mechanical longitudinal waves transmitted at frequencies above 20 kHz, the limit of human hearing [67]. Ultrasound has been used for diagnostics, imaging, and, more recently, for surgery and therapeutic applications including drug delivery, gene transfection, and tumor ablation [25, 29, 58, 98]. In traditional brightness-mode (B-mode) ultrasound, low acoustic pressure produced by an ultrasound transducer passes through a region of interest. A portion of the ultrasound wave reflects back to the transducer if the acoustic impedance of the medium changes – such as when the wave encounters a bone, tumor, or air – and the magnitude of difference in acoustic impedances at these interfaces of change determines the magnitude of the reflection, and thus the brightness, of the resulting image [67].

In contrast, many therapeutic applications of ultrasound incorporate forms of focused ultrasound (FUS), which can induce the aforementioned heating and cavitation responses. In

particular, high intensity focused ultrasound (HIFU) has been demonstrated for ablating damaged or diseased tissue, such as in cancer treatment; HIFU requires high acoustic pressures and intensities to achieve these effects (**Table 13**). These high acoustic pressures and duty cycles result in increased thermal effects. More broadly, though, applied FUS can induce heating by inducing a material to compress and expand in response to ultrasonic pressure waves [99, 100]. These small movements lead to localized microshearing and the friction from this process results in localized heating and wave attenuation [100-102]. In these instances, the magnitude of this effect depends on both the frequency emitted by the ultrasound transducer and by the material properties of the affected material. The effect has been demonstrated for tissue ablation applications, as well as for inducing responses from thermally-responsive polymers [56].

Parameters	***Brightness-mode ultrasound***	***High-intensity focused ultrasound***
Frequency	2 – 10 MHz Cadet [1, 2]	>1 MHz [3]
Acoustic intensity	< 200 mW/cm2 [2]	>5 W/cm2 (typically, > 1000 W/cm2) [3, 17, 18]
Peak negative pressure (PNP)	< 1 MPa [2]	
Pulse repetition frequency (PRF)	0.5 – 20 kHz [22]	1-100 Hz [23, 24]

Table 13: Ultrasound parameter ranges typical for B-mode US and HIFU.

In addition, FUS can induce cavitation – the formation, growth, oscillation, and collapse of gas bubbles in a medium [103] – beginning with the formation or presence of cavitation nuclei such as gas pockets, dissolved gasses, or gaseous impurities in crevices or at the interfaces

between materials [103-105]. It can occur as either stable cavitation, when a bubble repeatedly grows and shrinks at a consistent rate, or as inertial cavitation, when the bubble oscillates in size dramatically and then violently implodes. Such instances of inertial cavitation result in momentary high pressures and temperatures – as well as free radicals – at the collapse site, and will radiate energy in the form of broadband acoustic emissions [69, 106, 107].

Bubbles oscillate in size due to changes in pressure, such as those caused by propagation of ultrasonic waves. During low pressure (rarefaction), bubbles expand, while during high pressure (compression), bubbles compress. The maximum radius reached during rarefaction can increase with each oscillation, through a process known as rectified diffusion [108, 109]. As the bubble expands, its surface area grows, allowing gas to diffuse into the bubble; when the bubble compresses, the decrease in surface area results in less gas diffusing out of the bubble, despite the higher internal pressure of the bubble [108, 109]. The amplitude of bubble oscillation increases in parallel to increases in acoustic pressure, as more energy is transferred to the bubble [110, 111]. Whether the bubble experiences rectified diffusion and grows, maintains its initial radius, or shrinks and dissolves into the surrounding medium depends on conditions such as the acoustic pressure, the initial radius of the bubble, and the contents of the surrounding medium [109]. The Rayleigh-Plesset equation can be used to model the dynamics of an oscillating bubble in an infinite, incompressible fluid, and can be used to predict whether a bubble will undergo stable or inertial cavitation [112]:

$$\frac{\mathrm{d}^2R}{\mathrm{d}t^2} = \underbrace{-\frac{3}{2R}\left(\frac{\mathrm{d}R}{\mathrm{d}t}\right)^2}_{\text{Inertial factor}} + \underbrace{\left(\frac{p_G(R) + p_\infty(t) - 2\sigma/R}{\rho_L R}\right)}_{\text{Pressure factor}}$$

where R is the time-dependent bubble radius with initial radius R_0 and maximum radius R_{max}, p_G is the gas pressure in the bubble, p_∞ is the pressure of the liquid (both the hydrostatic pressure and the time-varying pressure), σ is the interfacial tension between the gas and liquid phases at the bubble surface, and ρ_L is the density of the liquid. In stable cavitation, the pressure factor (the second of the two terms) dominates, while in inertial cavitation, the inertial factor (the first of the two terms) dominates.

Bubbles driven at or around their resonant frequency will stably oscillate, expanding to their maximum radius during rarefaction and compressing to their minimum radius in compression. In the case of linear oscillations, assuming that the liquid is incompressible and the amplitude of oscillation is small, the resonant frequency is given by the Minnaert equation:

$$f_0 = \frac{1}{2}\pi\sqrt{3\kappa p_0/\rho}\,\frac{1}{R_0}$$

where p_0 is the hydrostatic pressure; ρ is the density of the liquid; and κ is the adiabatic index, the amount of heat required per unit mass for unit temperature rise [113]. At the resonant frequency, stable oscillation can occur for many acoustic cycles, and induce effects experienced in the surrounding medium including as microstreaming and radiation forces [114] [115]. Microstreaming is when circulating eddy currents are formed in the surrounding medium [108,

111, 114]. This happens because the bubble wall has a displacement amplitude much larger than the displacement of the surrounding medium: gasses are more compressible than liquids [116]. As ultrasonic frequency increases, microstreaming decreases, since the maximum bubble radius decreases [116-119]. It has a variety of therapeutic application, including for disrupting cell membranes and liposomes, denaturing proteins, and increasing drug permeability or distribution [111, 114, 120, 121].

Bubbles driven at frequencies below the resonant frequency can expand to more than twice the resting radius. At a sufficiently high peak negative pressure, the inertia of the fluid surrounding the bubble becomes so great that it cannot change direction as the pressure switches from compression to rarefaction [108, 111]. This results in violent bubble implosion and collapse in a process known as inertial cavitation [100, 122-125]. This collapse can result in shock waves, jets at speeds of 300 to 1000 m/s, localized temperatures over 5000 K, localized pressures in the GPa range, and the fragmentation of the original bubble into smaller gas bubbles that can function as cavitation nuclei themselves [118]. When bubbles collapse, they form spherically diverging shock waves that can travel at very high pressures (> 1 GPa) and velocities near the velocity of sound [116, 120, 126]. Such effects can be harnessed to transport materials or cause surface erosion [115]. Additionally, if a bubble is oscillating near a surface, it will oscillate asymmetrically and experience differential pressures across it [108, 116]; when the bubble collapses, it then collapses asymmetrically, and a microjet forms that traverses the bubble and perpendicularly pierces the nearby surface [108, 116]. Because of the considerable implosive pressure caused by bubble collapse, these microjets can travel at speeds ranging from 300 to

1,000 m/s [116, 127]. Such microjets can similarly be harnessed for surface erosion applications, selectively forming holes in membranes and surfaces [116].

Thus, these FUS-induced cavitation effects occurrences can induce acoustic streaming, shearing, microjets, and shock waves, and can be used for increasing drug delivery or inducing microparticle fracture.

3.2 Methods

3.2.1. Design strategy for ultrasound-responsive microcapsules

To develop a clinically impactful method for triggerable localized delivery, it was necessary to ensure that there is significantly greater drug release when ultrasound is applied compared to passive release. We relied on the dextran-PEGDA microcapsules, as described in Chapter 2, as the injectable drug-loaded device. To optimize the response to applied FUS, we tuned the parameters of the applied focused ultrasound, most notably power, duty cycle, and frequency (**Table 14**).

Parameter	*Definition*	*Effect on inertial cavitation*	*Explanation*	*Range tested*
Power	Wattage to the transducer.	Increasing power → more inertial cavitation	Higher power is equal to higher acoustic pressure. Larger peak negative pressure results in the bubble growing larger and collapsing more violently/being more likely to collapse.	10 – 150 W
Duty cycle	Time signal is on / total cycle length	Range: 1-5%: inertial cavitation 5-30%: increasing amounts of heating	With a larger duty cycle, the beads are exposed to more ultrasound per period and thus have more time to grow via rectified diffusion. However, at high duty cycles (above 10 or 20%), heating effects dominate. As such, duty cycle is typically kept low (< 10%).	1 – 30 %
Frequency	Oscillations per second	Increasing frequency → less inertial cavitation	Because the direction of the pressure wave changes more quickly with higher frequency, the beads cannot grow as much, resulting in less rectified diffusion.	1.1 or 3.3 MHz

Table 14: FUS parameters which determine whether heating, cavitation, or no effects occur.

3.2.2. Development of focused ultrasound *in vitro* testing environment

Our ultrasound was generated by a variable drive box connected to a concave focused transducer, with an impedance matching network that matched the generator with the transducer's output impedance to maximize the electrical output power transmitted into the transducer (respectively, TPO102 and H102; Sonic Concepts; Bothell, WA). The transducer had a 63.2 mm radius of curvature and was fitted with a 17.5 mm active diameter hydrophone in its central opening (Sonic Concepts; Bothell, WA). The hydrophone was a passive cavitation detecting hydrophone designed to be sensitive to a broad bandwidth – 10 kHz to 15 MHz – and is intended to measure harmonics radiating from high intensity focused ultrasound (HIFU) focal

areas and as a passive cavitation detector. The transducer was fitted with a polycarbonate coupling cone (C101; Sonic Concepts; Bothell, WA) filled with degassed water, and was placed within a degassed water bath for all experimental runs. All degassed water was prepared by boiling deionized water on a hotplate at 300˚C for at least one hour, until no bubbles were observed leaving the water; the water was allowed to cool completely before being used in the coupling cone.

A custom-printed holding piece was mounted onto the transducer's coupling cone; a Polydimethylsiloxane (PDMS) sample well was fabricated to fit into the holding piece, ensuring alignment with the focused ultrasound transducer. The microcapsules were cleaned by a series of six washes with deionized and degassed water, and then a sample of 24 microcapsules was transferred into the PDMS well, along with 25 µL of deionized and degassed water. The number of microcapsules used throughout testing corresponds to the scale of microcapsules likely for *in vivo* applications and ensures a reliably detectable signal. The wells were then covered with thin plastic film and placed into the transducer holding piece, oriented so that the plastic membrane was on the bottom of the well.

3.2.3. Validation of FUS effect on preseeded material

We received custom fabricated gas vesicles curtesy of the Shapiro Lab at California Institute of Technology [128]. To fabricate alginate-vesicle beads, we made a solution of 1.5% MVUP Alginate (Novamatrix; Sandvika, Norway) with 50% vesicles and loaded it into a 1 mL

syringe. We pumped the syringe at 26 µL/min, through a 23G needle, and dripped it into a 100 mL beaker of slowly stirring 10% $CaCl_2$ solution to crosslink. We fabricated PEGDA-vesicle beads on the microfluidic chip with two co-flowing junctions: the pure vesicle solution pumped into the first inlet, and the same PEGDA and oil solutions pumped into the chip as outlined in Chapter 2.

3.2.4. Determining extent of FUS-induced thermal effects

To monitor thermal effects, we designed a modified holding piece to fit onto the transducer coupling cone, to accommodate an agar-based sample piece. We selected agar, at 0.6% concentration, for this *in vitro* demonstration to mimic the density and thermal conductivity of tissue. Molds to hold the agar and the thermocouple were fabricated from PDMS, with the PDMS mold formed using a custom 3D-printed guide piece. The mold was filled with 0.6% agar composition halfway. After 5 minutes to let the agar begin to set, a thermocouple (5SC-TT-K-40-36; Omega Engineering; Norwalk, CT) was placed from the top to the center of the mold. One bead was placed on the agar so that it was touching the thermocouple. One drop of agar was placed on the bead to ensure the bead remained in place when filling the remainder of the mold. That was allowed to start setting for 1 minute before the rest of the mold was filled. After filling, the agar was allowed to set for at least 30 minutes.

The agar and thermocouple were then placed on the ultrasound transducer and either run with 20% duty, 5% duty, or no FUS (negative control) at 100 W for 30 seconds. Time points

were taken with a Thermocouple Amplifier MAX31855 Breakout Board (DigiKey; Thief River Falls, MN) and UNO (Arduino; Somerville, MA). Time points were collected from 5 s prior to Digi Key the FUS application, throughout the 30-second application of FUS, for an additional 5 s after the application completed.

3.2.5. Assessment of ultrasound-induced drug release profiles

Once prepared, the transducer and mounted sample were submerged into a water bath of deionized water and are exposed to pulsed FUS. After the FUS application finished, the transducer and mounted sample were removed from the water bath and the plastic membrane was carefully removed from the well to allow for sample collection.

Effluent samples were collected at the 0 timepoint, as well as immediately before and after each FUS application, and transferred to a 384-well flat clear bottom polystyrene microplate (Fisher Scientific; Waltham, MA). The plates were then tested for fluorescence using a plate reader (λ_{ex}=490 nm, λ_{ex}=525 nm). All collected effluent was replaced at each time point with an equal volume of degassed and deionized water. Between FUS applications and sampling, the wells are kept covered to minimize evaporation and incidental light exposure.

3.2.6. Cavitation detection

To monitor potential cavitation effects, the data was collected using a SDS 1202X-E oscilloscope, with sampling frequency of 50 Msa/sec (Siglent Technologies; Solon, OH). The data was passed through a SR445A pre-amplifier with a gain of 5 (Stanford Research Systems; Sunnyvale, CA). The data was then filtered using a 1.8 MHz high pass filter (Thorlabs; Newton, NJ). The data was further filtered using the Scipy package in Python, wherein we passed the data through a comb filter to remove the harmonics of the 1.1 MHz transducer, and then took the fast Fourier transform (FFT) of the filtered data.

3.3.7. Structural effects of applied FUS

Prior to undergoing ultrasound applications, the microcapsule samples were imaged on an inverted fluorescent microscope with a DFC7000 camera (Leica Microsystems; Buffalo Grove, IL). After the FUS applications, the microcapsules were transferred via 1000 µL micropipette into a well of a 96-well plate, which had been prefilled with 100 µL of degassed and deionized water.

3.2.8. Statistical analysis

All statistical testing was performed using Graphpad Prism 9 software (GraphPad, San Diego, CA). Where data was assumed to be normally distributed, values were compared using a one-way ANOVA for single variable with a Sidak post-hoc test applied for multiple comparisons. Where data was assumed to be normally distributed, values were compared using a

two-way ANOVA for more than one variable with a Tukey post-hoc test applied for multiple comparisons. Error bars represent standard deviation with n = 3.

3.3 Results

3.3.1. Design strategy for ultrasound-responsive microcapsules

Cavitation is more likely to occur, and requires less FUS application to occur, in heterogenous media or at interfaces, indicating that cavitation is inducible within microcapsule structure as fabricated in Chapter 2 (**Fig. 15a**). In homogenous media, including tissue, there is a lack of the structural impurities and weak points which can act at nucleation sites. In contrast, heterogenous media oftentimes has dissolved gasses present which form into bubbles when exposed to ultrasonic pressures of sufficient intensities and durations. Additionally, the interfaces between materials typically have gaseous impurities which can more easily be disrupted [100, 122, 123].

In a soft material, cavitation bubbles can spontaneously form if the surrounding pressure becomes lower than the saturation vapor pressure [124]. Furthermore, cavitation bubble growth in gels at least partially corresponds to stiffness; rather than oscillate and collapse as in a liquid, a cavitation bubble in a soft material may experience enough confinement to become toroidal, and then destabilize, fracture, and cause material erosion [124, 125]. Therefore, devices made from soft materials, without any incorporated seeding material, can still experience inertial cavitation with the application of ultrasound. This technique can potentially allow for deeper tissue

applications or more extended application periods within the body, although prior demonstrations typically rely on very high peak negative pressures [129]. Therefore, biphasic dextran-PEGDA microcapsules are soft structures within which cavitation nuclei will form and implode under certain ultrasound conditions. When FUS is applied, bubbles grow and cavitate throughout the microcapsule, and can cause sufficient material destruction to allow for a rapid release of a small molecule from the core into both the shell and the surrounding environment (**Fig. 15b**). This microcapsule has a relatively large payload, relative to the volume, which can be released on-demand with the application of FUS at specific parameters (**Fig. 15c**). This is a fundamentally different technology than prior demonstrations of ultrasound-based release, which have focused on microbubble- and contrast agent-enhanced responsiveness; the microcapsules presented herein provide a new drug release strategy with the potential for several improvements over prior methods, including allowing for pulsatile release and for responsiveness over several days.

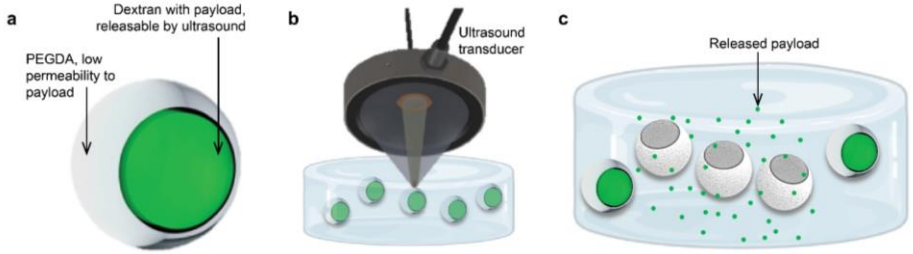

Figure 15: Representative schematic of microcapsule responsiveness to pulsatile FUS application. a) Schematic diagram of the biphasic microcapsule with a dextran inner phase loaded with FITC-dextran as a model drug (green) and a mixed-molecular weight PEGDA outer phase that is impermeable to payload (light grey). b) Schematic diagram of focused ultrasound transducer being used to selectively trigger a microcapsule. The focal area of the transducer is small enough to selectively actuate individual microcapsules. c) After focused ultrasound is applied to the microcapsule, the payload is released into the surrounding environment.

To further adapt our microcapsules to be stimulus-responsive, we have confirmed our material selection and tested the dextran-PEGDA microcapsules for indications of ultrasound responsiveness; we tuned the parameters of the applied ultrasound, within the constraints of what is safe for *in vivo* applications, to determine parameters that most reliably elicited an ultrasonically-triggered burst release of the model drug. Specifically, we applied pulsed FUS, which allows for heat dispersion between FUS application, and thus minimizes risk of tissue ablation. Additionally, we applied FUS at 1.1 MHz, a wavelength that can penetrate several cm into tissue.

3.3.2. Development of focused ultrasound *in vitro* testing environment

A turnkey transducer power output (TPO) system drive box – programmable by power, burst length, pulse length, and frequency – was connected to an impedance matching network that ensured an impedance of 50 Ω, $\vartheta \approx 0$ at 1.1 MHz (**Fig. 16**). The transducer and inset hydrophone were encased by the polycarbonate coupling cone, which was filled with fresh degassed and deionized water daily. Furthermore, all runs occurred with the transducer and attached sample submerged within a DI water bath. Using the coupling cone and surrounding water bath ensured impedance matching throughout the range of the ultrasound transducer and mimicked the impedance of tissue.

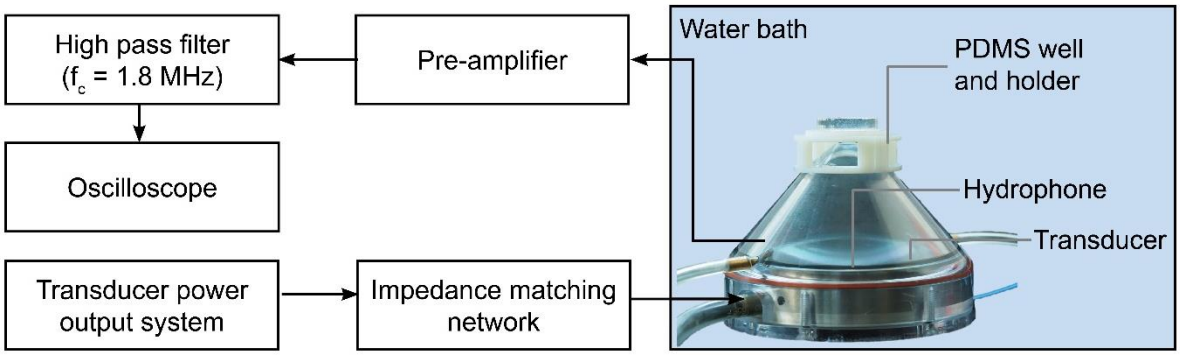

Figure 16: Focused ultrasound test setup and resulting cavitation-related data. a) Block diagram of the focused ultrasound experimental setup, including both the FUS exposure setup and the connecting data filtering and collection components.

The focal area of the of transducer centers 51 mm from the transducer's surface; the focal area has a width of 1.37 mm (in the x-y axes) and length of 10.21mm (in the z axis). The edges of the focal area are slightly tapered, consistent with the curvature of the transducer. For

consistent and maximized FUS effects on the microcapsules, it was critical to ensure consistent sample alignment directly in the focal area. In addition to designing and printing the custom holding piece, we experimented with a variety of well designs and geometries (**Fig. 17**). To optimize for cavitation effects while allowing for sufficient solution volume as to have a detectable release profile, we determined the optimal well dimensions to be a cylindrical form with a 2.5 diameter and 4 mm depth. The microcapsule well was fabricated in PDMS because the acoustic impedance of PDMS is similar to that of water, minimizing the amount of wave that is reflected at the water-PDMS boundary and helping prevent the formation of standing waves [130].

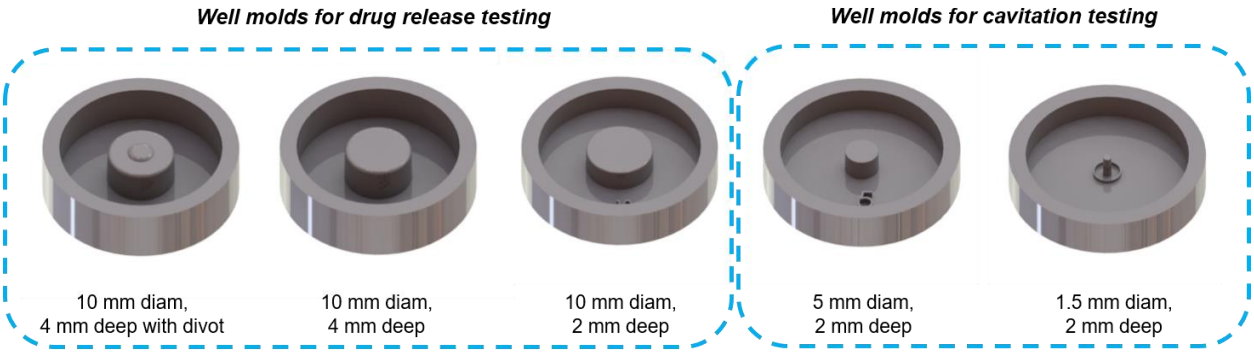

Figure 17: Molds for PDMS wells.

3.3.3. Validation of FUS effect on preseeded material

As a positive control on the effect of pulsed FUS, within the focal area, on a soft capsule, we fabricated alginate-vesicle beads using an extrusion method and PEGDA-vesicle beads using microfluidic fabrication, as described in **Table 15**.

Inlet port	*Composition*	*Flow rate (µL/min)*
Inner dispersed phase	Pure vesicles	(0.9 µL/min)
Outer dispersed phase	PEGDA 10k Da (20% w/v) + PEGDA 575 Da (30% v/v) + 2.5% Darocure 2959 (w/v)	(0.5 µL/min)
Continuous phase	Light mineral oil + 3% Span 80 (v/v)	(12 µL/min)

Table 15: Composition of PEGDA-vesicle capsules.

The resulting alginate-vesicle beads were mushroom-shaped because the vesicles caused the droplet to float when it hit the surface of CaCl2 solution during the drip extrusion fabrication process; additionally, the vesicles appeared as black imaged in brightfield (**Fig. 18a**). The PEGDA-vesicle beads similarly appeared black in brightfield images because of the inclusion of the vesicles (**Fig. 18b**). In contrast, the alginate-only beads were entirely spherical and clear when fabricated in the same manner (**Fig. 18c**). We placed three beads of a given type into the PDMS well for each FUS test and aligned the loaded PDMS well within the aligned mounting piece.

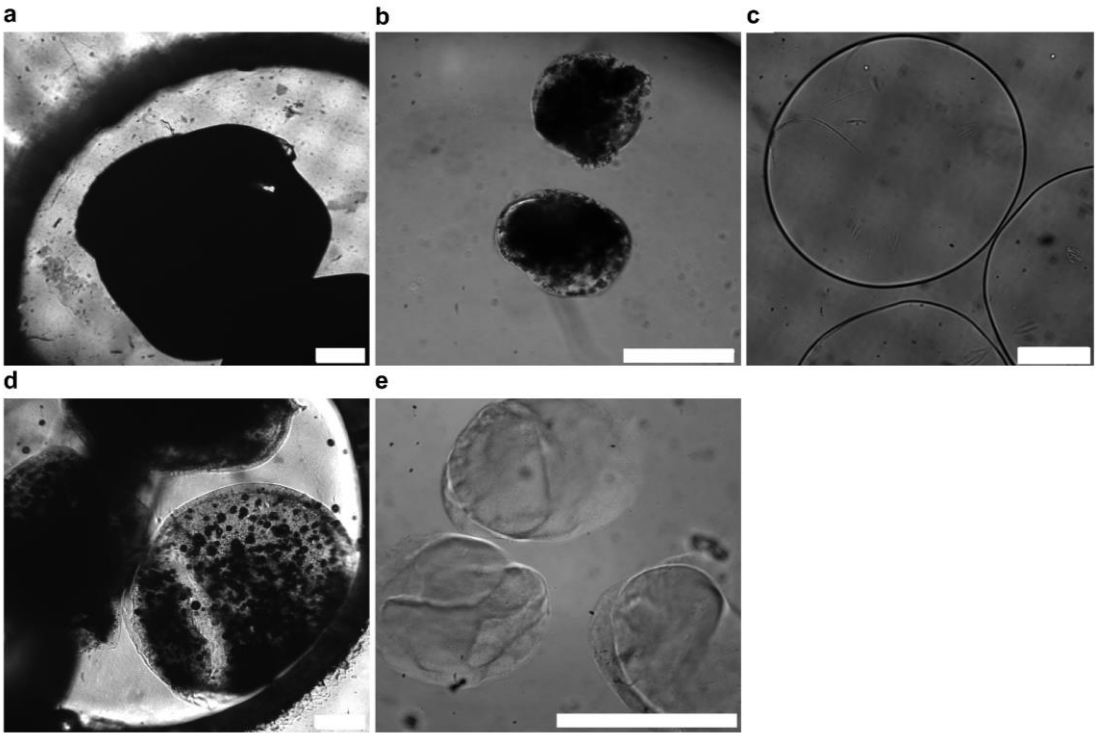

Figure 18: Vesicle-loaded samples undergoing FUS. Vesicle-loaded alginate capsules pre-FUS (a) are darker than the same capsules post-FUS (b), and without vesicles (c) for comparison. Alginate-vesicle beads are images within the PDMS well (which appears as the partial ring in images). Similarly, PEGDA-vesicles appear much darker pre-FUS (d) compared to post-FUS (e). Scale bars are 400 µm.

While the vesicles remained stable for several weeks within the beads [128], applying three periods of 30 s pulsed FUS, at 3% duty cycle, 1.1 MHz, and 100 W caused a visible decrease in the concentration of vesicles within the beads. In the alginate beads, the vesicles density visibly decreased along the outer portion of the bead in particular (**Fig. 18d**), while vesicles appeared to have burst almost in entirely within the PEGDA beads (**Fig. 18e**), based on their transparent appearance post-FUS. Given the difference in volume of the two types of beads

– because of the difference in fabrication technique – it was unclear whether the apparent difference in responsiveness of the vesicles within the alginate and PEGDA beads was due to material properties of the alginate and PEGDA, respectively; volume discrepancies; or differences in vesicles concentration due to fabrication technique. Nevertheless, this demonstration confirmed that applying pulsed FUS at the aforementioned parameters was sufficient for disrupting preseeded soft materials.

3.3.4. Determining extent of FUS-induced thermal effects

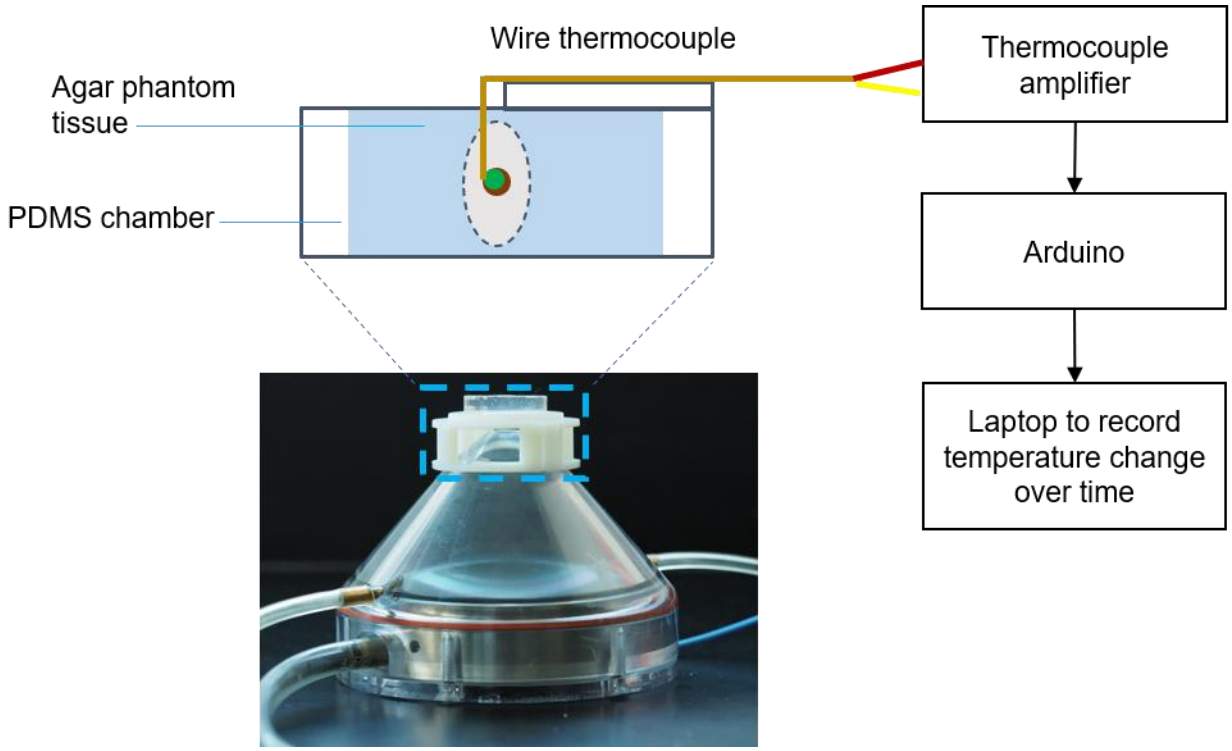

Figure 19: Thermal responsiveness to FUS application. Experimental test setup for assessing the associated thermal effects from the FUS application. This is a modification of the setup used for cavitation and release profile experimentation, to allow for the placement of a thermistor within immediate proximity to a microcapsule. In the above diagram, the focal area of the transducer is shown within the dotted ellipsoidal area.

The microcapsules were exposed to pulsed FUS at a variety of acoustic parameters within the modified mounting setup (**Fig. 19**); the duty cycle, power, application time, and frequency were adjusted independently. Increasing the power or total application time, while keeping the duty cycle low, typically corresponds to relatively high levels of inertial cavitation and minimized thermal effects.

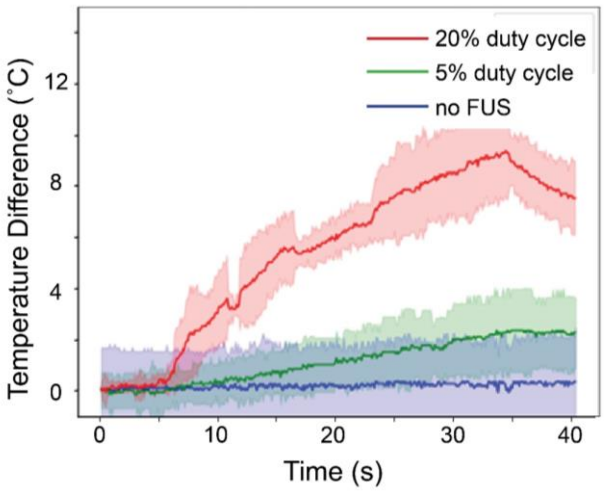

Figure 20: Real-time recording of thermal changes during 100 W FUS applications. The data was recorded beginning 5 seconds before a 30 second period of applied pulsatile FUS, at varying duty cycles. The shaded regions represent the 95% confidence intervals (n = 3).

Applying FUS at an intensity of 100 W, we observed no significant difference between the samples undergoing FUS at 5% duty cycle and the negative control (**Fig. 20**). In contrast, when we applied a 20% duty cycle, which we would expect to induce thermal effects, we recorded significant changes in temperature immediately adjacent to the microcapsules. This temperature increase occurred beginning in the very first FUS burst cycle and increased consistently over the course of the 30-second FUS total time. When the FUS application concludes, the average temperature of samples undergoing 20% duty cycle rapidly reduced, and the average temperature of samples undergoing 5% duty cycle began to slightly decrease.

When we increased the FUS power intensity to 150 W, we observed an increase up to 2˚C when applying a 5% duty cycle over the 30 s application time (**Fig. 21**). We recorded a

larger temperature increase at a 20% duty cycle than at 5%; furthermore, at the higher duty cycle, on results from initial drug release profile analysis, the temperature spiked erratically, rather than consistently increasing, as occurred at 100 W; at 150 W, the temperature increase for the 20% sample was less than resulting during the 100 W application, which likely relates this erratic temperature spiking. Furthermore, when the 150 W FUS application concluded, the average temperature of samples undergoing both 5% and 20% duty cycle continued to increase. The data demonstrates that FUS applications at this higher intensity are more likely to have thermal effects; to apply 150 W intensity with minimal thermal effects, we must use a low duty cycle and keep the total application time as short as possible.

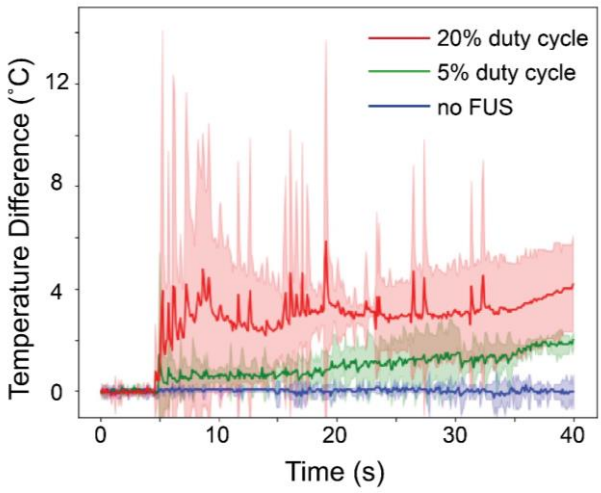

Figure 21: Real-time recording of thermal changes during 150 W FUS applications. The data was recorded beginning 5 seconds before a 30 second period of applied pulsatile FUS, at varying duty cycles. The shaded regions represent the 95% confidence intervals (n = 3).

3.3.5. Assessment of ultrasound-induced drug release profiles

From a release profile perspective, the appeal of these microcapsules as an FUS-triggered method of localized drug delivery is that they do not require preseeding, and thus allow for: firstly, the possibility of a longer usage window once implanted; and secondly, repeatable burst release, such as for therapeutic applications that require repeated dosing. Within this context, we performed a series of release experiments to demonstrate the responsiveness of the microcapsules, the maximum release load, and the ability adjust release amounts by adjusting ultrasound parameters. To assess the impact of these FUS factors, we measured the cumulative release of our model drug from the microcapsule samples over the course of multiple applications of FUS, compared to passive release from the microcapsules when no FUS was applied.

Based on the thermal changes that we observed, we performed release experiments at duty cycles below 10%, to minimize temperature changes in and around the targeted area. Furthermore, we used a high pulse repetition frequency – number of ultrasound pulses emitted by the transducer over a designated period of time – to try to reduce thermal effects. When we applied three bursts of pulsed FUS for 30 seconds every ten minutes at 100 W and 5% duty cycles at a pulse repetition frequency of 210 Hz, we observed an initial on:off ratio of 10x drug release during the first FUS burst, compared to passive release periods (**Fig. 22**). However, this heightened release rate did not reoccur during subsequent FUS bursts. We had high standard deviations in release amounts between samples under these conditions.

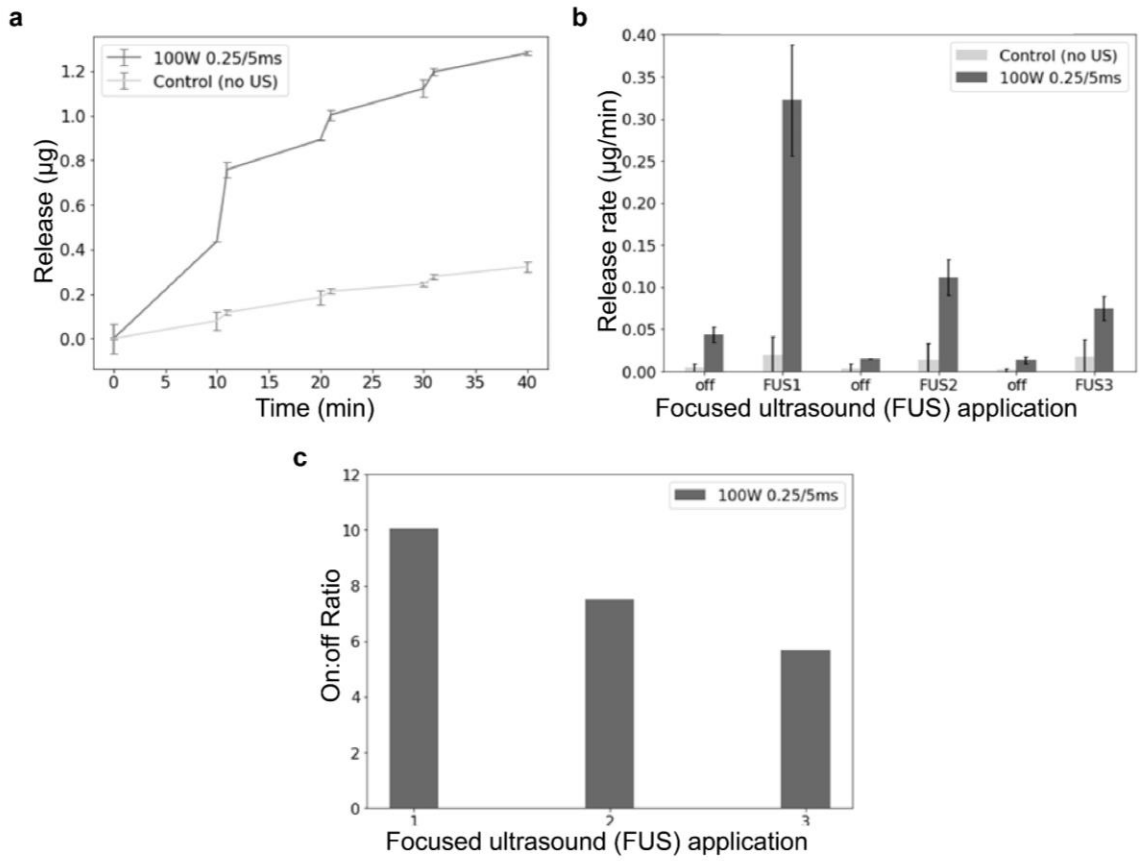

Figure 22: Cumulative release profile (a), release rates (b) and on:off ratio of release rates (c) from a sample of 32 microcapsules, during three cycles of FUS blasts at 5% duty cycle at 100 W.

When we increased the duty cycle to 8% while maintaining a high pulse repetition frequency and 100W intensity, total release and release rates both correspondingly (**Fig. 23A-C**). Under these conditions, the increased on:off ratios occurred during repeated FUS bursts, rather than only the initial burst. However, we still observed high standard deviations in release amounts. Additionally, there was not a significant difference between the cumulative release from microcapsules which underwent FUS and microcapsules which did not. We observed

similar release trends when using both recently fabricated microcapsules, along with microcapsules which had been stored in solution for up to a week, indicating that likely there was negligible pre-seeding effects that may have occurred during fabrication or washing to affect release. We did obtain more consistent steplike release over a greater number of cycles of FUS application by increasing the total length of FUS application periods during subsequent application periods **(Fig. 23D)**.

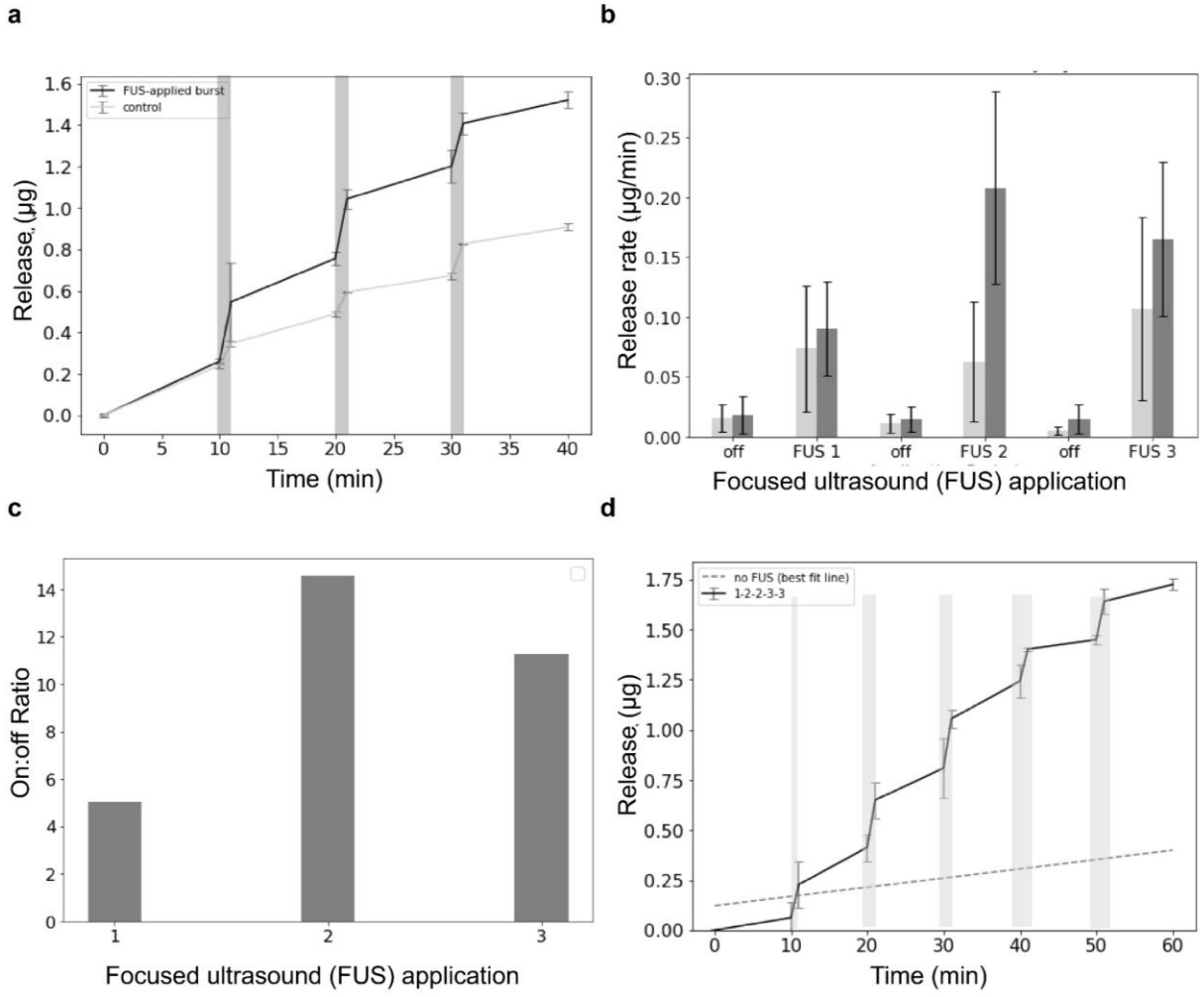

Figure 23: Demonstration of effects of FUS with respect to drug release. Plots A-C show data from FUS applications at 100 W and 5% duty cycle with 30 s FUS applications every 10 minutes. a) The cumulative release of 20k Da FITC-dextran from the microcapsules is shown, where periods of FUS application are demarcated by the grey shading bands (b) The release rates during the 'off' periods, where no FUS is applied, and the periods of FUS application, with the control group in light grey and the experimental (undergoing FUS) group in dark grey. c) Release rate ratios between the off:on periods, for the experimental group. d) Application of pulsatile FUS at the same power and duty cycle, but at increasing time increments of application, with the first application for 1 min, then 2 minutes for the 2nd and 3rd application, and 3 minutes for the 4th and 5th applications. Vertical grey bands indicate application bursts of pulsed FUS.

In subsequent runs, by reducing the pulse repetition frequency to 1.05 Hz, we reduced standard deviation on the release profiles. Likely this was because the longer pulses allowed for more consistent occurrence of inertial cavitation, allowing sufficient pulse durations for cavitation nuclei formation, growth, and collapse. Furthermore, we increased the FUS intensity to 150 W to obtain significantly more cumulative release from the microcapsules under FUS than in passive release conditions. Under these refined FUS parameters, we applied a multitude of FUS bursts over three days, to determine the maximum amount of FITC-dextran that can be released by FUS application. As anticipated, high release rates correspond to the periods of FUS application, resulting in stepwise release profile. After 13 FUS bursts, we observed 3 FUS bursts which resembled the releases rates that occur during passive release, indicating that the FUS-responsiveness of the microcapsules was exhausted. By applying 16 periods of 30 s pulsed FUS applications, we released 0.552 ± 0.069 µg of model drug from a microcapsule; over the same multi-day time period, a microcapsule will passively release significantly less, 0.158 ± 0.013 µg of model drug (**Fig. 24a**). The cumulative release between the microcapsules which undergo FUS have significantly greater FITC-dextran release compared to microcapsules which passively release (**Fig. 24b**). We then applied five bursts of pulsed FUS over 8 hours, with 5 s, 30 s, and 60 s burst lengths. There was significantly more cumulative release from the microcapsules which underwent FUS, for all burst length groups, compared to the passive release group (**Fig. 24c**).

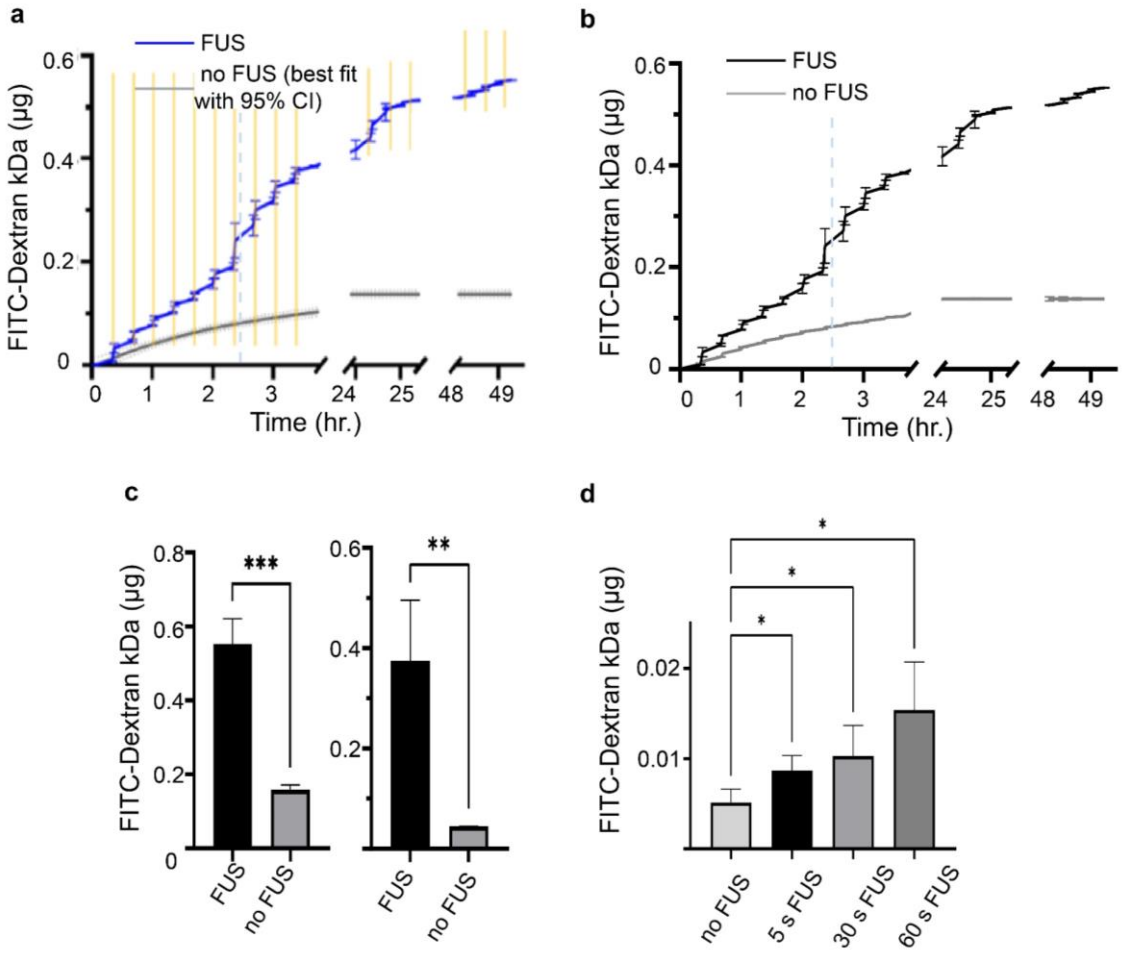

Figure 24: Demonstration of effects of FUS at 150 W and 5% duty cycle. a) The release profile of FITC-dextran from a microcapsule undergoing repeated FUS applications over three days, with each FUS application period shown as a yellow band, compared to a control sample that does not undergo FUS. FUS was applied for 30 s every 20 minutes, for 10 cycles on day 0, and then 3 cycles on days 1 and 2. b) The release profile with a vertical dashed line demarcating the end of the equilibration period for the passively releasing microcapsules. c) Total amount of FITC-dextran released over three days (left) and total amount of FITC-dextran released over three days when excluding the initial 2 hours equilibration period, during which surface leaching occurs (right). ***P < 0.006, **P < 0.0089. d) Average amount of FITC-dextran release from a microcapsule per application of FUS, as measured for different durations of FUS application and averaged over 5 cycles applied every 80 minutes. * P < 0.05.

Finally, we experimented with more comprehensively tuning each of the FUS parameters, namely: power, frequency, blast time, and pulse time (**Fig. 25**). Increasing the power caused a corresponding increase in the release. In contrast, the cumulative release decreased at higher frequency. This behavior is consistent what we would expect for a release profile that is primarily caused by inertial cavitation; the propensity for generating inertial cavitation is inversely related to frequency, while thermal effects are directly related to frequency. Increasing pulse length and burst length corresponded to slight increases in cumulative release.

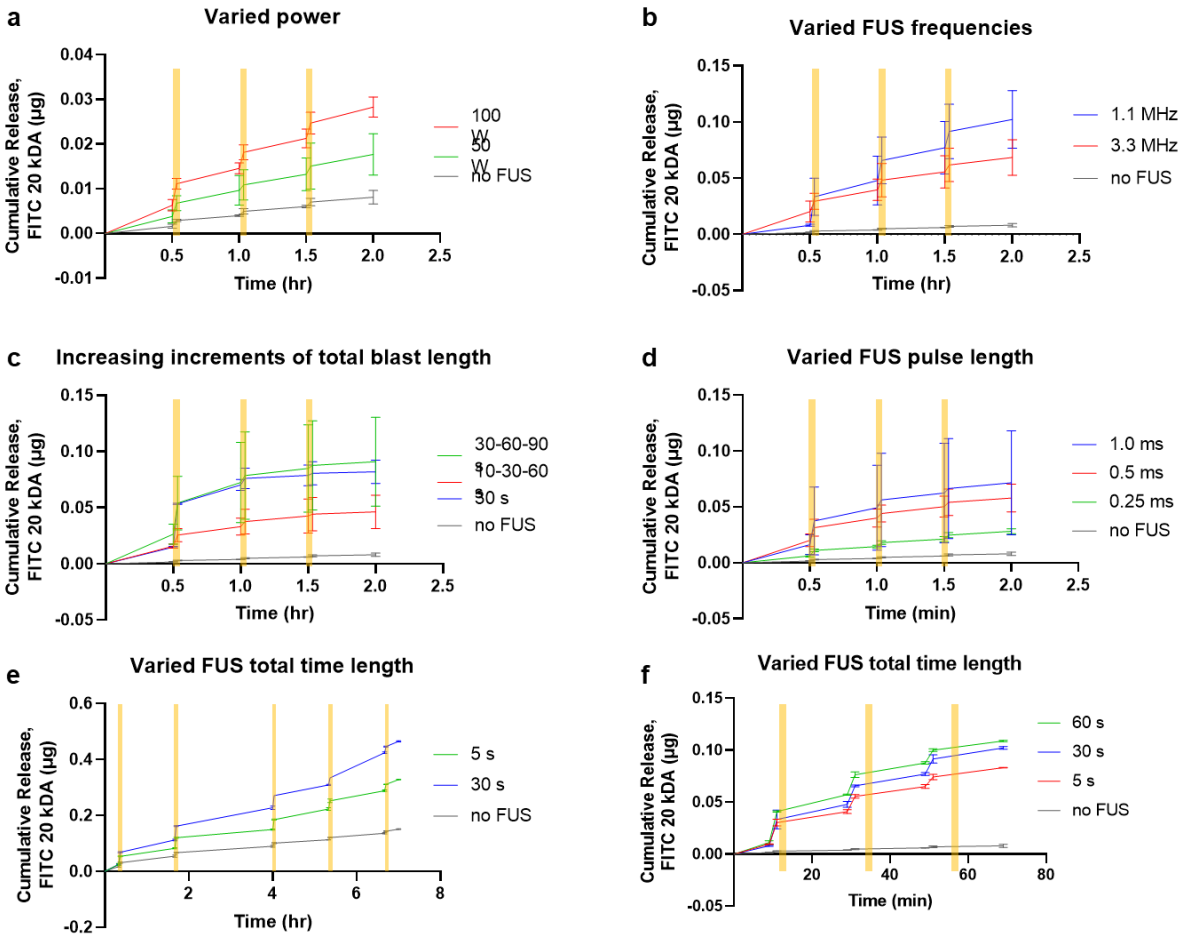

Figure 25: The cumulative release of model drug from a microcapsule, as affected by changing a FUS parameter and compared to a negative control sample that does not undergo FUS. Periods of pulsed FUS application shown as yellow bands on the plots. All experimental runs were performed using FUS at 5% duty cycle. Samples were tested under varied (a) FUS power intensities; (b) f_o frequency, 1.1 MHz, and f_3 frequency, 3.3 MHz; (c) Stepwise increases of the FUS application period, as 10 s for the first application, 30 s for the second application, and 60 s for the third application, as compared to 30 s for the first application, 60 s for the second application, and 90 s for the third application, and compared to samples which undergo 30 s FUS applications for all three blasts; (d) FUS pulse lengths; (e) FUS application times with long periods between FUS applications; and (f) FUS application times with short periods between FUS applications.

3.3.6. Cavitation detection

To assess for occurrences of inertial cavitation, we analyzed the acoustic emissions (**Fig. 26**), as detected by the hydrophone transducer and passed through the high pass filter and amplifier. If stable cavitation occurs, it is noticeable in frequency domain graphs, or spectrum plots, as harmonics of the transducer's operating frequency; stable cavitation occurs because air bubbles are oscillating at harmonic frequencies of the transducer. In contrast, inertial cavitation appears in the frequency domain as broadband noise, because air bubbles explode, creating shock waves, microjets, and microstreams, which appear as a wide spectrum of frequencies. In our test setup, we anticipated stable cavitation even when using degassed water, since any exposure to a water:air interface allows for dissolved gas to reenter the fluid. Based on our release profile data, we anticipated detectable inertial cavitation when we applied FUS to the microcapsule samples.

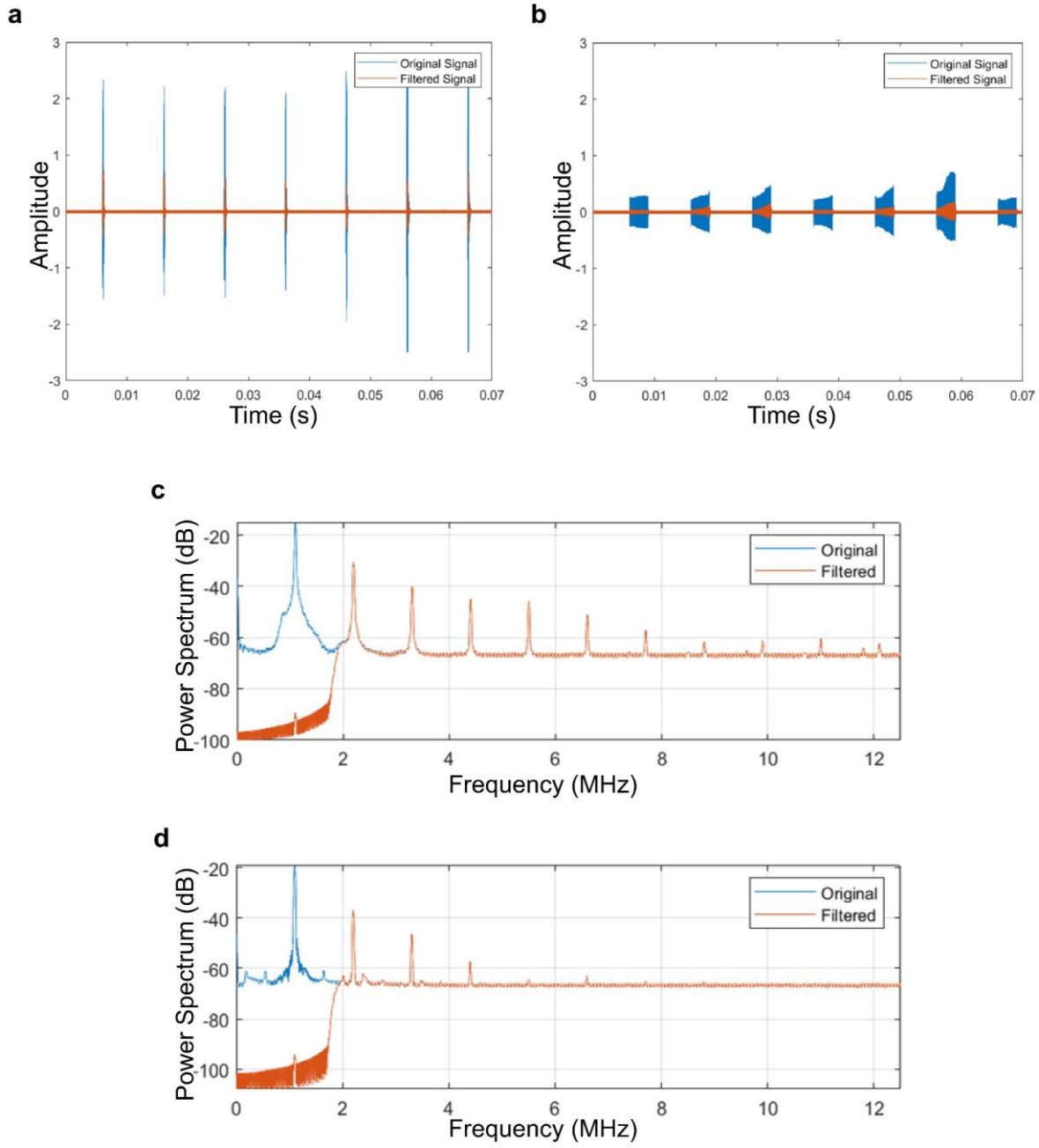

Figure 26: Example signal captured by hydrophone. A time domain sample of 7 FUS bursts is shown, with a 0.2 ms burst length (a) and a 3 ms burst length (b) per every 10 ms, for a 2% and 30% duty cycle, respectively. This same data is shown in the frequency domain, with the 'original' data unfiltered and the 'filtered' data having passed through a 2 MHz high pass filter (c-d).

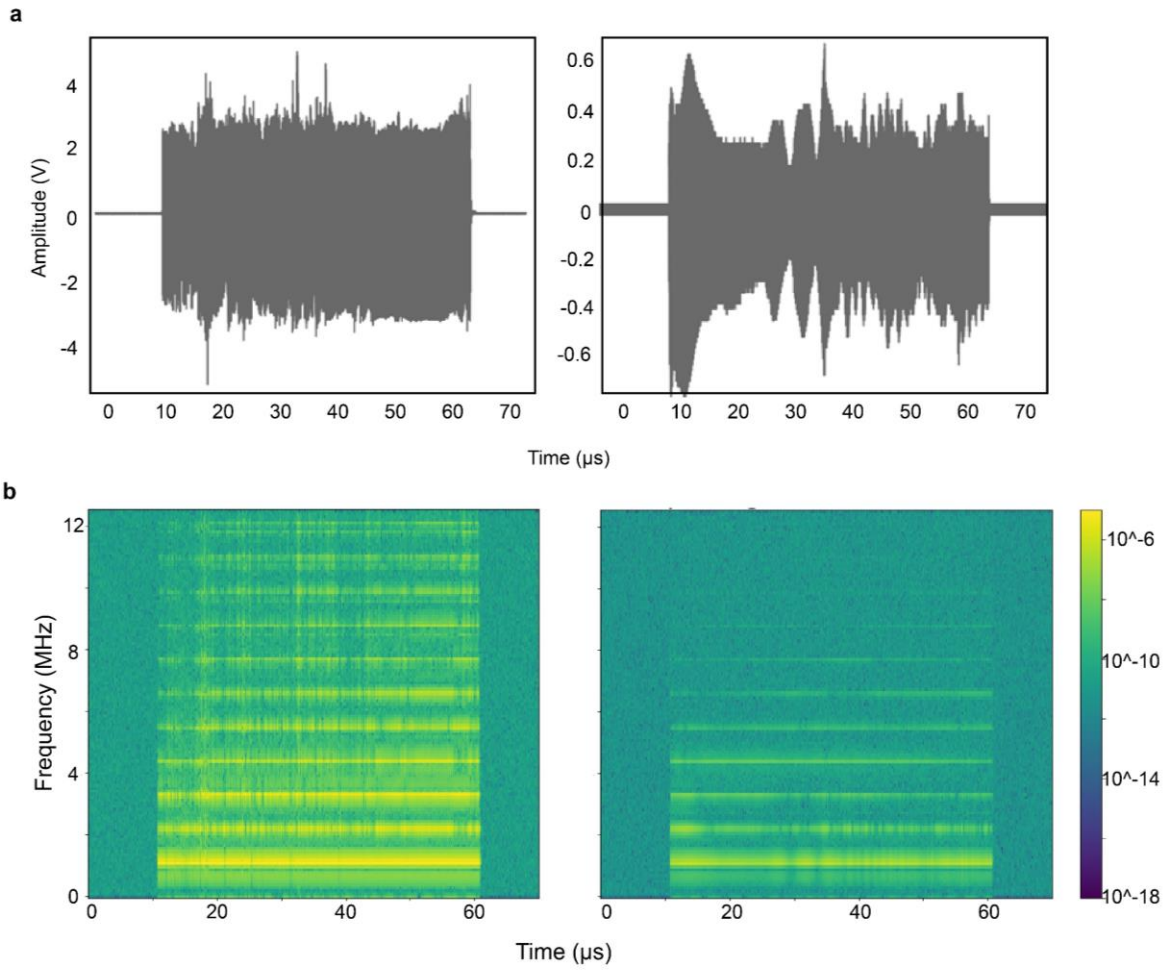

Figure 27: Output of hydrophone-recorded information. a) Recorded output from the hydrophone during a single FUS pulse application, as passed through the amplifier and high-pass filter and recorded via the oscilloscope. b) Spectrograms of a single FUS pulse during a 30 second FUS application from a sample of microcapsules (left) and of degassed water (right), showing the signal strength at various frequencies over time within the respective samples.

The acoustic emissions of the microcapsules, as recorded by the hydrophone during an individual FUS burst. displays a large amount of noise. The time-domain signal displays no

discernable signal in both the microcapsule and water sample when displayed in the time domain, particularly given the amplitude of the harmonic frequencies. Although this data has already passed through the high-pass filter, at 1.8 MHz, and the amplifier, it is expected that the time-domain representation of the data is not clearly interpretable. In the spectrograms, a series of Fast Fourier Transforms (FFTs) of the data is overlapped to visualize the changes in amplitude and frequency of the acoustic emissions over time. The spectrogram shows greater amplitudes across a broad range of frequencies in the microcapsules sample compared to the water control sample (**Fig. 27b**). This increased amplitude occurs throughout the 50 ms pulse period, although particularly for the 15-50ms portion of the pulse. While the bright yellow bands represent the harmonics, the heightened amplitude at frequencies between those bands indicate the occurrence of inertial cavitation.

To confirm this, we plotted the power spectral density during FUS bursts by applying Welch's method to the time-domain data. Welch's method is common method for power spectral density (PSD) estimation, which uses 'a moving window technique': the FFT in each window of the time-domain data and the PSD is then computed as an average of these FFTs values. As shown in the PSD plots, broadband noise occurs in the microcapsule samples undergoing FUS bursts at 150 W, 5%, and 1.1 MHz for 5 s, 30 s, 60 s (**Fig. 28**). We were particularly interested assess whether inertial cavitation occurs at different burst lengths to understand if there was a 'build-up' or phase to consider; that the 5 s burst length sample demonstrated equal amounts of inertial cavitation as the longer burst applications demonstrates that such a delay does not seems to occur for this effect.

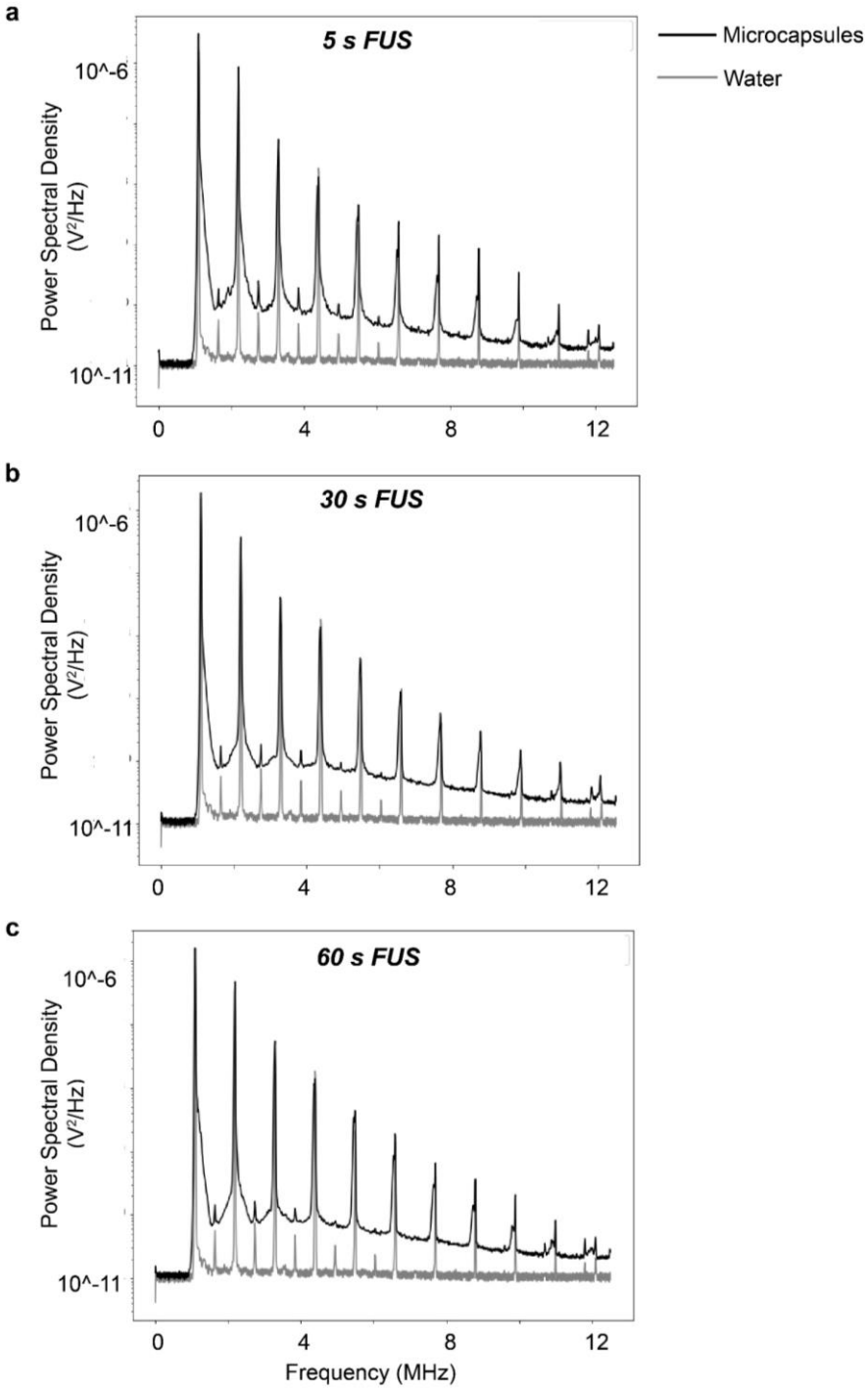

Figure 28: Representative spectral density plots of microcapsule samples compared to degassed water, with the broadband noise occurring at higher amplitudes when the capsules are present indicative of cavitation, recorded during FUS applications of (a) 5, (b) 30, and (c) 60 s.

3.3.7. Structural effects of applied FUS

Inertial cavitation typically causes structure damage, which has facilitated the increased release rate of model drug when we applied pulsed FUS, compared to passive background release from the microcapsules. To investigate how that structural change occurred within the microcapsules, we collected microscope images of the microcapsules between applications of FUS bursts. Under high pulse repetition frequency and 100 W intensity – the conditions where we had observed the sub-optimized release profiles shown in **Figure 22** – we observed only slight changes in microcapsules images before and after undergoing the 3 cycles of pulsed FUS bursts. Namely, some fluorescence compound appeared to migrate from the dextran phase to the boundary of the PEGDA phase, and the entire microcapsule appeared fluorescently brighter (with image exposure conditions consistent) **(Figure 29a-d**). When the microcapsules undergo a more comprehensive number and intensity of FUS applications, the entire dextran inner phase is correspondingly disrupted, with the previously contained fluorescent drug load released into surrounding effluent (**Figure 29e-h**).

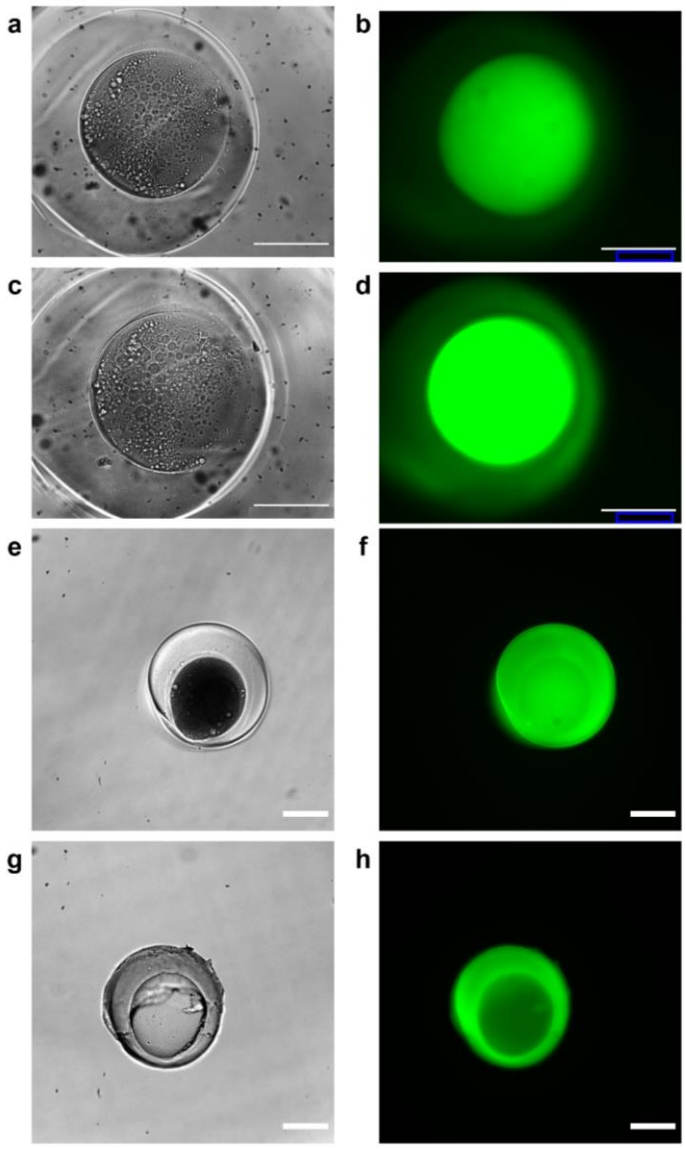

Figure 29: Demonstration of effects of FUS-triggered release profiles. A representative microcapsule shown prior to FUS in (a) brightfield and (b) fluorescence, and after 3 FUS applications at 100 W and 5% duty cycle in (c) brightfield and (d) fluorescence. For comparison, a representative microcapsule shown prior to FUS in (e) brightfield and (f) fluorescence, and after 10 FUS applications at 150 W and 5% duty cycle in (g) brightfield and (h) fluorescence.

For comparison, when we applied FUS on the microcapsules at FUS parameters selected for inducing thermal effects, namely a high duty cycle of 33%, the microcapsules were visibly damaged (**Fig. 30**). This damage, including both surface damage to the PEGDA phase and complete separation of the dextran and PEGDA phases, occurred even at relatively low FUS intensities, including 20 W. However, the visual change to the microcapsules was not consistent across microcapsules and did not correspond to a detectable cumulative release, possibly because the increased temperatures induced fluorescence quenching.

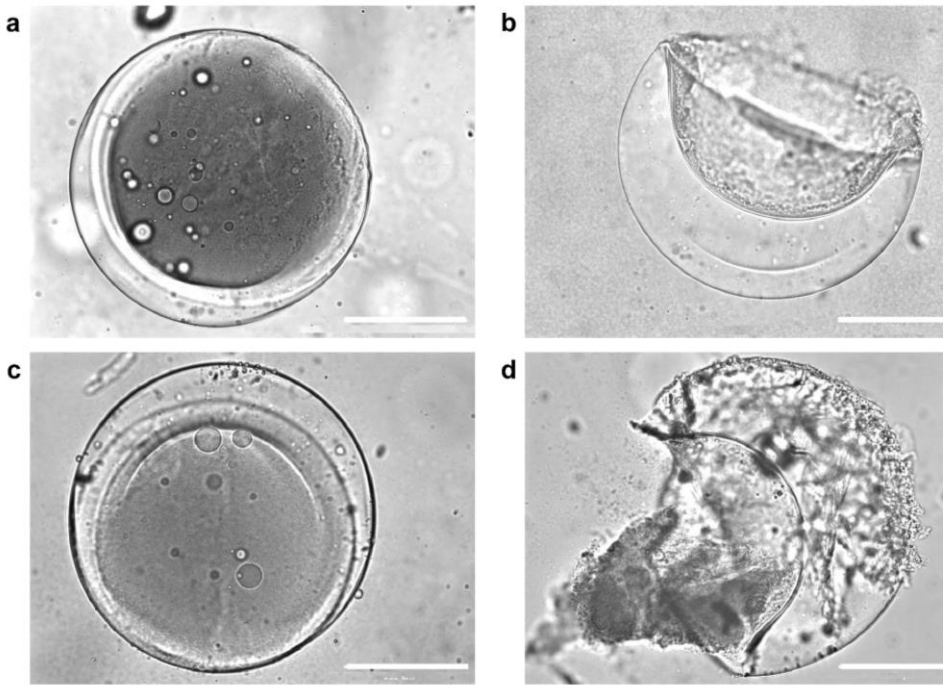

Figure 30: Thermal effects on microcapsules. Microcapsules underwent FUS bursts of 33% duty cycle, at 1.1 MHz and 20 W. Compared to (a) prior to the FUS application, after a 10 s FUS application (b), there the dextran core is disrupted and the inner surface of the PEGDA phase appears changes. Compared to (c) prior to the FUS application, after a 20 s FUS application (d), both the dextran and PEGDA phases appear disrupted. Scale bars are 250 μm.

Under the FUS conditions which yielded significantly increased drug release compared to passive-release control, as shown previously in **Figure 24**, we observed disruption of the microcapsule sample in a consistent manner, with the dextran phase breaking down gradually during repeated FUS bursts (**Fig. 31**) and the PEGDA phase undergoing visible changes the microcapsules approached maximum cumulative drug release (**Fig. 32**). After 5 applications of FUS bursts, the dextran-rich phase of the microcapsules was clearly disrupted. While there were still portions of the dextran-rich phase in microcapsules which had undergone the shorter 5 s FUS bursts, the dextran appeared entirely removed from the microcapsules which underwent FUS burst lengths of 60 s. Furthermore, scanning the surrounding solution at that timepoint, the inner dextran core did not appear elsewhere in the sample well, indicating that it likely was broken down and dissolved into the surrounding solution. After 10 cycles of FUS bursts, the dextran-rich phases do not appear in samples of either burst length. Additionally, the overall brightness of the FITC-dextran in the remaining structure was decreased, with exposure settings consistent.

As shown previously in **Figure 24a,** microcapsules which had undergone 16 applications of FUS bursts over 3 days, for 30 s burst periods, appeared to plateau with respect to FUS-triggered drug release. When examined in microscope images, those microcapsules exhibit pitting and cracking in the PEGDA-rich phase, and did not maintain the dextran-rich inner phase. These images indicate that inertial cavitation may occur at lower applied pressures within the dextran-rich phase, and potentially at the dextran-PEGDA interface; visible effects on the PEGDA-rich phase may only occur after numerous FUS burst applications. While increasing the

FUS intensity may also have caused disruption to the PEGDA phase, we did not test these conditions because we did not pursue parameters which would definitively induce additional heating effects.

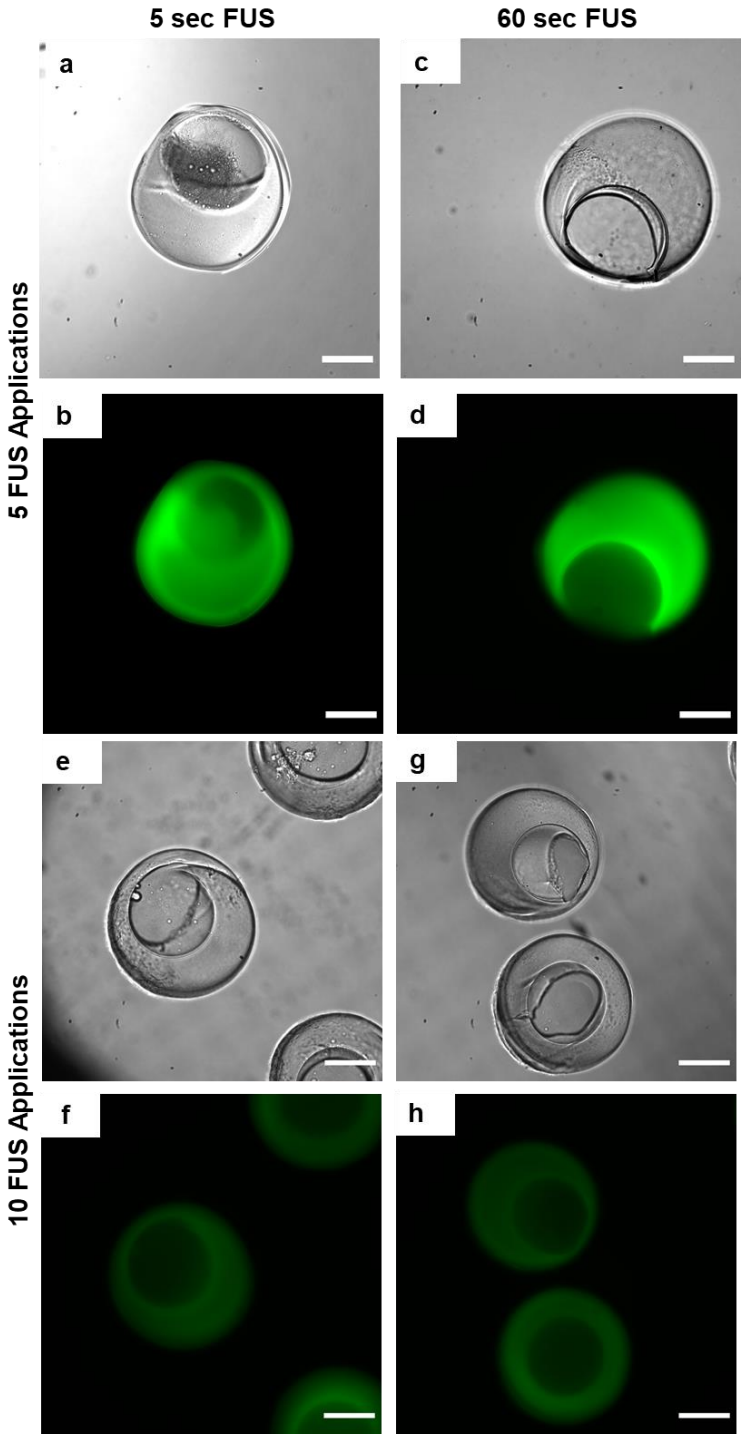

Figure 31: Effect of repeated FUS applications to microcapsules. Images of the microcapsules after 5 pulsed FUS applications for 5 second (a-b) and 60 seconds (c-d) periods, and after 10 pulsed FUS applications for 5 second (e-f) and 60 seconds (g-h) periods. Scale bars are 200 µm.

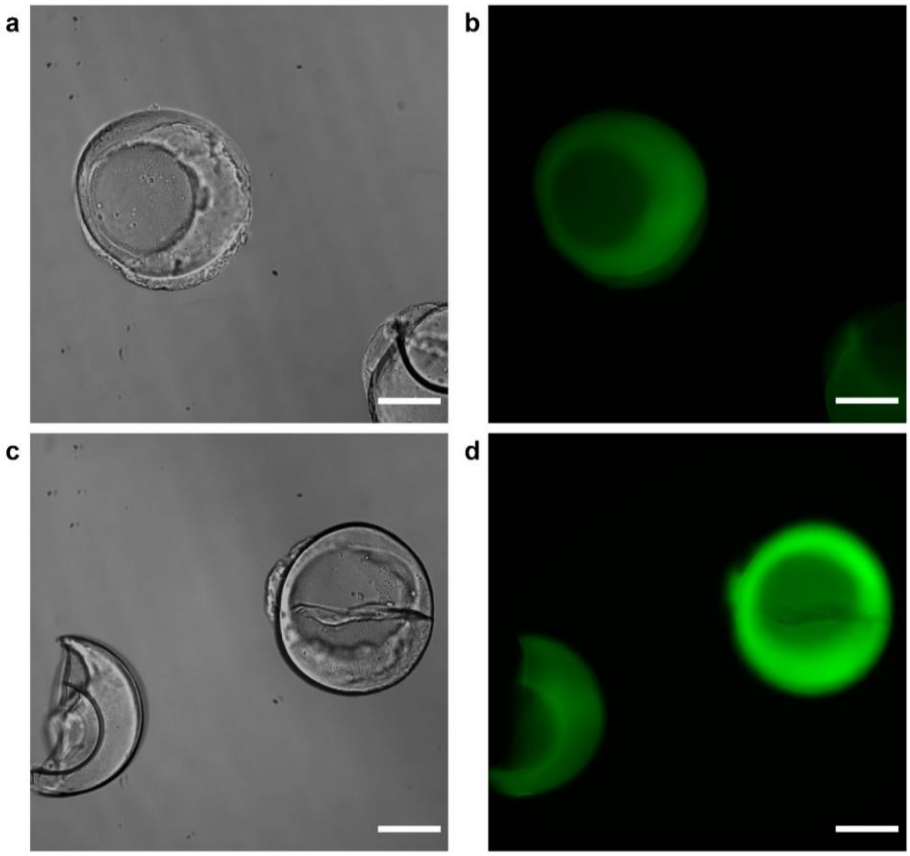

Figure 32: FUS-induced damage to the microcapsules. Images of the microcapsules after 16 applications of pulsed FUS applications, with the dextran portion of the microcapsule fully released. The images show (a-b) pitting in the PEGDA phase and (c-d) cracking of the microcapsule structure. Scale bars are 200 μm.

3.4 Discussion

Considering this release data, in conjunction with the detected thermal effects at 100 W and 150 W, we determined that applying FUS at 150 W, 1.1 MHz, and 5% duty cycle for 30 s burst periods yielded repeatable release. Furthermore, we optimized by using a 50 m**s** pulse length, for a low pulse repetition frequency, that allowed for inertial cavitation to occur more consistently across samples; this reduced the standard deviation of cumulative release amounts, compared to runs performed as shorter pulse lengths.

We have demonstrated a method for inducing repeated dosage releases from the biphasic, biocompatible microcapsules. Due to the presence of broadband noise, the minimal thermal effect at duty cycles which produce notable amounts of release, and the minimal response observed at higher duty cycles, it can be concluded that the release of model drug seems to be primarily caused by cavitation occurring within the microcapsule. The occurrence of cavitation likely causes increased defects, particularly within the PEGDA portion of the microcapsules, which effectively increase the porosity of the microcapsule.

This technology contributes a useful addition to the field of localized drug delivery by allowing for ultrasound-triggered release without the need for cavitation seeding material. In contrast to most prior demonstrations of ultrasound-triggered drug delivery from microcapsules, this technology does not incorporate any form of microbubbles or other forms of pre-seeding cavitation nuclei. This technology has the potential for repeatable localized delivery within tissue

with high spatial and temporal control, due to the precise and small focal area of FUS and the stability of the microcapsules over a multiweek period.

As a future step, we are incorporating gold nanoparticles (NPs) into the microcapsule structure; these NPs will change the minimum applied pressure needed for a structural disruption of the microcapsules, to allow for selective release of microcapsules within close proximity of each other. We hypothesize that such tuning will allow for multiplexed release with this method. Relatedly, future demonstrations may include incorporating a range of drugs with varied molecular weights or with positive or negative charge, as well as *in vivo* demonstrations.

Chapter 4: Integrated demonstration of ultrasound-responsive devices to promote wound healing

4.1 Background

Wound healing is a complex process which is only partially understood; the biological pathways which cause chronic wounds are of particular interest because of their negative impact on the immune system and risk of infection or other complications [57]. Furthermore, such chronic wounds affect more than 6 million people in the United States, with an associated annual cost of $25 billion; challenges to wound healing are a growing issue in the United States, due to an aging population and compounded by increasing rates of obesity and diabetes [131].

Wounds that are healing properly progress through three general phases of development: coagulation-inflammation, proliferation, and remodeling [132]. The coagulation-inflammation phase is characterized by coagulation followed by intense infiltration by inflammatory cells, such as neutrophils and macrophages, which clean the wound by producing high levels of proinflammatory cytokines, protease, and reactive oxygen species (ROS) to kill bacteria [133, 134]. During the next phase – proliferation – keratinocytes, endothelial cells, and fibroblasts migrate to the wound site and proliferate to replace the lost tissue, oftentimes forming scar tissue [135]. Additionally, deposition of the granulation tissue, or extracellular matrix (ECM), occurs [136, 137]. Finally, during the remodeling stage, the fibroblasts present in the wound produce ECM, and the ECM network matures and increases in mechanical strength. In addition to these

phases, it is relevant to note that the reepithelization occurs throughout almost the entire healing process. Furthermore, these phases process over a variable timeframe, from days to years, with stages overlapping (**Fig 33**). Therefore, in clinical environments, a wound may not clearly present as a certain stage of progression.

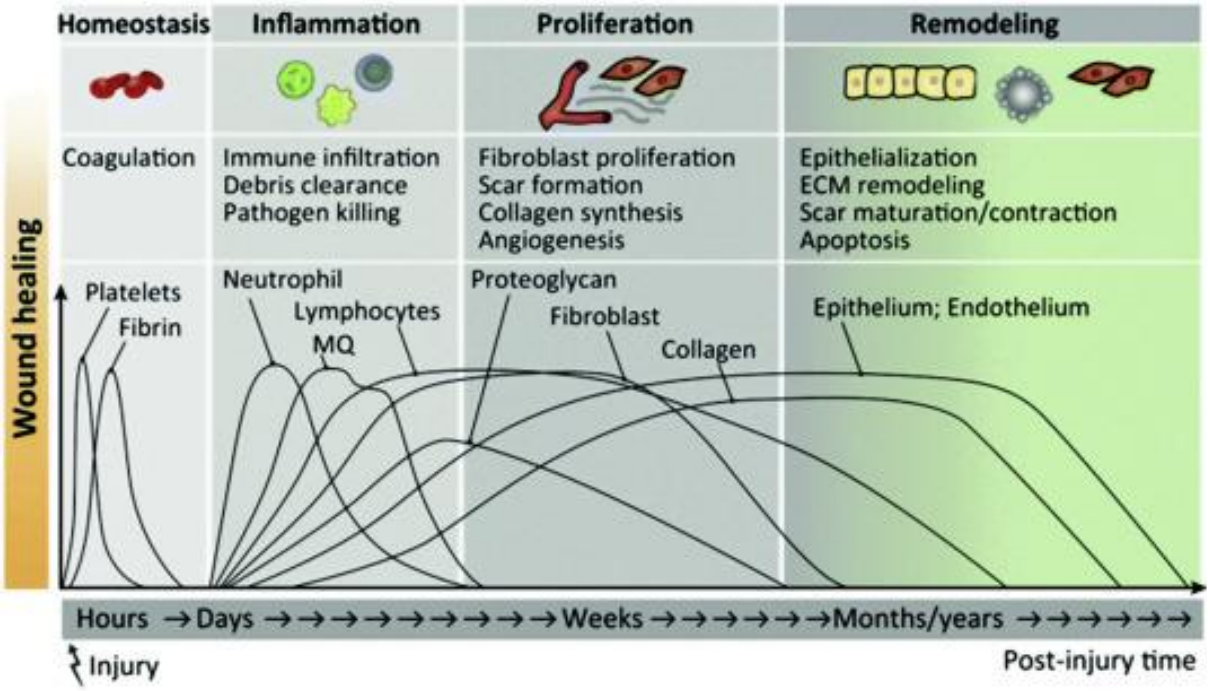

Figure 33: Typical stages of wound healing (from [12], reprinted with permission).

However, chronic wounds typically become fixed in some stage of development, not progressing completely through the healing process; such chronic wounds can form for a variety of reasons, including comorbid conditions, chronicity, and confounding factors [12]. Chronic wounds tend to exhibit persistent inflammation, as biofilms and platelet-derived factors induce

pro-inflammatory cytokines and inflammatory cells. In response, the ROS and protease levels elevate in the wound site, leading to degradation of growth factors and destruction of ECM components [138]. This, in turn, attracts additional inflammatory cells to the wound, promoting the inflammation phase further, and perpetuating the signature consistent inflammation of a chronic wound.

Currently, wound dressings or bandages are one of the most common clinical tools for acute and chronic wound care. However, the majority of existing wound care dressings are passive, and cannot actively respond to variations in the wound environment [134]. As a consequence, patients must be frequently inspected to monitor and assess the healing process. In recent years, there have been a variety of proposed methods for "smart" bandages, which can sense wound conditions and provide insights into the current stage of healing development [139-141]. For instance, a wide range of sensors have been integrated into wound dressings to monitor physical and chemical signals including pH, temperature, oxygen level, moisture, and electrical signals [136, 139, 140, 142-144].

Considering the time-dependency of the physiological processes involved in wound healing, there is an opportunity for a closed-loop system that incorporates sensors and actuators within a wound site, to enable real-time sensing of wound conditions with high spatiotemporal resolution and to responsively administer drugs at the wound site, thereby aiding to accelerate the healing process. Towards this end, we have been collaborating to incorporate the ultrasound-responsive drug-loaded microcapsules into a larger integrated system for promoting wound

healing, consisting of: (1) an active patch device that acts as ultrasound imager, focused ultrasound actuator, electrochemical sensor of pH and metabolites, and electrical stimulator using principles of temporal interference (TI); (2) injectable sub-500-μm "motes" which are powered by the ultrasound imager on the patch and which appear in the ultrasound image, allowing sensing of biomarkers deeper in the wound; (3) the aforementioned microcapsules; (4) active implantable scaffolds infused with the motes and which also incorporate electric field sensing and ultrasound-activated drug delivery from hydrogels; and (5) a machine-learning framework (**Fig. 34**) that communicates wirelessly with the patch device and that "closes" the loop, connecting imaging recognition, surface sensing, and mote interrogation to drive actuation decisions. Within the context of this Specific Aim, we focused on *in vitro* demonstrations of integrating elements of the system, to validate core functionalities of the devices when in proximity to the other components and to cellular constructs.

We performed this work in collaboration with the other 'Treatment and recovery augmented with electrical and ultrasound- mediated actuation and sensing' (TRAUMAS) grant participants, particularly the Hung and Shepard Laboratories at Columbia University and the Zhao Laboratory at Massachusetts Institute of Technology.

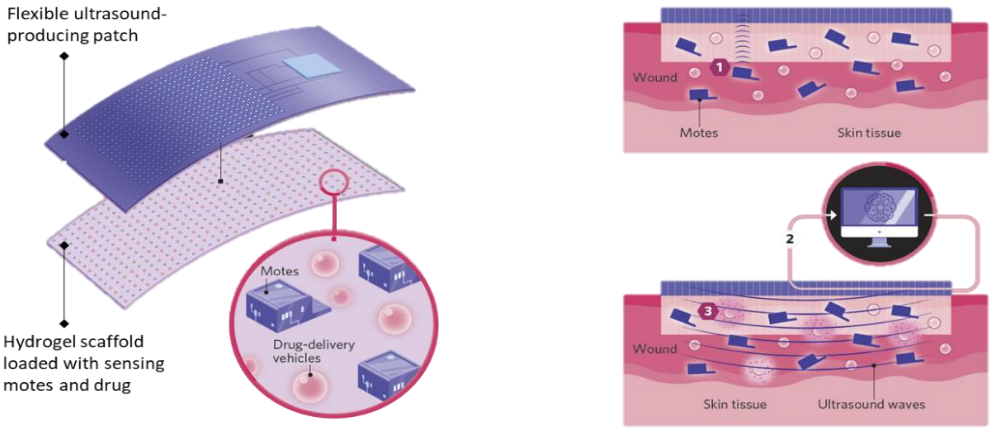

Figure 34: Integrated system for wound healing promotion. A flexible smart bandage sits on the surface of the wound and contains a flexible ultrasound transducer capable of both generating focused ultrasound and receiving acoustic signals. Within the wound site, a sensing electronic mote (left) emits ultrasonic signals with pertinent information regarding the wound microenvironment, while a polymeric drug-loaded device (right) is preloaded with small molecule drug which can be release on-demand, depending on the appropriate application of FUS. (Figure adopted from SEAS Communications team.)

4.2 Methods

4.2.1. Proof-of-concept integration of system components

4.2.1.a. Assessment of available ultrasound transducers

During the course of work for this Aim, we had access to three different ultrasound transducers, which required customized considerations given the diversity in terms of output ranges, focal area dimensions, and housing configuration. To establish a baseline of usage comparison, we operated all three transducers while at least partially submerged in degassed water within a 400 mL beaker.

Firstly, the L12-3 transducer probe (Verisonics; Kirkland, WA) operated using a turnkey system (Verisonics) and accompanying Matlab (MathWorks; Natick, MA) script. The housing of this transducer allowed for ease of use at any angle or orientation, requiring either submersion of the end array in degassed water or coupling gel. For consistency, we used a mounting clamp to maintain a vertical orientation for the transducer throughout all applications. We operated this transducer at a 4 MHz frequency. During operation, we ran a real-time terminal to observe live ultrasound imaging.

Secondly, we applied ultrasound using a flexible 16x16 array, fabricated using a polyimide flexible printed circuit board (Custom design and construction, by the Shepard Laboratory). This transducer was similarly operated using the Verisonics turnkey system and accompanying Matlab script, and applied FUS at peak negative pressures corresponding to the applied voltage. For our trials, we applied 40 V across the array, corresponding to 500-600 kPa. The transducer could also alternatively produce an ultrasound image.

Finally, we tested the H102 single element FUS transducer with an embedded Y107 hydrophone (Sonic Concepts; Bothell, WA) – the operated setup transducer, operated using a turnkey transducer power output (TPO), was previously described in the Methods section of Chapter 3. For the following integration experiments, we operated this transducer at a 1.1 MHz frequency, 5% duty cycle, 30 s burst length, and a range of 10-150 W intensity.

4.2.1.b. Capacities of imaging ultrasound transducer

We constructed an *in vitro* system, initially, within a 400 mL glass beaker. Within the vessel, to simulate tissue and to ensure minimal issues with impedance mismatches, we cross-linked a 200 mL 3% w/v agarose block. We cross-linked the agarose within the beaker to ensure a flush fit. Furthermore, we embedded a 3x3 matrix of 'dummy' mote devices, which can be ultrasonically imaged but provide no readout, on the top surface of the agarose block. On top of the motes, we added another 50 mL crosslinked 3% w/v agarose block, to simulate a dermal layer. Prior to each run, we used tweezer to apply a sample of scaffold structure with embedded liposomes, which had already been loaded with 20k Da FITC-dextran and extensively pre-leached. All scaffold samples were weighed before use, and then a scaffold sample was placed on top of the of the agarose blocks, to act as a bandage layer on top of the 'dermal' agarose. Finally, we pipetted a 0.029% w/v $CaCl_2$ into the beaker, which both stabilized the alginate scaffold structure and aided in ensuring minimum impedance mismatches between the applied transducer and the tissue phantom.

To assess drug release from the scaffold, we collected three 1 mL samples 30 seconds before and after ultrasound applications, as well as at the same time points during a negative control. The 3 mL of effluent was collected as close to the estimated ultrasonic focal area as possible during all runs, and was immediately replaced in the beaker with a corresponding volume of fresh $CaCl_2$ solution.

4.2.1.c. Capacities of flexible focused ultrasound transducer

To accommodate the wide connecting cables of the flexible array, approximately 1.5 cm in diameter, we fabricated a custom 3D-printed 400 mL beaker. The structure incorporated a platform around the beaker lip to facilitate easy mounting of the transducer across the top of the beaker, allowing for consistent alignment and even weighting with respect to the connecting cables. We filled the beaker itself to the brim, to allow for the 16x16 array to be submerged while balancing across the top of the beaker. When collecting solution samples, we lifted the array by the connecting cables, to ensure minimal disruption to the water's surface.

4.2.2. *In vitro* testing of integrated elements

4.2.2.a. Cell monolayer

To perform initial biocompatibility demonstrations of the system, we tested the effects of applying FUS to 35 mm petri dishes containing cell monolayers. Specifically, the petri dishes had a monolayer of 3T3 fibroblasts (Mus musculus) expanded on 35 mm glass bottom dishes, covered by a 2 mm-thick layer of 2% agarose which had been presoaked in media, and then by another 2 mm-thick layer of 2% agarose with a 2 mm diameter hole in the center of the layer. We formed this center hole using a custom printed mold; immediately prior to testing, we filled the punch hole with either a scaffold sample of equal diameter, or 20 hydrogel-based microcapsules.

To observe the effects of FUS on the system in real-time, we designed a custom 3D-printed mount to position the single-element FUS transducer above the 35-mm petri dish on the stage of an inverted microscope (Leica; Allendale, NJ). The custom mount was designed to align the transducer's focal area over the center punch containing the scaffold or microcapsules samples, while still allowing for movement of the microscope stage. Ultrasonic coupling gel was applied on the top of the sample at a sufficient volume as to immerse the bottom portion of the transducer's coupling cone, to ensure minimal changes in impedance between the transducer and the sample. While the addition of the transducer impeded any brightfield functionality of the microscope, real-time fluorescent images and videos were captured using the added microscope camera and LAS-X software (Leica; Allendale, NJ).

In addition to real-time fluorescent monitoring, the samples were kept and we analyzed the cell monolayers using live/dead staining. By imaging the cells after the FUS application, we could investigate whether the applied FUS parameters were so powerful as to cause cell damage.

4.2.2.b. Cell construct

Tissue-engineered skin constructs were made by seeding m3T3 fibroblasts at 10,000 cells/construct; 25,000 cells/construct; and 50,000 cells/construct in 12-well Transwell filters (0.4 µm pore size) (Corning, Corning, NY). The construct dimensions were: 12mm in diameter and 2mm in height. We prepared constructs with both biased (air interface in upper compartment) vs. unbiased (liquid interface in both compartments) feeding. Furthermore,

Matrigel (7 mg/mL) and collagen (4 mg/mL) foundation was tested. The resulting constructs were cultured over a period of 7 days.

For testing with FUS, these constructs were centered in a 35 mm plastic petri dish, on top of a 2 mm thick 2% agarose layer which had been presoaked in media and surrounded by an additional agarose layer with a 10 mm punch to accommodate the construct. We placed a 2 mm thick layer of 2% agarose, with a centered 2 mm diameter hole, on top of the construct layer; during assembly we added up to 50 µL of media, as needed to minimize any noticeable air bubbles between the two layers. Similar to during the monolayer experiments, we used a micropipette to place 10 microcapsules into the punched hole. Once assembled, we placed the petri dish into the transducer mount piece, sealed it with ultrasonic coupling gel, and applied 10 bursts of pulsed FUS.

4.2.3. Release effect from microcapsules into cell construct

4.2.3.a Fabrication of microcapsules loaded with relevant compounds

To form microcapsules loaded with a FITC-conjugated Lipopolysaccharides (FITC-LPS) (F3665; Millipore Sigma, Burlington, MA), we dissolved the FITC-LPS into the dextran solution. We then loaded this solution into a 1 mL syringe, which was prewrapped to minimize light exposure, and pumped the solution into the microchip previously described in Chapter 2. As with prior dextran-PEGDA microcapsules, we applied on-chip UV light to photopolymerized the microcapsules. After fabrication, we performed six rounds of washing in DI water, and then

stored microcapsules samples in degassed DI water or phosphate buffered saline (PBS) (Thermofisher Scientific, Waltham, MA).

4.2.3.b Sterile fabrication of microcapsules

Fabrication of sterile microcapsules required sterile preparation of each fluid phase, followed by assembly and running of the microfluidic chip within the cell culture hood. Firstly, to prepare the sterile dextran solution, we diluted a stock 15% dextran 500k Da solution to make a 3.75% dextran 500k Da solution, and sterilized by autoclaving at 110-115°C for 30 to 45 minutes. In the cell culture hood, we then added 0.50 mL of 3.75% dextran 500k Da to the 1 mg vial of FITC-LPS. To sterilize the PEGDA prepolymer solution, we filtered the solution through a 0.45 µm syringe filter, keeping the vial and syringe covered to prevent light exposure. Additionally, we autoclaved the PDMS microfluidic device and associated tubing on a dry cycle. We then ran the microfluidic chip, including the photopolymerization portion, within the cell culture hood, using sterile technique practices for all equipment.

4.3 Results

4.3.1. Proof-of-concept integration of system components

4.3.1.a. Assessment of available ultrasound transducers

We compared the relevant parameters of the three transducers, according to available documentation. It was important to consider the focal distance and focal area: the imaging

transducer had the smallest focal distance and largest focal area, in contrast to the very narrow focal area of the single element transducer. Additionally, the range of available intensity varied broadly, with the imaging transducer producing minimal intensity, particularly compared to the single element transducer (**Table 16**).

	Verisonics L12-3	***Sonic Concepts H102***	***Custom 16x16 Array Patch***
Transducer type	Linear Array Imaging transducer	Single element focused ultrasound (FUS) transducer	Flexible patch for imaging and FUS
Frequency (MHz)	4	1.1	1.4
Intensity		5 – 150 W (> 1 MPa)	10 – 30 V (400 – 600 kPa)
Purpose	Provides real-time guidance when devices are implanted	Tunable application of FUS with known focal area	Mimics eventual closed-loop system; limited upper limit of applied intensity
Focal distance (mm)	20	51	35

Table 16: Comparison of characteristics for each transducer.

4.3.1.b. Capacities of imaging ultrasound transducer

It is important to ensure that each of the implanted devices, particularly the sensing motes, are ultrasonically visible within the wound site. In addition to the surrounding tissue, the *in vivo* system will incorporate a hydrogel scaffold on the surface of the wound site, for localized

drug delivery. In this *in vitro* setup, we investigated whether the scaffold placement interfered with the ultrasonic visibility of the motes (**Fig 35a-b**). The top and bottom boundary of the scaffold appears clearly in the ultrasound image as the upper two horizontal lines. This appearance is caused by the boundary appearance of the scaffold, not because of a notable impedance mismatch between the scaffold and water, as indicated by the lack of brightness within the scaffold. Nevertheless, as the imaging transducer centered above each mote, it appeared as a white spherical shape within the image, at a higher brightness level than the surrounding boundary conditions (**Fig. 35a-c)**. Furthermore, we measured a linear cumulative release profile from the scaffold during the period of applying imaging ultrasound (**Fig. 35d**), prompting additional measurement of the scaffold's release profile under varied ultrasound conditions. Furthermore, we noted that the motes were only visible when we oriented the transducer directly over and in alignment with the motes; when multiple motes were present, they were only visible if the motes were implanted along a single axis.

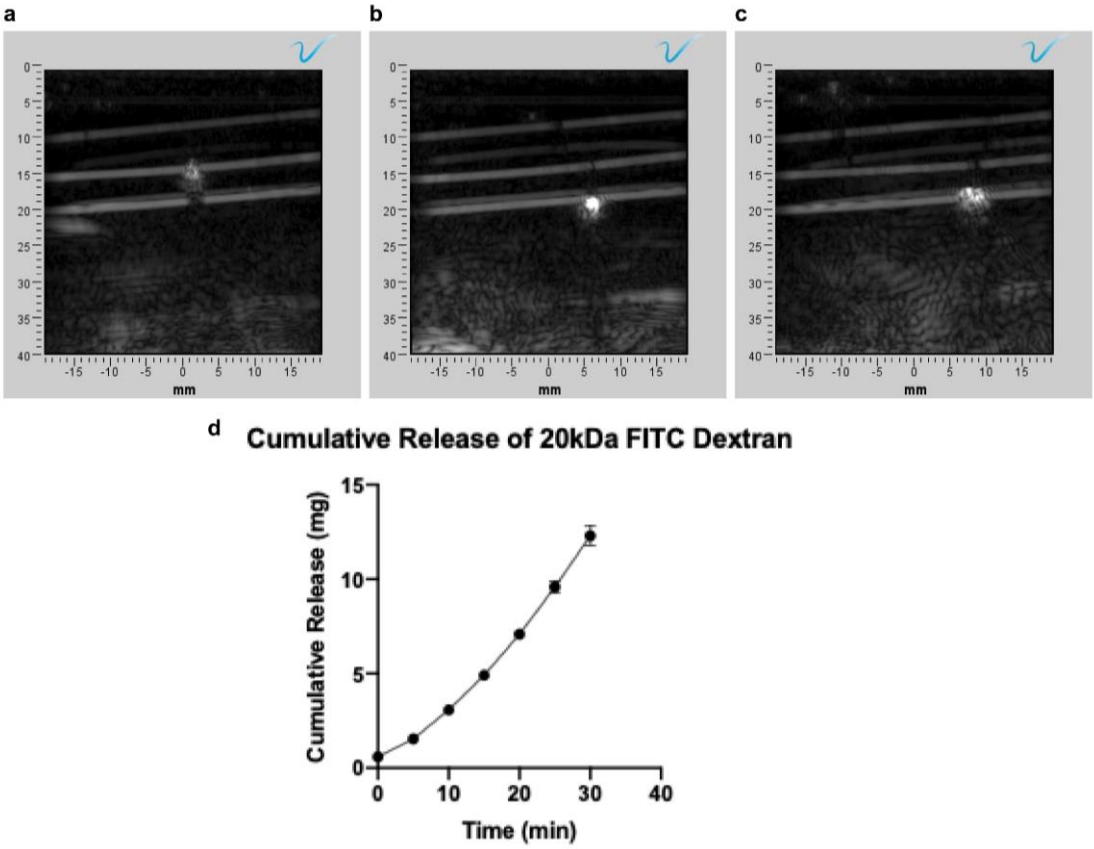

Figure 35: Integration of mock sensing motes with drug-loaded scaffold. a-c) Ultrasound images of individual mock motes embedded in a 3% agarose block, covered by a thin alginate scaffold. The mote in each image appears as a bright spot, while the top and bottom boundary of the scaffold appearing as a set of white horizontal lines. d) The cumulative amount of passive release measured from the scaffold during 30 minutes of applying the imaging ultrasound transducer.

To that end, we measured the cumulative release profiles of the scaffold while applying focused ultrasound at a 50 W intensity, using an *in vitro* setup that incorporated a 3x3 array of mock sensing motes (**Fig. 36a-c**). We tested the cumulative release of the scaffold on three separate days, with a scaffold that was 7 days post-fabrication, 10 days post fabrication, and 14 days post-fabrication respectively (**Fig. 36d-f**). The FUS burst applications stimulated a higher release rate of model drug for 50 minutes, compared to release rates from applying the imaging

transducer or passive release. A rapid increase in the release rate occurred from the scaffold after 50 minutes of applying the imaging transducer. While the imaging transducer applies two orders of magnitude lower peak pressure than the FUS transducer, cumulative exposure to the imaging transducer can stimulate breakdown of the scaffold structure. A visual assessment of the scaffold after sampling confirmed this, as all samples exposed to ultrasound exhibited holes at and near the focal area, which did not occur on the control samples.

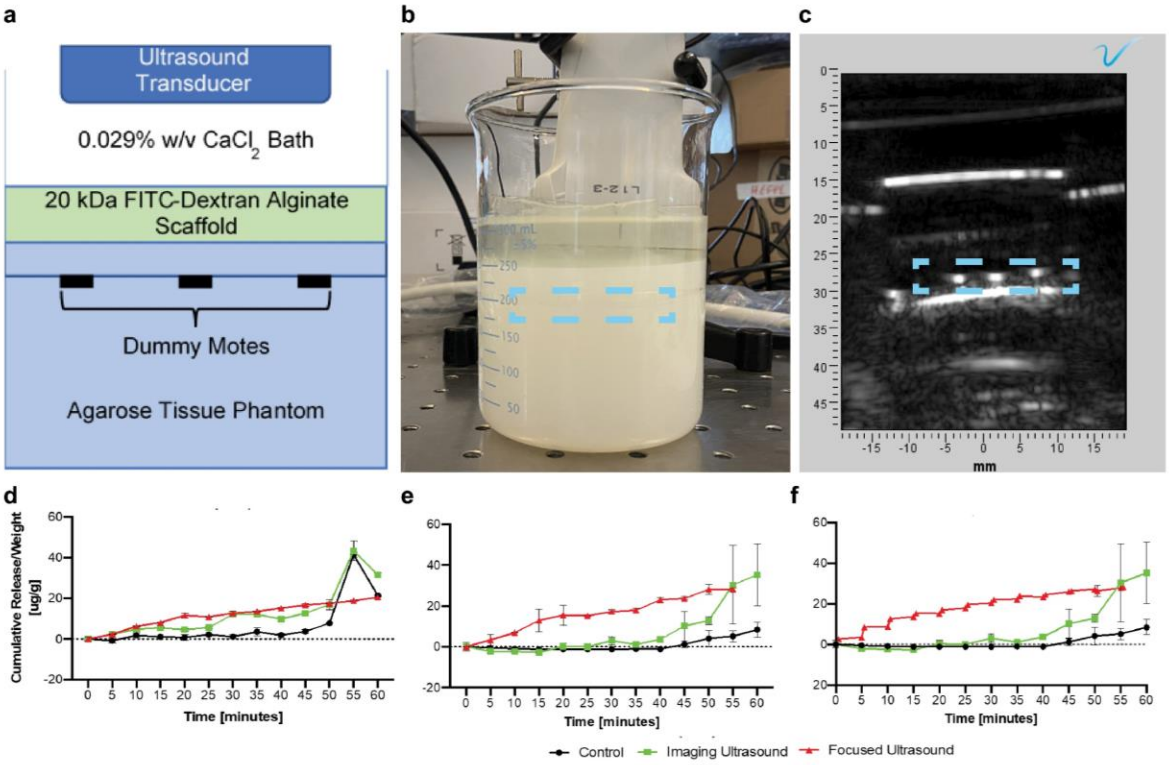

Figure 36: Model drug released during *in vitro* testing. a) Schematic of *in vitro* testing setup. b) Photograph of testing setup. c) Ultrasound image of multiple mock mote sin alignment, highlighted within the dotted blue box. d-f) Release profiles of FITC-dextran 20k Da from the scaffold, when undergoing focused ultrasound (red), imaging ultrasound (green), and no ultrasound (black). The scaffold was 7 days post-fabrication (d, n =1), 10 days post fabrication e, n = 3), and 14 days post-fabrication (f, n =3), respectively. Release was measured as the amount of fluorescent compound detected in collected samples of surrounding solution, normalized by the total weight of the scaffold sample.

4.3.1.c. Capacities of flexible focused ultrasound transducer

To assess the effect of the peak negative pressure of the flexible 16x16 focused ultrasound array, we performed a similar assessment of the cumulative release profile of the scaffold during three cycles of applied FUS. We applied 30 s of FUS for each cycle at the 6-, 12-, and 18-minute time points, and collected samples at the 0- and 23-minute points, along with before and after each FUS application. The application of the single element FUS transducer induced a significantly larger cumulative release than that induced by the flexible array, and both transducers triggered significantly increased release compared to the passive background leaching from the control samples (**Fig. 37**). Nevertheless, the background release levels have prompted additional reformulation of the scaffold, which is a continuing area of work.

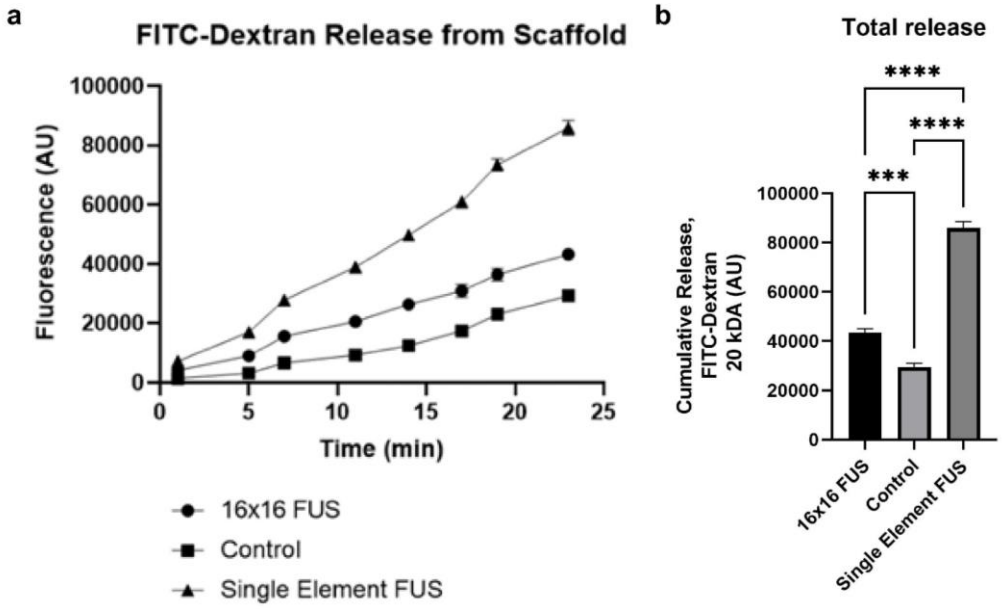

Figure 37: Effect of flexible 16x16 array on scaffold. A. Release profile of FITC-dextran 20k Da from the scaffold samples, which undergoes three bursts of ultrasound, at the 6-, 12-, and 18-minute time points. Release is shown in arbitrary units (AU). B. Cumulative release of FITC-dextran 20k Da from the scaffolds. ***P < 0.0004, ****P < 0.0001 (n = 3)

4.3.2. *In vitro* testing of integrated elements

4.3.2.a. Cell monolayer

We applied focused ultrasound to a cell monolayer, within an *in vitro* setup that aligned either a drug-loaded scaffold or 24 drug-loaded microcapsules between the ultrasound transducer and the monolayer. When testing with the scaffold, we manually aligned the scaffold and monolayer within the FUS focal area; when testing with microcapsules, we placed a custom-molded agarose layer atop the monolayer, which had a small hole in the center into which we

pipetted the sample microcapsules, thereby ensuring that placement of the microcapsules aligned with the FUS focal area (**Fig 38a**). By ensuring consistent alignment, we minimized inconsistency of applied FUS pressure experienced by samples across various runs. Furthermore, by positioning the FUS test setup on the inverted microscope stage, we collected real-time fluorescent images as the scaffold and microcapsules underwent FUS (**Fig 38b**). The scaffold had no noticeably visible change (**Fig 38c-d)**, while the microcapsules did noticeably move during FUS pulses (**Fig 38e-f)**. It was not possible to visibly detect fluorescent release in real-time because of the relatively intense brightness of the drug-loaded samples compared to the amount dispersed into the surrounding solution.

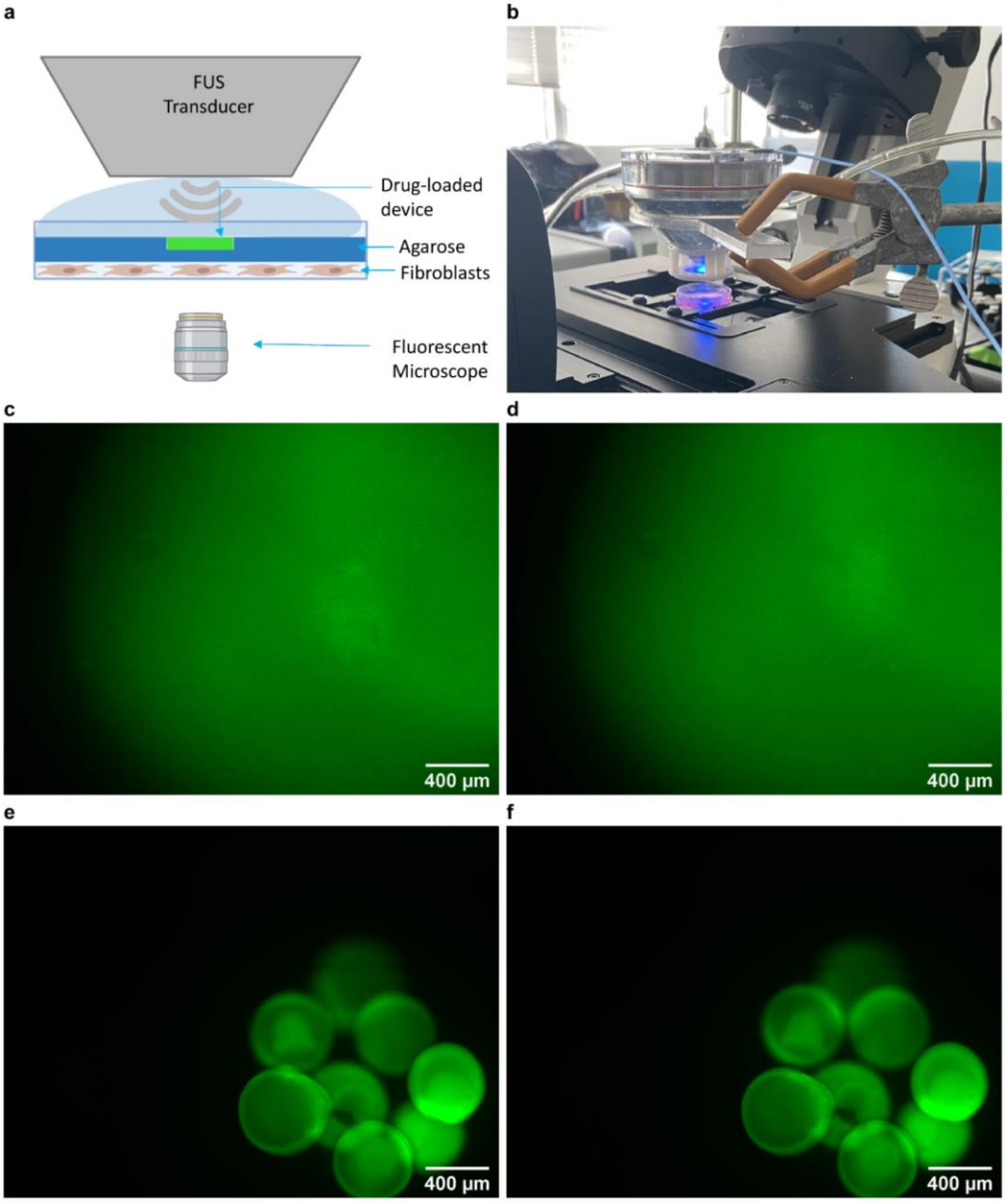

Figure 38: Testing of drug-loaded devices with cell monolayer. Monolayer testing setup schematic (a) and photograph (b). Fluorescent microscope images of the scaffold, placed on top of the agarose-monolayer structure, at the beginning (c) and end (d) of a 30 s burst of pulsed FUS. Fluorescent microscope images of a sample of microcapsules pipetted on top of the cell monolayer, at the beginning (e) and end (f) of a 30 s burst of pulsed FUS.

Cell staining of tested monolayers showed minimal cell death under the focal area (**Fig. 39a, c, e**), and almost no cell death in the surrounding regions (**Fig. 39b, d, f**). Additionally, areas of cell detachment occurred under the FUS focal area, shown as black regions (**Fig. 39c, e**).

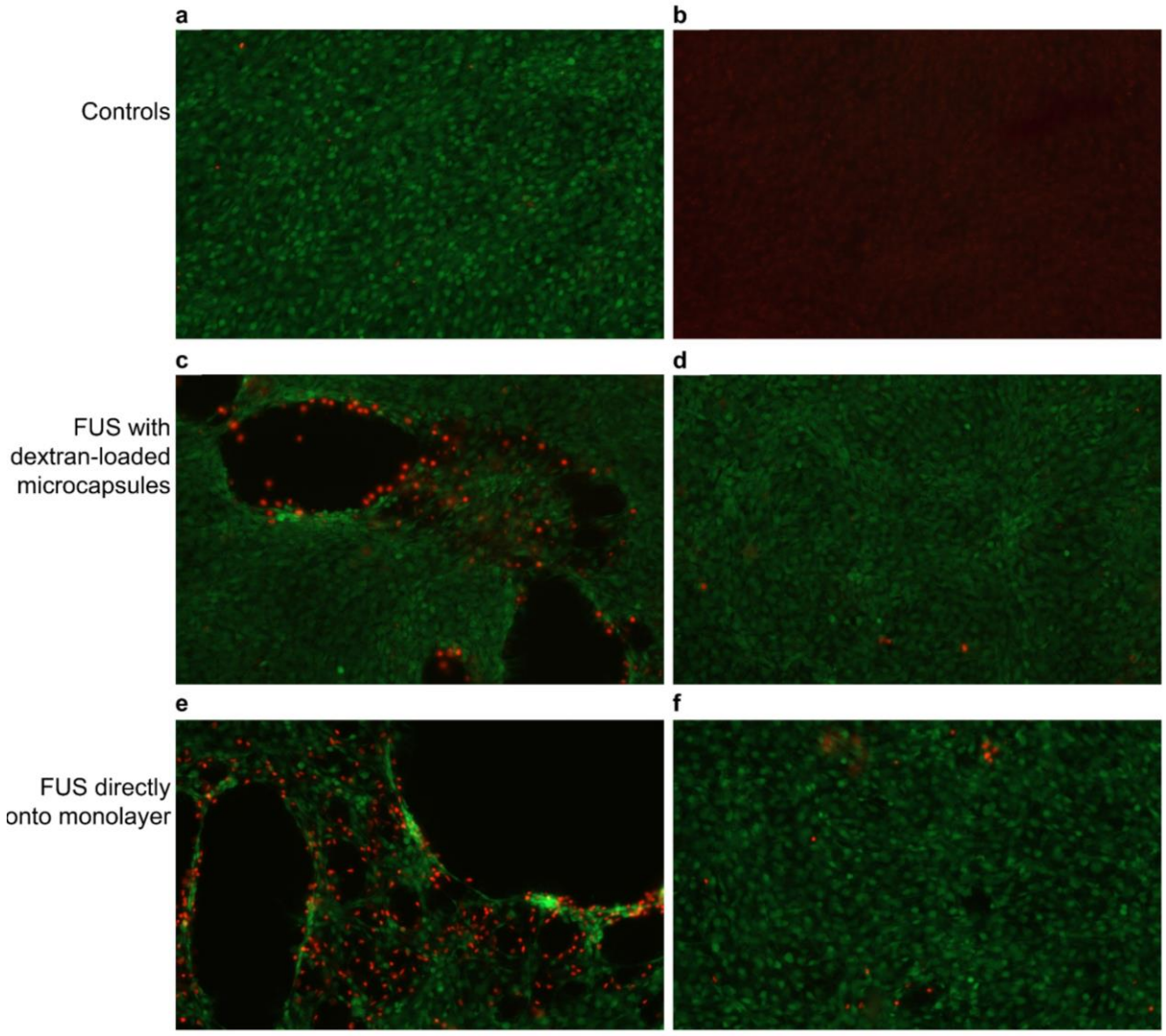

Figure 39: Effect of FUS on cell monolayer. a) Positive control, showing live cells (Calcein AM, green). b) Negative control of dead cells (Ethidium Homodimer-1, red). c-d) Imaging of the area of the hDF monolayer under the focal area (c) and in the surrounding region (d) after FUS applied to the dextran-PEGDA microcapsules. e-f) Imaging of the area of the hDF monolayer under the focal area (e) and in the surrounding region (f) after FUS applied directly to the monolayer.

4.3.2.b. Cell construct

To address this challenge of cell liftoff observed when testing the monolayer, and to have an *in vitro* model that more closely mimics human anatomy and physiology, we modified our *in vitro* model to include a 3-dimensional cell construct, rather than a monolayer. After testing seeding density, feeding strategy, and foundation material, we performed our FUS testing on constructs with a seeding concentration of 10,000 cell/construct, with a collagen foundation. The 10,000 cells/construct density had the smallest percentage of dead cell, most widespread cell distribution, and minimal contraction in the X-Y plane, compared to constructs at the other seeding densities (data not shown). Culturing occurred over 7 days in a collagen matrix.

On day 7, we performed the FUS testing on the constructs using a custom mounting piece to mimic the holder that we will be using for *in vivo* demonstrations (**Fig. 40**), which aligns the FUS transducer directly above the center of the construct sample. This alignment was important for consistently knowing where the peak negative pressure was applied to the sample, since this system was not integrated with imaging ultrasound. These constructs underwent 10 bursts of the 150 W FUS, applied for 30 s every minute, which is the upper limit of the amount of FUS pressure relevant for therapeutic applications. Furthermore, we maintained minimum changes in impedance between the FUS transducer's coupling cone and the sample by applying coupling gel at the interface.

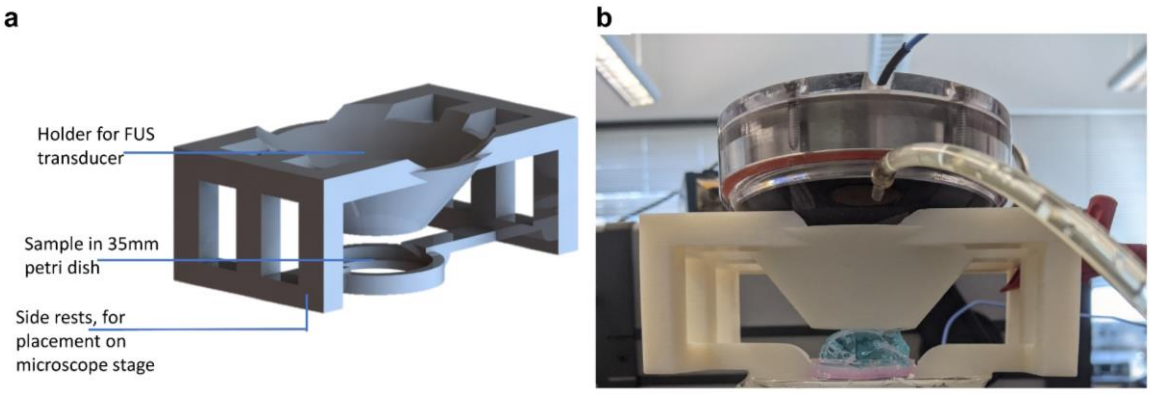

Figure 40: Testing setup for applying FUS to cell construct. a) Schematic of mounting piece, designed to align FUS transducer with the 35 mm petri dish. b) Photograph of testing setup.

The primary readout from this experiment was observing whether the FUS applications affected occurrences of cell death within the constructs. As a baseline, we observed some small amount of cell death localized to the surface and edges of the positive control constructs (**Fig. 41a**), and complete death in the negative control (**Fig. 41b**). Constructs which underwent the 150 W FUS applications did not display any noticeable difference in live and dead staining, compared to the control constructs (**Fig. 41c-d**). Live imaging on day 11 confirmed that the constructs which underwent FUS applications continued to display similar trends of cell death as the positive control, namely that the cell death was localized to the surface and edges (**Fig. 41e**). The lack of change in the construct demonstrates that these FUS parameters are within an appropriate range for *in vivo* applications.

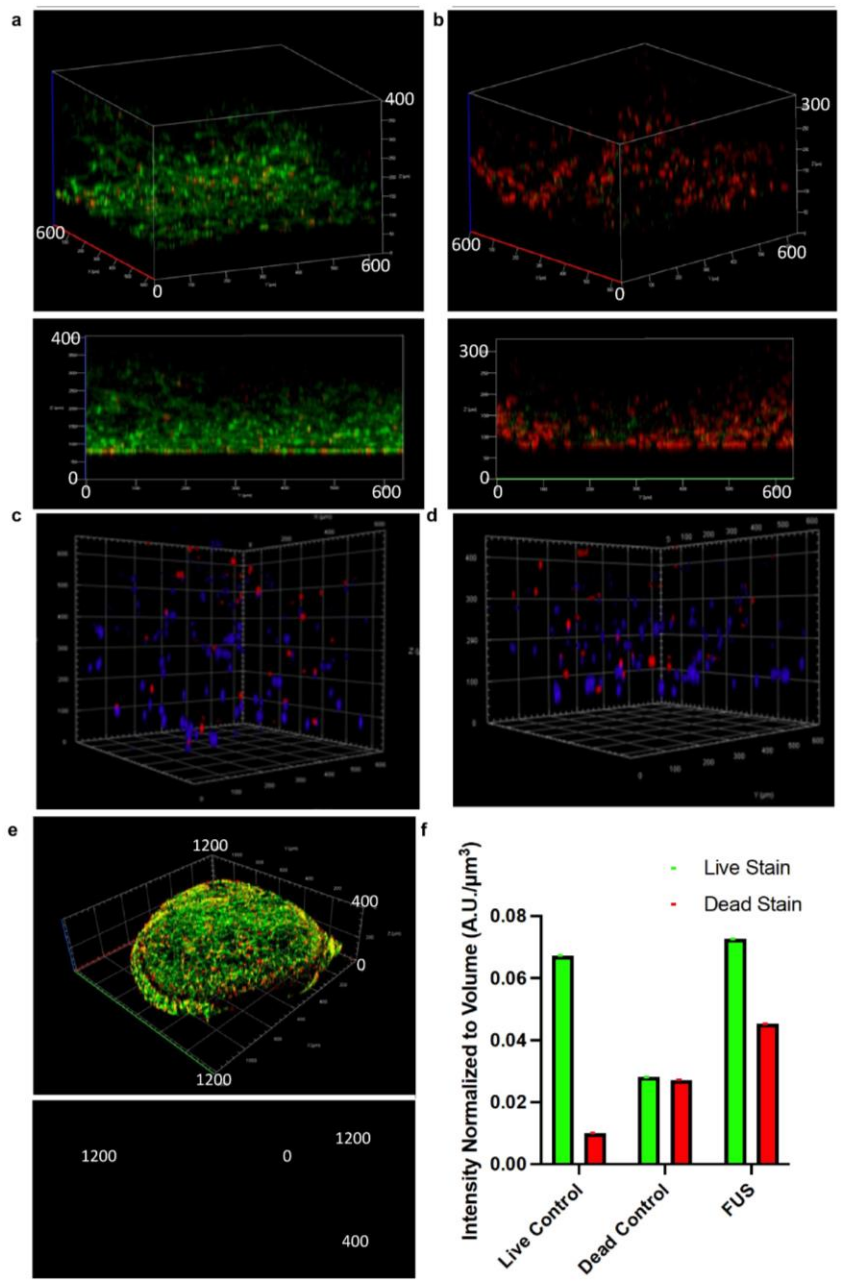

Figure 41: Cell construct structure. a) Live control of the construct at day 11, showing predominantly live cells (Calcein AM, green) a few dead cells along the surface and edges (Ethidium Homodimer-1, red). b) Dead control at day 11, with evenly distributed cell death throughout. c) Representative live (Hoechst, blue) and dead (Ethidium Homodimer-1, red) images of the hDF constructs at day 1 without FUS. d) Representative live and dead image of the hDF construct at day 1 having undergone FUS at 150 W. e) A construct at day 11, after undergoing FUS, with cell death localized to the surface and edges. f) Normalized intensity of live and dead staining on day 11 cell constructs.

4.3.3. Release effect from microcapsules into cell construct

4.3.3.a Fabrication of microcapsules loaded with relevant compounds

To demonstrate a cellular response to the compound release from the microcapsules, we loaded the microcapsules with lipopolysaccharide (LPS). LPS is a causative agent of the cellular production of nitric oxide (NO); if the microcapsules release sufficient LPS, we would detect increased NO levels in the construct.

Inlet port	***Composition***	***Flow rate (µL/min)***
Inner dispersed phase	3.75% dextran 450-650k Da + 1 mg LPS-FITC (2-10 µg FITC/mg of LPS)	(0.9 µL/min)
Outer dispersed phase	PEGDA 10k Da (20% w/v) + PEGDA 575 Da (30% v/v) + 2.5% Darocure 2959 (w/v)	(0.55 µL/min)
Continuous phase	Light mineral oil + 3% Span 80 (v/v)	(12 µL/min)

Table 17: Microfluidic parameters for LPS-loaded microcapsules.

To fabricate these modified microcapsules, we adjusted the inlet phase solutions and flow rates for on-chip fabrication (**Table 17**), while continuing to use the same PDMS chip design as discussed in **Section 2.3.3**. In particular, we increased the PEGDA phase flow rate by 0.05 µL/min to maintain consistent droplet formation; for comparison, the slightly slower flow rate used previously resulted in plug structures when respective to these altered compositions, rather than the desired droplets. At these adjusted flow rates, we successfully fabricated microcapsules similar in structural appearance to the previously demonstrated compositions (**Fig. 42a**); these

LPS-loaded microcapsules also appeared stable when stored for 10 days (**Fig. 42c**), as we expected based on the prior results. We used FITC-conjugated LPS to confirm whether the FITC-LPS stays concentrated in the dextran phase; after fabrication, the microcapsules did have the FITC concentrated in the dextran region (**Fig. 42b**). However, the FITC-LPS appeared to migrate into the PEGDA phase during 10 days of storage in DI water (**Fig. 42d**). Given that we did not observe such a phenomenon when loading the microcapsules with FITC-dextran, additional research may be required to understand this change, such as an impact from the MW or charge of the FITC-LPS which is sufficiently different from that of FITC-dextran as to induce this migration between phases. Given that the microcapsules will be suspended in PBS for delivery to the wound site during the *in vivo* demonstration, we also stored the LPS-loaded beads in PBS for 6 days to observe whether there were any structure effects. In contrast to the results from stored the LPS-loaded microcapsules in DI water, there was minimal visible degradation on brightfield (**Fig. 42e**) or change in fluorescence distribution **(Fig. 42f**) after this period in PBS. Thus, the stability of the LPS-loaded microcapsules in PBS was promising with respect to the eventual *in vivo* application.

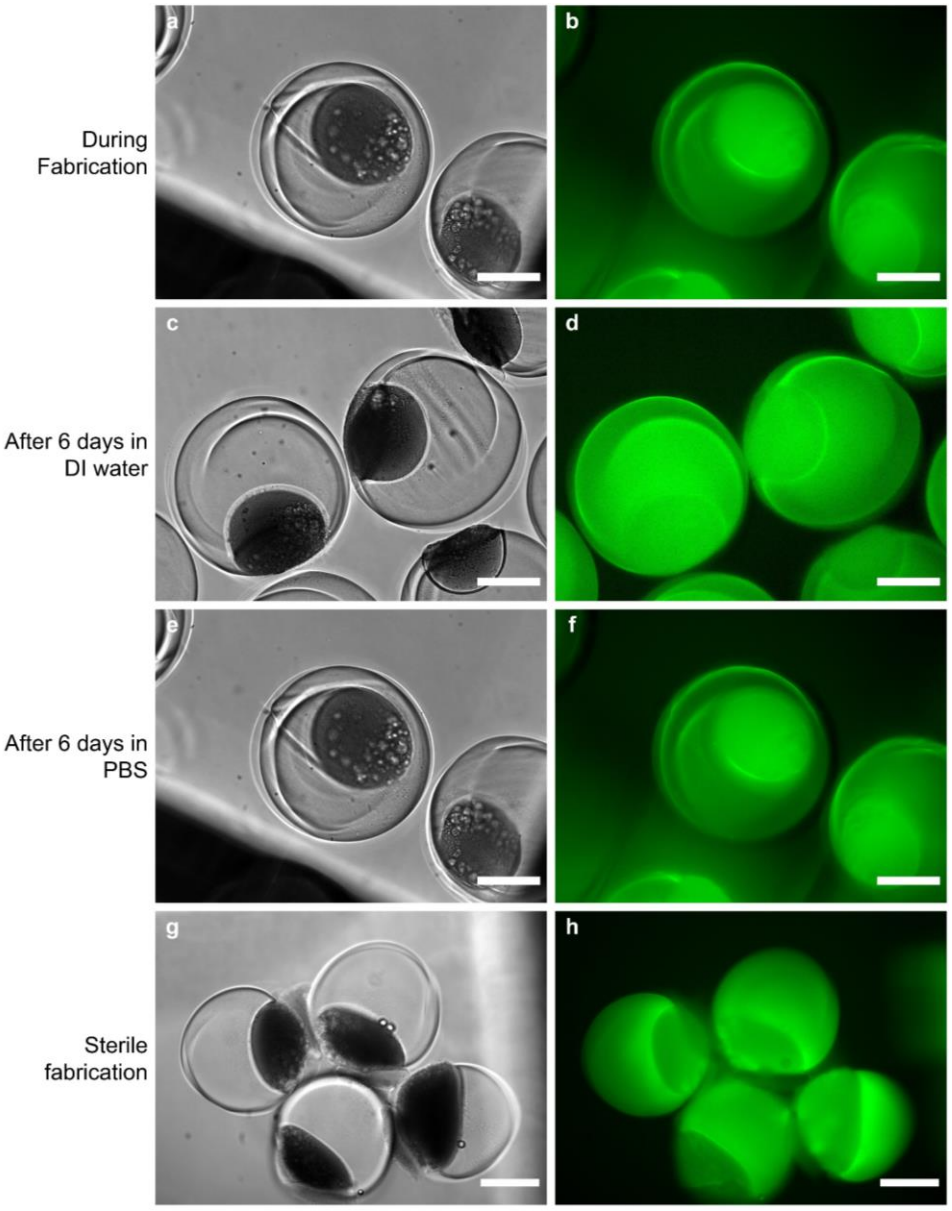

Figure 42: LPS-loaded dextran-PEGDA microcapsules a-b) The LPS-loaded microcapsules immediately after fabrication and washing. c-d) The same sample of microcapsules after 6 days of soaking in DI water. e-f) The LPS-loaded microcapsule sample after 6 days of soaking in PBS. g-h) Representative LPS-loaded microcapsules fabricated in sterile technique. Scale bars are 200 µm.

4.3.3.b Sterile fabrication of microcapsules

After refabricating these LPS-loaded microcapsules in a sterile environment, we observed that their ATPS ratio was shifted and that the particles had a Janus particle-like structure (**Fig. 42g-h**). This is likely because autoclaving the dextran and filtering the PEGDA prepolymer may have changed the concentrations of those respective solutions, and thus the ratio. Additionally, the distribution of the fluorescent compound differed from the non-sterile microcapsules, with the highest fluorescent intensity occurring on the inner surface of the PEGDA, bordering the dextran phase. We are conducting further research into this discrepancy that occurs due to the sterile fabrication process in our future works.

4.4 Discussion

Applying the three different types of transducers to the system components was instrumental in confirming certain functionalities and in identifying aspects for further development. Firstly, applying imaging-level ultrasound, at very low pressure and over a wide focal area, demonstrated that that the motes were visible via ultrasound even with the scaffold in place. However, it also demonstrated the high background release rate of the scaffold, which had visible damage after 50 minutes of exposure to the imaging transducer. Additionally, by applying the flexible array and the single element transducer to the scaffold, we demonstrated that the flexible array generates a higher cumulative compound release than the cumulative background release, although less than that from the single element transducer.

Next, we confirmed that there were minimal damaging effects for a cell monolayer or 3-dimensional construct when either directly exposed to focused ultrasound or exposed while underneath a sample of scaffold or microcapsules. Even when we increased the amount of FUS exposure to 10 cycles of FUS at 150 W, applied in rapid succession so as to induce some minor heating effect, there were only cell damage to the edges of the cell structures. With real-time fluorescent monitoring, we confirmed that the focal area was correctly positioned and that the drug-loaded devices were responding to the FUS. Therefore, these experiments confirm that the upper limit of potential FUS parameters for the *in vivo* stage will cause minimal tissue damage.

Finally, we demonstrated the loading versatility of the microcapsules, substituting LPS-FITC instead of FITC-dextran as the model drug. With the modified the composition, the microcapsules maintained their geometry and fluorescence arrangement, even after several days in solution. Furthermore, when exposed to ultrasound in the *in vitro* setup, the LPS-loaded microcapsules released an effective payload. However, we did note minor changes in the phase separation ratio when we refabricated the microcapsules in a sterile environment; further research into those changes is included for future work.

Overall, outcomes from this Aim provided an encouraging step towards the broader goal of a closed-loop system for healing interventions, primarily by demonstrating that the actuation devices can respond to ultrasound pulses which are safe for surrounding tissue. The process also highlights the numerous considerations needed for the integration of a multitude of devices within a localized area of the body. Furthermore, given the importance of the focal area for the *in*

vitro setup, particular effort will be committed during the *in vivo* experiments to ensure proper focal area alignment.

Chapter 5: Conclusion

In this thesis, we demonstrate the fabrication and actuation of devices for wireless, deep-tissue drug delivery, which couple with an external control modality to facilitate localized therapeutic interventions.

In Chapter 2, we discuss a microfluidic fabrication technique for fabricating hydrogel-based microcapsules. Our strategy relies on an aqueous two-phase system (ATPS), comprised of a dextran-PEGDA composition, which forms biphasic droplets without an intermediate oil layer so as to ensure biocompatibility. Furthermore, we demonstrate an on-chip photopolymerization system which results in monodisperse microcapsules. Although similar ATPS on-chip fabrication strategies have been demonstrated previously, we determine a specific composition of high molecular weight dextran and mixed molecular weight PEGDA which, at certain flow rates, resulted in an asymmetric biphasic microcapsule; the inner dextran-rich phase is loaded with a high concentration of model drug and the outer PEGDA-rich phase is largely impenetrable to the payload. While we tune and characterize these microcapsules using dextran 20k Da as a model drug, these microcapsules are versatile and can be modified for a variety of payloads at similar molecular weights.

In Chapter 3, we demonstrate the effect of applying focused ultrasound on the microcapsules, for a repeatable and on-demand drug release. Ultrasound-triggered drug delivery from micro- and nano-scale drug delivery systems are of particular interest due to the strategy's

noninvasiveness and large depth of penetration, even when compared to other external triggering modalities, such as magnetic or infrared techniques. We demonstrate that the microcapsules largely undergo inertial cavitation, with minimal heating effects, due to the pulsed FUS; this inertial cavitation caused structural disruption, particularly in the dextran-rich phase, which resulted in rapid drug release during FUS applications. In tuning the FUS parameters, we demonstrate that the applied FUS intensity is the primary parameter in determining release profiles, with FUS bursts above 100 W corresponding to a significant increase in drug release; above that threshold intensity, the number of FUS bursts and lengths of the respective bursts determines the magnitude of total drug release. This ultrasound-triggered method of drug delivery is innovative because prior micro-scale ultrasound-assisted drug delivery technologies have incorporated microbubbles or contrast agents, which acts as 'preseeding' to ensure cavitation. However, these strategies are inherently limited in their use period within the body, typically on the scale of minutes or sometimes hours, and have only a single burst release. In contrast, by not incorporating these preseeding elements, our microcapsules were able to repeatedly release an on-demand dose over the course of several days. Therefore, this technology may facilitate localized and on-demand drug delivery for applications that require repeated dosing.

Finally, in Chapter 4, we demonstrate the functionality of drug-loaded actuators, both the microcapsules and a scaffold, using multiple *in vitro* test setups; these actuators, along with a flexible ultrasound array, implantable sensing motes, and adaptive learning algorithms, will comprise a closed-loop system for responsively promoting healing within a wound. We

demonstrate that when we integrate the actuators and sensors, each element is independently visible in ultrasound images. The actuators maintain the expected release profile when integrated with the sensors. When tested with *in vitro* cell constructs, the actuators are FUS-responsive at low enough FUS intensity as to not damage the cell constructs. Furthermore, we load the microcapsules with LPS, and observe potential changes in the cell constructs corresponding to the presence of the released LPS. These demonstrations will guide the testing strategy and material refinement for continued integration of the of the sensors, actuators, and control algorithm, towards the eventual goal of a closed-loop system.

5.1 Future Directions

While the immediate next step of this work is an *in vivo* demonstration of the ultrasound-triggered microcapsules and scaffold, there remain several areas for further research.

First, there remains further research to consider with respect to the fundamental properties driving the asymmetric geometry of the microcapsules. While we were able to shift the contact angle between the dextran and PEGDA phases, we did not demonstrate complete encapsulation of the dextran-rich phase within the PEGDA-rich phase. While there has been much research about dextran-PEGDA solution in bulk, the behavior of the ATPS on a microfluidic chip is not fully explored, and merits further analysis.

We also intend to further refine the ultrasound-triggering of microcapsules to demonstrate multiplexed release. Already we have shown that the microcapsule composition can be modified for loading compounds close to 20k Da in weight, and we plan to further investigate the possibilities for payload which have differing molecular weights or charges. These compounds may have different release profiles from the microcapsules, or the PEGDA composition may need minor adjustments to allow for differing release profiles for each type of compound. By tuning these material properties, we intend to be able to selectively trigger release of microcapsules loaded with a particular compound, within an area injected with microcapsules loaded with a disparate variety of compounds. We envision that the ability to discretely deliver a multitude of compounds on-demand and within a localized area may have applications for current therapies, such as for tumor microenvironments, and may enable the effectiveness of new therapeutic strategies.

Furthermore, as implied in Appendix A, we believe that the insights from this research may contribute towards strategies for medical microrobots. While the demonstrated actuators remain at the injection site, the principles of ultrasound-responsiveness, biocompatibility, and functionality can translate to an eventual mobile iteration.

References

[1] J. E. Aldrich, "Basic physics of ultrasound imaging," (in eng), *Crit Care Med,* vol. 35, no. 5 Suppl, pp. S131-7, May 2007.

[2] F. A. Duck, "Medical and non-medical protection standards for ultrasound and infrasound," *Progress in Biophysics and Molecular Biology,* vol. 93, no. 1, pp. 176-191, 2007/01/01/ 2007.

[3] M. S. Canney, M. R. Bailey, L. A. Crum, V. A. Khokhlova, and O. A. Sapozhnikov, "Acoustic characterization of high intensity focused ultrasound fields: a combined measurement and modeling approach," (in eng), *J Acoust Soc Am,* vol. 124, no. 4, pp. 2406-20, Oct 2008.

[4] H. Yuk, B. Lu, and X. Zhao, "Hydrogel bioelectronics," (in en), *Chemical Society Reviews,* vol. 48, no. 6, pp. 1642-1667, 2019 2019.

[5] R. Feiner and T. Dvir, "Tissue–electronics interfaces: From implantable devices to engineered tissues," *Nature Reviews Materials,* vol. 3, no. 1, p. 17076, 2018.

[6] K. C. Spencer, J. C. Sy, K. B. Ramadi, A. M. Graybiel, R. Langer, and M. J. Cima, "Characterization of Mechanically Matched Hydrogel Coatings to Improve the Biocompatibility of Neural Implants," (in En), *Scientific Reports,* vol. 7, no. 1, p. 1952, 2017/05/16/ 2017.

[7] A. A. Sharkawy, B. Klitzman, G. A. Truskey, and W. M. Reichert, "Engineering the tissue which encapsulates subcutaneous implants. I. Diffusion properties," (in en), *Journal of Biomedical Materials Research,* vol. 37, no. 3, pp. 401-412, 1997 1997.

[8] W. K. Ward, E. P. Slobodzian, K. L. Tiekotter, and M. D. Wood, "The effect of microgeometry, implant thickness and polyurethane chemistry on the foreign body response to subcutaneous implants," *Biomaterials,* vol. 23, no. 21, pp. 4185-4192, 2002/11/01/ 2002.

[9] E. R. Aurand, K. J. Lampe, and K. B. Bjugstad, "Defining and Designing Polymers and Hydrogels for Neural Tissue Engineering," *Neuroscience research,* vol. 72, no. 3, pp. 199-213, 2012/03// 2012.

[10] J. L. Ifkovits, J. J. Devlin, G. Eng, T. P. Martens, G. Vunjak-Novakovic, and J. A. Burdick, "Biodegradable fibrous scaffolds with tunable properties formed from photo-cross-linkable poly (glycerol sebacate)," *ACS applied materials & interfaces,* vol. 1, no. 9, pp. 1878-1886, 2009.

[11] J. Kim, M. Dadsetan, S. Ameenuddin, A. J. Windebank, M. J. Yaszemski, and L. Lu, "In vivo biodegradation and biocompatibility of PEG/sebacic acid-based hydrogels using a cage implant system," *Journal of biomedical materials research Part A,* vol. 95, no. 1, pp. 191-197, 2010.

[12] N. Remoué, C. Bonod, B. Fromy, and D. Sigaudo-Roussel, "Animal models in chronic wound healing research: for innovations and emerging technologies in wound care," in *Innovations and Emerging Technologies in Wound Care*: Elsevier, 2020, pp. 197-224.

[13] R. D. Field, P. N. Anandakumaran, and S. K. Sia, "Soft medical microrobots: Design components and system integration," *Applied Physics Reviews,* vol. 6, no. 4, p. 041305, 2019.

[14] K. Wang, N. G. Horton, K. Charan, and C. Xu, "Advanced fiber soliton sources for nonlinear deep tissue imaging in biophotonics," *IEEE Journal of Selected Topics in Quantum Electronics,* vol. 20, no. 2, pp. 50-60, 2013.

[15] M. Aliabouzar, G. L. Zhang, and K. Sarkar, "Acoustic and mechanical characterization of 3D-printed scaffolds for tissue engineering applications," *Biomedical Materials,* vol. 13, no. 5, p. 055013, 2018.

[16] O. Veiseh *et al.*, "Size- and shape-dependent foreign body immune response to materials implanted in rodents and non-human primates," (in eng), *Nature Materials,* vol. 14, no. 6, pp. 643-651, 2015/06// 2015.

[17] G. ter Haar, "Therapeutic ultrasound," (in eng), *Eur J Ultrasound,* vol. 9, no. 1, pp. 3-9, Mar 1999.

[18] H. Jia *et al.*, "Universal Soft Robotic Microgripper," *Small,* vol. 15, no. 4, p. 1803870, 2019.

[19] K. Köhrmann, M. Michel, A. Steidler, E. Marlinghaus, O. Kraut, and P. Alken, "Technical characterization of an ultrasound source for noninvasive thermoablation by high-intensity focused ultrasound," *BJU international,* vol. 90, no. 3, pp. 248-252, 2002.

[20] G. M. Cruise, D. S. Scharp, and J. A. Hubbell, "Characterization of permeability and network structure of interfacially photopolymerized poly (ethylene glycol) diacrylate hydrogels," *Biomaterials,* vol. 19, no. 14, pp. 1287-1294, 1998.

[21] R. Weissleder, "A clearer vision for in vivo imaging," (in eng), *Nature Biotechnology,* vol. 19, no. 4, pp. 316-317, 2001/04// 2001.

[22] G. York and Y. Kim, "Ultrasound Processing and Computing: Review and Future Directions," *Annual Review of Biomedical Engineering,* vol. 1, no. 1, pp. 559-588, 1999.

[23] Y. Zhou and X. Wang, "Effect of pulse duration and pulse repetition frequency of cavitation histotripsy on erosion at the surface of soft material," (in eng), *Ultrasonics,* vol. 84, pp. 296-309, Mar 2018.

[24] W. Yang and Y. Zhou, "Effect of pulse repetition frequency of high-intensity focused ultrasound on in vitro thrombolysis," (in eng), *Ultrason Sonochem,* vol. 35, no. Pt A, pp. 152-160, Mar 2017.

[25] U. Walter, M. Kanowski, J. Kaufmann, A. Grossmann, R. Benecke, and L. Niehaus, "Contemporary ultrasound systems allow high-resolution transcranial imaging of small echogenic deep intracranial structures similarly as MRI: a phantom study," *Neuroimage,* vol. 40, no. 2, pp. 551-558, 2008.

[26] M. Jang, H. Ruan, B. Judkewitz, and C. Yang, "Model for estimating the penetration depth limit of the time-reversed ultrasonically encoded optical focusing technique," *Optics express,* vol. 22, no. 5, pp. 5787-5807, 2014.

[27] J. A. Virmont, "NIR medical imaging: spatial resolution and discrimination," in *Optical Tomography, Photon Migration, and Spectroscopy of Tissue and Model Media: Theory, Human Studies, and Instrumentation*, 1995, vol. 2389, pp. 358-365: International Society for Optics and Photonics.

[28] T. Xu, W. Gao, L. P. Xu, X. Zhang, and S. Wang, "Fuel-free synthetic micro-/nanomachines," *Advanced Materials*, vol. 29, no. 9, p. 1603250, 2017.

[29] Z. Izadifar, P. Babyn, and D. Chapman, "Mechanical and biological effects of ultrasound: A review of present knowledge," *Ultrasound in medicine & biology*, vol. 43, no. 6, pp. 1085-1104, 2017.

[30] K. Malachowski *et al.*, "Stimuli-Responsive Theragrippers for Chemomechanical Controlled Release," *Angewandte Chemie (International ed. in English)*, vol. 53, no. 31, pp. 8045-8049, 2014/07/28/ 2014.

[31] A. Raza, U. Hayat, T. Rasheed, M. Bilal, and H. M. N. Iqbal, "“Smart” materials-based near-infrared light-responsive drug delivery systems for cancer treatment: A review," *Journal of Materials Research and Technology*, 2018/08/01/ 2018.

[32] S. Y. Chin *et al.*, "Additive manufacturing of hydrogel-based materials for next-generation implantable medical devices," *Science Robotics*, vol. 2, no. 2, p. eaah6451, 2017.

[33] M. P. Kummer, J. J. Abbott, B. E. Kratochvil, R. Borer, A. Sengul, and B. J. Nelson, "OctoMag: An electromagnetic system for 5-DOF wireless micromanipulation," *IEEE Transactions on Robotics*, vol. 26, no. 6, pp. 1006-1017, 2010.

[34] S. Martel, "Combining pulsed and DC gradients in a clinical MRI-based microrobotic platform to guide therapeutic magnetic agents in the vascular network," *International Journal of Advanced Robotic Systems,* vol. 10, no. 1, p. 30, 2013.

[35] W. Wang, L. A. Castro, M. Hoyos, and T. E. Mallouk, "Autonomous motion of metallic microrods propelled by ultrasound," *ACS nano,* vol. 6, no. 7, pp. 6122-6132, 2012.

[36] V. Garcia-Gradilla *et al.*, "Functionalized ultrasound-propelled magnetically guided nanomotors: Toward practical biomedical applications," *ACS nano,* vol. 7, no. 10, pp. 9232-9240, 2013.

[37] O. Ordeig, S. Y. Chin, S. Kim, P. V. Chitnis, and S. K. Sia, "An implantable compound-releasing capsule triggered on demand by ultrasound," *Scientific Reports,* Article vol. 6, p. 22803, 03/11/online 2016.

[38] M. N. Hoff *et al.*, "Safety Considerations of 7-T MRI in Clinical Practice," *Radiology,* p. 182742, 2019.

[39] K. J. Rao, F. Li, L. Meng, H. Zheng, F. Cai, and W. Wang, "A Force to Be Reckoned With: A Review of Synthetic Microswimmers Powered by Ultrasound," *Small,* vol. 11, no. 24, pp. 2836-2846, 2015.

[40] A. Sánchez, V. Magdanz, O. G. Schmidt, and S. Misra, "Magnetic control of self-propelled microjets under ultrasound image guidance," in *5th IEEE RAS/EMBS International Conference on Biomedical Robotics and Biomechatronics*, 2014, pp. 169-174: IEEE.

[41] B. P. Timko and D. S. Kohane, "Prospects for near-infrared technology in remotely-triggered drug delivery," *Expert opinion on drug delivery,* vol. 11, no. 11, pp. 1681-1685, 2014/11// 2014.

[42] R. Langer, "New methods of drug delivery," *Science,* vol. 249, no. 4976, pp. 1527-1533, 1990.

[43] R. Langer, "Drug delivery and targeting," *Nature,* vol. 392, no. 6679 Suppl, pp. 5-10, 1998.

[44] T. M. Allen and P. R. Cullis, "Drug delivery systems: entering the mainstream," *Science,* vol. 303, no. 5665, pp. 1818-1822, 2004.

[45] A. M. Vargason, A. C. Anselmo, and S. Mitragotri, "The evolution of commercial drug delivery technologies," *Nature Biomedical Engineering,* pp. 1-17, 2021.

[46] N. Bhattarai, J. Gunn, and M. Zhang, "Chitosan-based hydrogels for controlled, localized drug delivery," *Advanced drug delivery reviews,* vol. 62, no. 1, pp. 83-99, 2010.

[47] M. Khanday, A. Rafiq, and K. Nazir, "Mathematical models for drug diffusion through the compartments of blood and tissue medium," *Alexandria Journal of Medicine,* vol. 53, no. 3, pp. 245-249, 2017.

[48] S. Campbell and N. Smeets, "Drug Delivery: Polymers in the Development of Controlled Release Systems," in *Functional Polymers*, M. A. Jafar Mazumder, H. Sheardown, and A. Al-Ahmed, Eds. Cham: Springer International Publishing, 2019, pp. 1-29.

[49] K. Park, "Controlled drug delivery systems: past forward and future back," *Journal of Controlled Release,* vol. 190, pp. 3-8, 2014.

[50] Y. Yun, B. K. Lee, and K. Park, "Controlled drug delivery systems: the next 30 years," *Frontiers of Chemical Science and Engineering,* vol. 8, no. 3, pp. 276-279, 2014.

[51] H. Wen and K. Park, *Oral controlled release formulation design and drug delivery: theory to practice*. John Wiley & Sons, 2011.

[52] K. Park, "Facing the truth about nanotechnology in drug delivery," *ACS nano,* vol. 7, no. 9, pp. 7442-7447, 2013.

[53] S. M. Mirvakili and R. Langer, "Wireless on-demand drug delivery," *Nature Electronics,* vol. 4, no. 7, pp. 464-477, 2021.

[54] M. Sitti, *Mobile Microrobotics*. MIT Press, 2017.

[55] R. Bashir, "BioMEMS: state-of-the-art in detection, opportunities and prospects," *Advanced drug delivery reviews,* vol. 56, no. 11, pp. 1565-1586, 2004.

[56] H. Xie *et al.*, "Reconfigurable magnetic microrobot swarm: Multimode transformation, locomotion, and manipulation," *Science Robotics,* vol. 4, no. 28, p. eaav8006, 2019.

[57] I. B. Almeida *et al.*, "Smart Dressings for Wound Healing: A Review," *Advances in Skin & Wound Care,* vol. 34, no. 2, pp. 1-8, 2021.

[58] T. Boissenot, A. Bordat, E. Fattal, and N. Tsapis, "Ultrasound-triggered drug delivery for cancer treatment using drug delivery systems: from theoretical considerations to practical applications," *Journal of Controlled Release,* vol. 241, pp. 144-163, 2016.

[59] S. Talebian *et al.*, "Biopolymers for antitumor implantable drug delivery systems: recent advances and future outlook," *Advanced Materials,* vol. 30, no. 31, p. 1706665, 2018.

[60] B. J. Nelson, I. K. Kaliakatsos, and J. J. Abbott, "Microrobots for minimally invasive medicine," *Annual review of biomedical engineering,* vol. 12, pp. 55-85, 2010.

[61] C. Hu, S. Pané, and B. J. Nelson, "Soft micro-and nanorobotics," *Annual Review of Control, Robotics, and Autonomous Systems,* vol. 1, pp. 53-75, 2018.

[62] S. Sershen and J. West, "Implantable, polymeric systems for modulated drug delivery," *Advanced drug delivery reviews,* vol. 54, no. 9, pp. 1225-1235, 2002.

[63] J. K. Patra *et al.*, "Nano based drug delivery systems: recent developments and future prospects," *Journal of nanobiotechnology,* vol. 16, no. 1, pp. 1-33, 2018.

[64] Q. Liu *et al.*, "Self-Orienting Hydrogel Micro-Buckets as Novel Cell Carriers," *Angewandte Chemie International Edition,* vol. 58, no. 2, pp. 547-551, 2019.

[65] M. Lengyel, N. Kállai-Szabó, V. Antal, A. J. Laki, and I. Antal, "Microparticles, microspheres, and microcapsules for advanced drug delivery," *Scientia Pharmaceutica,* vol. 87, no. 3, p. 20, 2019.

[66] Y. K. Sung and S. W. Kim, "Recent advances in polymeric drug delivery systems," *Biomaterials Research,* vol. 24, no. 1, pp. 1-12, 2020.

[67] K. L. Thornton, "Principles of ultrasound," *The Journal of reproductive medicine,* vol. 37, no. 1, pp. 27-32, 1992.

[68] R. E. Apfel and C. K. Holland, "Gauging the likelihood of cavitation from short-pulse, low-duty cycle diagnostic ultrasound," *Ultrasound in medicine & biology,* vol. 17, no. 2, pp. 179-185, 1991.

[69] C. Coussios, C. Farny, G. Ter Haar, and R. Roy, "Role of acoustic cavitation in the delivery and monitoring of cancer treatment by high-intensity focused ultrasound (HIFU)," *International journal of hyperthermia,* vol. 23, no. 2, pp. 105-120, 2007.

[70] Z. Jagga and D. Gupta, "Machine learning for biomarker identification in cancer research–developments toward its clinical application," *Personalized medicine,* vol. 12, no. 4, pp. 371-387, 2015.

[71] A. L. Swan, A. Mobasheri, D. Allaway, S. Liddell, and J. Bacardit, "Application of machine learning to proteomics data: classification and biomarker identification in postgenomics biology," *Omics: a journal of integrative biology,* vol. 17, no. 12, pp. 595-610, 2013.

[72] L. J. Marcos-Zambrano *et al.*, "Applications of machine learning in human microbiome studies: a review on feature selection, biomarker identification, disease prediction and treatment," *Frontiers in microbiology,* vol. 12, p. 313, 2021.

[73] H. N. Yow and A. F. Routh, "Formation of liquid core–polymer shell microcapsules," *Soft matter,* vol. 2, no. 11, pp. 940-949, 2006.

[74] D. Lensen, K. van Breukelen, D. M. Vriezema, and J. C. van Hest, "Preparation of biodegradable liquid core PLLA microcapsules and hollow PLLA microcapsules using microfluidics," *Macromolecular bioscience,* vol. 10, no. 5, pp. 475-480, 2010.

[75] D. S. Kohane, "Microparticles and nanoparticles for drug delivery," (in eng), *Biotechnol Bioeng,* vol. 96, no. 2, pp. 203-9, Feb 1 2007.

[76] W. L. Lee, E. Widjaja, and S. C. Loo, "Designing drug-loaded multi-layered polymeric microparticles," (in eng), *J Mater Sci Mater Med,* vol. 23, no. 1, pp. 81-8, Jan 2012.

[77] L. Nan, Y. Cao, S. Yuan, and H. C. Shum, "Oil-mediated high-throughput generation and sorting of water-in-water droplets," *Microsystems & Nanoengineering,* vol. 6, no. 1, pp. 1-10, 2020.

[78] B.-U. Moon, N. Abbasi, S. G. Jones, D. K. Hwang, and S. S. Tsai, "Water-in-water droplets by passive microfluidic flow focusing," *Analytical chemistry,* vol. 88, no. 7, pp. 3982-3989, 2016.

[79] P. Zhu and L. Wang, "Passive and active droplet generation with microfluidics: a review," *Lab on a Chip,* vol. 17, no. 1, pp. 34-75, 2017.

[80] A. Montessori *et al.*, "Regularized lattice Boltzmann multicomponent models for low capillary and Reynolds microfluidics flows," *Computers & Fluids,* vol. 167, pp. 33-39, 2018.

[81] J. R. Choi, K. W. Yong, J. Y. Choi, and A. C. Cowie, "Recent advances in photo-crosslinkable hydrogels for biomedical applications," *BioTechniques,* vol. 66, no. 1, pp. 40-53, 2019.

[82] V. Hagel, T. Haraszti, and H. Boehm, "Diffusion and interaction in PEG-DA hydrogels," *Biointerphases,* vol. 8, no. 1, p. 36, 2013.

[83] B. G. Bush, J. M. Shapiro, F. W. DelRio, R. F. Cook, and M. L. Oyen, "Mechanical measurements of heterogeneity and length scale effects in PEG-based hydrogels," *Soft Matter*, vol. 11, no. 36, pp. 7191-7200, 2015.

[84] B. V. Slaughter, S. S. Khurshid, O. Z. Fisher, A. Khademhosseini, and N. A. Peppas, "Hydrogels in regenerative medicine," *Advanced materials*, vol. 21, no. 32-33, pp. 3307-3329, 2009.

[85] S. P. Zustiak and J. B. Leach, "Hydrolytically degradable poly (ethylene glycol) hydrogel scaffolds with tunable degradation and mechanical properties," *Biomacromolecules*, vol. 11, no. 5, pp. 1348-1357, 2010.

[86] Y. K. Yau, C. W. Ooi, E.-P. Ng, J. C.-W. Lan, T. C. Ling, and P. L. Show, "Current applications of different type of aqueous two-phase systems," *Bioresources and Bioprocessing*, vol. 2, no. 1, pp. 1-13, 2015.

[87] T. Nakano and T. Nakaoki, "Coagulation size of freezable water in poly (vinyl alcohol) hydrogels formed by different freeze/thaw cycle periods," *Polymer journal*, vol. 43, no. 11, pp. 875-880, 2011.

[88] B. Y. Zaslavsky, *Aqueous two-phase partitioning: physical chemistry and bioanalytical applications*. CRC press, 1994.

[89] R. Hatti-Kaul, "Aqueous Two-Phase Systems: Methods and Protocols Methods and Protocols," ed: Springer, 2001.

[90] A. G. Teixeira, R. Agarwal, K. R. Ko, J. Grant-Burt, B. M. Leung, and J. P. Frampton, "Emerging biotechnology applications of aqueous two-phase systems," *Advanced healthcare materials,* vol. 7, no. 6, p. 1701036, 2018.

[91] G. T. Vladisavljević, R. Al Nuumani, and S. A. Nabavi, "Microfluidic production of multiple emulsions," *Micromachines,* vol. 8, no. 3, p. 75, 2017.

[92] S.-Y. Teh, R. Lin, L.-H. Hung, and A. P. Lee, "Droplet microfluidics," *Lab on a Chip,* vol. 8, no. 2, pp. 198-220, 2008.

[93] S. Sokic and G. Papavasiliou, "Controlled proteolytic cleavage site presentation in biomimetic PEGDA hydrogels enhances neovascularization in vitro," *Tissue Engineering Part A,* vol. 18, no. 23-24, pp. 2477-2486, 2012.

[94] J. Guzowski, P. M. Korczyk, S. Jakiela, and P. Garstecki, "The structure and stability of multiple micro-droplets," *Soft Matter,* vol. 8, no. 27, pp. 7269-7278, 2012.

[95] T. Trantidou, Y. Elani, E. Parsons, and O. Ces, "Hydrophilic surface modification of PDMS for droplet microfluidics using a simple, quick, and robust method via PVA deposition," *Microsystems & nanoengineering,* vol. 3, no. 1, pp. 1-9, 2017.

[96] S. Seiffert, J. Dubbert, W. Richtering, and D. A. Weitz, "Reduced UV light scattering in PDMS microfluidic devices," *Lab on a Chip,* vol. 11, no. 5, pp. 966-968, 2011.

[97] A. Y. Rwei, B. Wang, T. Ji, and D. S. Kohane, "Predicting the tissue depth for remote triggering of drug delivery systems," *Journal of controlled release,* vol. 286, pp. 55-63, 2018.

[98] A. Shah *et al.*, "Focused ultrasound to expel calculi from the kidney," *The Journal of urology*, vol. 187, no. 2, pp. 739-743, 2012.

[99] M. C. Ziskin, "Fundamental physics of ultrasound and its propagation in tissue," *Radiographics*, vol. 13, no. 3, pp. 705-709, 1993.

[100] G. ter Haar and C. Coussios, "High intensity focused ultrasound: physical principles and devices," *International journal of hyperthermia*, vol. 23, no. 2, pp. 89-104, 2007.

[101] G. Canavese *et al.*, "Nanoparticle-assisted ultrasound: A special focus on sonodynamic therapy against cancer," *Chemical Engineering Journal*, vol. 340, pp. 155-172, 2018.

[102] A. Yildirim, N. T. Blum, and A. P. Goodwin, "Colloids, nanoparticles, and materials for imaging, delivery, ablation, and theranostics by focused ultrasound (FUS)," *Theranostics*, vol. 9, no. 9, p. 2572, 2019.

[103] A. A. Atchley and A. Prosperetti, "The crevice model of bubble nucleation," *The Journal of the Acoustical Society of America*, vol. 86, no. 3, pp. 1065-1084, 1989.

[104] B. M. Borkent, M. Arora, and C.-D. Ohl, "Reproducible cavitation activity in water-particle suspensions," *The Journal of the Acoustical Society of America*, vol. 121, no. 3, pp. 1406-1412, 2007.

[105] B. M. Borkent, S. Gekle, A. Prosperetti, and D. Lohse, "Nucleation threshold and deactivation mechanisms of nanoscopic cavitation nuclei," *Physics of fluids*, vol. 21, no. 10, p. 102003, 2009.

[106] M. L. Fabiilli, K. J. Haworth, N. H. Fakhri, O. D. Kripfgans, P. L. Carson, and J. B. Fowlkes, "The role of inertial cavitation in acoustic droplet vaporization," *IEEE transactions on ultrasonics, ferroelectrics, and frequency control,* vol. 56, no. 5, pp. 1006-1017, 2009.

[107] M. Lafond *et al.*, "Unseeded inertial cavitation for enhancing the delivery of chemotherapies: a safety study," *Ultrasound in medicine & biology,* vol. 42, no. 1, pp. 220-231, 2016.

[108] V. F. Humphrey, "Ultrasound and matter--physical interactions," (in eng), *Prog Biophys Mol Biol,* vol. 93, no. 1-3, pp. 195-211, Jan-Apr 2007.

[109] T. Leong, M. Ashokkumar, and S. Kentish, "The Growth of Bubbles in an Acoustic Field by Rectified Diffusion," in *Handbook of Ultrasonics and Sonochemistry*, M. Ashokkumar, Ed. New York: Springer, 2016, pp. 69-98.

[110] M. C. Ziskin, "Fundamental physics of ultrasound and its propagation in tissue," (in eng), *Radiographics,* vol. 13, no. 3, pp. 705-9, May 1993.

[111] W. G. Pitt, G. A. Husseini, and B. J. Staples, "Ultrasonic drug delivery--a general review," (in eng), *Expert Opin Drug Deliv,* vol. 1, no. 1, pp. 37-56, Nov 2004.

[112] E. Stride and C. Coussios, "Nucleation, mapping and control of cavitation for drug delivery," *Nature Reviews Physics,* vol. 1, no. 8, pp. 495-509, 2019/08/01 2019.

[113] R. Manasseh, "Acoustic Bubbles, Acoustic Streaming, and Cavitation Microstreaming," in *Handbook of Ultrasonics and Sonochemistry*, M. Ashokkumar, Ed. New York: Springer, 2016, pp. 33-68.

[114] S. R. Sirsi and M. A. Borden, "State-of-the-art materials for ultrasound-triggered drug delivery," (in eng), *Adv Drug Deliv Rev,* vol. 72, pp. 3-14, Jun 2014.

[115] Z. Izadifar, P. Babyn, and D. Chapman, "Mechanical and Biological Effects of Ultrasound: A Review of Present Knowledge," (in eng), *Ultrasound Med Biol,* vol. 43, no. 6, pp. 1085-1104, Jun 2017.

[116] M. Wan, Ed. *Cavitation in Biomedicine: Principles and Techniques*, 1 ed. Dordrecht: Springer, 2015.

[117] M. R. Bailey, V. A. Khokhlova, O. A. Sapozhnikov, S. G. Kargl, and L. A. Crum, "Physical mechanisms of the therapeutic effect of ultrasound (a review)," *Acoustical Physics,* vol. 49, no. 4, pp. 369-388, 2003/07/01 2003.

[118] K. Ferrara, R. Pollard, and M. Borden, "Ultrasound microbubble contrast agents: fundamentals and application to gene and drug delivery," (in eng), *Annu Rev Biomed Eng,* vol. 9, pp. 415-47, 2007.

[119] T. Boissenot, A. Bordat, E. Fattal, and N. Tsapis, "Ultrasound-triggered drug delivery for cancer treatment using drug delivery systems: From theoretical considerations to practical applications," (in eng), *J Control Release,* vol. 241, pp. 144-163, Nov 10 2016.

[120] A. Yildirim, N. T. Blum, and A. P. Goodwin, "Colloids, nanoparticles, and materials for imaging, delivery, ablation, and theranostics by focused ultrasound (FUS)," (in eng), *Theranostics,* vol. 9, no. 9, pp. 2572-2594, 2019.

[121] J. J. Kwan *et al.*, "Ultrasound-Propelled Nanocups for Drug Delivery," (in eng), *Small,* vol. 11, no. 39, pp. 5305-14, Oct 21 2015.

[122] T. Leong, M. Ashokkumar, and S. Kentish, "The growth of bubbles in an acoustic field by rectified diffusion," *Handbook of ultrasonics and sonochemistry,* vol. 10, pp. 978-981, 2016.

[123] T. D. Khokhlova and J. H. Hwang, "HIFU for palliative treatment of pancreatic cancer," *Journal of gastrointestinal oncology,* vol. 2, no. 3, p. 175, 2011.

[124] K. Al Mahmud, F. Hasan, M. I. Khan, and A. Adnan, "On the Molecular Level Cavitation in Soft Gelatin Hydrogel," *Scientific reports,* vol. 10, no. 1, pp. 1-13, 2020.

[125] O. Vincent, P. Marmottant, S. R. Gonzalez-Avila, K. Ando, and C.-D. Ohl, "The fast dynamics of cavitation bubbles within water confined in elastic solids," *Soft Matter,* vol. 10, no. 10, pp. 1455-1461, 2014.

[126] D. Christensen, *Ultrasonic Bioinstrumentation*. New York: Wiley, 1988.

[127] I. Tzanakis, G. S. B. Lebon, D. G. Eskin, and K. A. Pericleous, "Characterizing the cavitation development and acoustic spectrum in various liquids," *Ultrasonics Sonochemistry,* vol. 34, pp. 651-662, 2017/01/01/ 2017.

[128] A. Bar-Zion *et al.*, "Acoustically detonated biomolecules for genetically encodable inertial cavitation," 2019.

[129] S. Wrenn, S. Dicker, E. Small, and M. Mleczko, "Controlling cavitation for controlled release," in *2009 IEEE International Ultrasonics Symposium*, 2009, pp. 104-107: IEEE.

[130] I. Leibacher, S. Schatzer, and J. Dual, "Impedance matched channel walls in acoustofluidic systems," *Lab on a Chip,* vol. 14, no. 3, pp. 463-470, 2014.

[131] C. K. Sen *et al.*, "Human skin wounds: a major and snowballing threat to public health and the economy," *Wound repair and regeneration*, vol. 17, no. 6, pp. 763-771, 2009.

[132] V. Falanga, "Wound healing and its impairment in the diabetic foot," *The Lancet*, vol. 366, no. 9498, pp. 1736-1743, 2005.

[133] P. Krzyszczyk, R. Schloss, A. Palmer, and F. Berthiaume, "The role of macrophages in acute and chronic wound healing and interventions to promote pro-wound healing phenotypes," *Frontiers in physiology*, vol. 9, p. 419, 2018.

[134] G. C. Gurtner, S. Werner, Y. Barrandon, and M. T. Longaker, "Wound repair and regeneration," *Nature*, vol. 453, no. 7193, pp. 314-321, 2008.

[135] P. Rousselle, M. Montmasson, and C. Garnier, "Extracellular matrix contribution to skin wound re-epithelialization," *Matrix Biology*, vol. 75, pp. 12-26, 2019.

[136] A. J. Singer and R. A. Clark, "Cutaneous wound healing," *New England journal of medicine*, vol. 341, no. 10, pp. 738-746, 1999.

[137] M. M. Santoro and G. Gaudino, "Cellular and molecular facets of keratinocyte reepithelization during wound healing," *Experimental cell research*, vol. 304, no. 1, pp. 274-286, 2005.

[138] A. Vishwakarma *et al.*, "Engineering Immunomodulatory Biomaterials To Tune the Inflammatory Response," *Trends in Biotechnology*, vol. 34, no. 6, pp. 470-482, 2016/06/01/ 2016.

[139] S. D. Milne *et al.*, "A wearable wound moisture sensor as an indicator for wound dressing change: an observational study of wound moisture and status," *International wound journal,* vol. 13, no. 6, pp. 1309-1314, 2016.

[140] M. S. Brown, B. Ashley, and A. Koh, "Wearable technology for chronic wound monitoring: current dressings, advancements, and future prospects," *Frontiers in bioengineering and biotechnology,* vol. 6, p. 47, 2018.

[141] P. Mostafalu, W. Lenk, M. R. Dokmeci, B. Ziaie, A. Khademhosseini, and S. R. Sonkusale, "Wireless flexible smart bandage for continuous monitoring of wound oxygenation," *IEEE Transactions on biomedical circuits and systems,* vol. 9, no. 5, pp. 670-677, 2015.

[142] T. Q. Trung, S. Ramasundaram, B. U. Hwang, and N. E. Lee, "An all-elastomeric transparent and stretchable temperature sensor for body-attachable wearable electronics," *Advanced materials,* vol. 28, no. 3, pp. 502-509, 2016.

[143] R. Rahimi, S. Nikfar, and M. Abdollahi, "Pregnancy outcomes following exposure to serotonin reuptake inhibitors: a meta-analysis of clinical trials," *Reproductive Toxicology,* vol. 22, no. 4, pp. 571-575, 2006.

[144] S. L. Swisher *et al.*, "Impedance sensing device enables early detection of pressure ulcers in vivo," *Nature communications,* vol. 6, no. 1, pp. 1-10, 2015.

[145] S. Ornes, "Inner Workings: Medical microrobots have potential in surgery, therapy, imaging, and diagnostics," *Proceedings of the National Academy of Sciences,* vol. 114, no. 47, pp. 12356-12358, 2017.

[146] J. Troccaz and R. Bogue, "The development of medical microrobots: a review of progress," *Industrial Robot: An International Journal*, 2008.

[147] C. Chautems, B. Zeydan, S. Charreyron, G. Chatzipirpiridis, S. Pane, and B. J. Nelson, "Magnetically powered microrobots: a medical revolution underway?," *European Journal of Cardio-Thoracic Surgery*, vol. 51, no. 3, pp. 405-407, 2017.

[148] K. Belharet, D. Folio, and A. Ferreira, "Simulation and planning of a magnetically actuated microrobot navigating in the arteries," *IEEE Transactions on Biomedical engineering*, vol. 60, no. 4, pp. 994-1001, 2012.

[149] M. Fruchard, L. Arcese, and E. Courtial, "Estimation of the blood velocity for nanorobotics," *IEEE Transactions on Robotics*, vol. 30, no. 1, pp. 93-102, 2013.

[150] X. Yang *et al.*, "Bioinspired neuron-like electronics," *Nature materials*, vol. 18, no. 5, p. 510, 2019.

[151] S. Fusco *et al.*, "Shape-switching microrobots for medical applications: the influence of shape in drug delivery and locomotion," (in eng), *ACS applied materials & interfaces*, vol. 7, no. 12, pp. 6803-6811, 2015/04/01/ 2015.

[152] K. Kalantar-Zadeh *et al.*, "A human pilot trial of ingestible electronic capsules capable of sensing different gases in the gut," *Nature Electronics*, vol. 1, no. 1, p. 79, 2018.

[153] X. Liu *et al.*, "Ingestible hydrogel device," *Nature communications*, vol. 10, 2019.

[154] S. Miyashita, S. Guitron, K. Yoshida, S. Li, D. D. Damian, and D. Rus, "Ingestible, controllable, and degradable origami robot for patching stomach wounds," in *2016 IEEE International Conference on Robotics and Automation (ICRA)*, 2016, pp. 909-916: IEEE.

[155] A. Abramson *et al.*, "An ingestible self-orienting system for oral delivery of macromolecules," *Science*, vol. 363, no. 6427, pp. 611-615, 2019.

[156] M. R. Basar, F. Malek, K. M. Juni, M. S. Idris, and M. I. M. Saleh, "Ingestible wireless capsule technology: A review of development and future indication," *International Journal of Antennas and Propagation*, vol. 2012, 2012.

[157] L. Ricotti *et al.*, "Biohybrid actuators for robotics: A review of devices actuated by living cells," *Science Robotics*, vol. 2, no. 12, p. eaaq0495, 2017.

[158] L. Schwarz, M. Medina-Sánchez, and O. G. Schmidt, "Hybrid biomicromotors," *Applied Physics Reviews*, vol. 4, no. 3, p. 031301, 2017.

[159] D. B. Weibel *et al.*, "Microoxen: Microorganisms to move microscale loads," *Proceedings of the National Academy of Sciences*, vol. 102, no. 34, pp. 11963-11967, 2005.

[160] D. Rus and M. T. Tolley, "Design, fabrication and control of soft robots," *Nature*, vol. 521, no. 7553, p. 467, 2015.

[161] C. Majidi, "Soft Robotics: A Perspective—Current Trends and Prospects for the Future," *Soft Robotics*, vol. 1, no. 1, pp. 5-11, 2013/07/17/ 2013.

[162] W. Hu, G. Z. Lum, M. Mastrangeli, and M. Sitti, "Small-scale soft-bodied robot with multimodal locomotion," *Nature,* vol. 554, no. 7690, p. 81, 2018.

[163] M. Choi, M. Humar, S. Kim, and S. H. Yun, "Step-index optical fiber made of biocompatible hydrogels," *Advanced materials,* vol. 27, no. 27, pp. 4081-4086, 2015.

[164] N. Sood, A. Bhardwaj, S. Mehta, and A. Mehta, "Stimuli-responsive hydrogels in drug delivery and tissue engineering," *Drug delivery,* vol. 23, no. 3, pp. 748-770, 2016.

[165] J.-Y. Sun *et al.*, "Highly stretchable and tough hydrogels," *Nature,* vol. 489, no. 7414, p. 133, 2012.

[166] N. Tejavibulya, Colburn, D.A., Marcogliese, F.A., Yang, K., Guo, V., Chowdhury, S., Stojanovic, M.N., Sia S.K. , "Towards Intradermal Health Monitoring," 2019.

[167] G. M. Xiong *et al.*, "Materials technology in drug eluting balloons: Current and future perspectives," *Journal of Controlled Release,* vol. 239, pp. 92-106, 2016.

[168] S. M. Seedial *et al.*, "Local drug delivery to prevent restenosis," *Journal of vascular surgery,* vol. 57, no. 5, pp. 1403-1414, 2013.

[169] M. Bukka, P. J. Rednam, and M. Sinha, "Drug-eluting balloon: design, technology and clinical aspects," *Biomedical Materials,* vol. 13, no. 3, p. 032001, 2018.

[170] W. A. Gray and J. F. Granada, "Drug-coated balloons for the prevention of vascular restenosis," *Circulation,* vol. 121, no. 24, pp. 2672-2680, 2010.

[171] H. Ang *et al.*, "Drug-coated balloons: Technologies and clinical applications," *Current pharmaceutical design,* vol. 24, no. 4, pp. 381-396, 2018.

[172] K. Katsanos, S. Spiliopoulos, P. Kitrou, M. Krokidis, and D. Karnabatidis, "Risk of death following application of paclitaxel-coated balloons and stents in the femoropopliteal artery of the leg: a systematic review and meta-analysis of randomized controlled trials," *Journal of the American Heart Association,* vol. 7, no. 24, p. e011245, 2018.

[173] Y. P. Clever *et al.*, "Novel Sirolimus–Coated Balloon Catheter: In Vivo Evaluation in a Porcine Coronary Model," *Circulation: Cardiovascular Interventions,* vol. 9, no. 4, p. e003543, 2016.

[174] D. Andreini and D. Trabattoni, "Is the Sirolimus encapsulated balloon a reliable tool for treating the in-stent restenosis?—insights from the SABRE trial," *Journal of thoracic disease,* vol. 10, no. 2, p. 634, 2018.

[175] Y. Liu, M. Pharr, and G. A. Salvatore, "Lab-on-skin: a review of flexible and stretchable electronics for wearable health monitoring," *ACS nano,* vol. 11, no. 10, pp. 9614-9635, 2017.

[176] C. Wang, C. Wang, Z. Huang, and S. Xu, "Materials and structures toward soft electronics," *Advanced Materials,* vol. 30, no. 50, p. 1801368, 2018.

[177] Y. Zhang *et al.*, "Flexible electronics based on micro/nanostructured paper," *Advanced Materials,* vol. 30, no. 51, p. 1801588, 2018.

[178] D. H. Kim and J. A. Rogers, "Stretchable electronics: materials strategies and devices," *Advanced Materials,* vol. 20, no. 24, pp. 4887-4892, 2008.

[179] Y. Tang and J. Yin, "Design of cut unit geometry in hierarchical kirigami-based auxetic metamaterials for high stretchability and compressibility," *Extreme Mechanics Letters,* vol. 12, pp. 77-85, 2017.

[180] J. A. Fan *et al.*, "Fractal design concepts for stretchable electronics," *Nature communications,* vol. 5, p. 3266, 2014.

[181] E. M. White, J. Yatvin, J. B. Grubbs III, J. A. Bilbrey, and J. Locklin, "Advances in smart materials: Stimuli-responsive hydrogel thin films," *Journal of Polymer Science Part B: Polymer Physics,* vol. 51, no. 14, pp. 1084-1099, 2013.

[182] E. A. Turner, M. K. Atigh, M. M. Erwin, U. Christians, and S. K. Yazdani, "Coating and Pharmacokinetic Evaluation of Air Spray Coated Drug Coated Balloons," *Cardiovascular engineering and technology,* vol. 9, no. 2, pp. 240-250, 2018.

Appendix A: Soft medical microrobots: Design components and system integration*

While there has been both scientific and broader popular culture fascination with implantable microscopic robots for more than half a century, initial proof-of-concept technological strategies have only emerged within recent years. This emerging field of medical microrobots (MMRs) encompasses a range of devices on the scale of a few microns to nearly a millimeter, which vary broadly in terms of material composition and intended application, and which travel through the human body and perform designed functions [60, 145, 146]. Such technology could have significant impact in opening up new avenues of diagnostics and therapeutics by allowing for new levels of temporal and spatial precision, such as for sensing and destroying early-stage cell cells or allowing for minimally-invasive methods of addressing blockages in blood vessels [13, 54, 60, 147]. Furthermore, given the growth in the last decade of genetic testing, such devices could be tailored to allow for more active levels of prevention for genetically at-risk populations. Finally, such medical microrobots may allow for delivery in currently challenging-to-reach or privileged areas of the body, most notably beyond the blood-brain barrier and in the eye.

* Material from: Field, *et al.*, Soft medical microrobots: Design components and system integration, *Applied Physics Reviews*, published 2019, AIP Publishing [13.].

A fully functionalized MMR would have (1) the ability for some amount of movement within an environment, with range of mobility dependent on use case; (2) responsiveness to either intrinsic controls tied to physiological sensing capacities or extracorporeal control modalities; (3) a task-specific functionality, such as sensing or delivery; and (4) sufficient biocompatibility, so as to avoid reduced functionality due to a strong immune response (**Fig. 43**). This framework was summarized in a review paper that helped to contextualize design consideration for the work done in Chapters 2 and 3 [13], which highlights the aforementioned four design considerations.

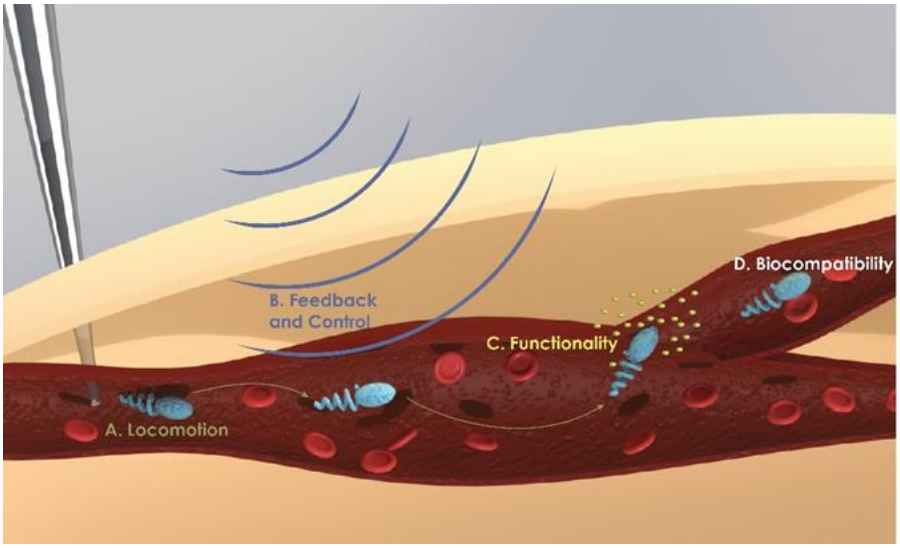

Figure 43: The four design elements to consider to create a fully functionalized MMR. [13]

A.1 Locomotion

Locomotion is perhaps the mostly widely investigated aspect of medical microrobots, with several prior demonstrations relying on magnetic or catalytic propulsion. For movement at

the microscale, devices must operate at low Reynold's number environments and in what are considered time-independent conditions; in these conditions reciprocal motions are ineffective, and motion instead commonly occurs due to nonreciprocal shape changes such as demonstrated by bacterial swimmers [54]. We provide general force balance equation:

$$m\frac{d\boldsymbol{v}}{dt} = F_m + F_d + F_{AW} + F_{vdw} + F_{el} + F_c$$

in which an MMR of mass m has an acceleration $\frac{d\boldsymbol{v}}{dt}$ dependant on the motive force F_m, hydrodynamic drag force F_d, apparent weight force F_{AW}, Van der Waals force F_{vdw}, electrostatic force F_{el}, and contact force F_c [54, 148, 149]. Depending on the intended environment for an MMR, we provide guidance for appropriate assumptions regarding relevant forces in blood vessels of various sizes, along tissue boundaries, and in swarms.

A.2 Feedback and Control

An MMR must respond and adapt to its surrounding environment, by innate internal control, manually-controlled extracorporeal control, or automated extracorporeal control. Common methods for extracorporeal control rely on magnetic, ultrasound, or near-infrared, relevant considerations shown in **Table 18**. Depth of penetration is an important consideration for extracorporeal modalities: both magnetic- and ultrasound-based control modalities, which can rely on MRI machines, permanent magnets, ultrasound transducers, or other equipment, can penetrate deep within the body, with minimal risk to surrounding tissue. Material responsiveness also corresponds to control modalities, with magnetic extracorporeal control modalities

particularly dependent upon responsive material, and on the density of responsive material, within the MMR. Intrinsic control mechanisms typically rely on material responsiveness to surrounding environment, such as swelling-based release due to pH or temperature changes.

Modality	*Magnetic*	*Ultrasound*	*Near-infrared (via photothermal effect)*
Depth of penetration	>100 mm [14]	100 mm [19]	Up to 100 mm, but dependent on tissue type [21]
Resolution ($x \times y$)	1 × 1 mm is standard at 3 T from MRI machine, for depths of 30-100 mm [25]	Depends on the depth of penetration, e.g. 40 × 40 μm at a depth of 2.5 mm [26]	Depends on the depth of penetration, e.g. for thicknesses > 1 cm, resolution is 1/5 of thickness [27]
Risk of tissue damage	Heavy metals (e.g. Pt, Au, Ni, Co, and Ag) may be harmful to living cells and tissues [28]	Potential tissue deformation and damage [18, 29, 30]; heavy metals may be harmful to living cells and tissues [28]	Risk for tissue damage due to resulting hyperthermia [31]
Capital equipment	Permanent magnet, electromagnet system, or MRI machine [32-34]	Ultrasound transducer	NIR light integrated laser system
Responsive materials	Magnetic, e.g. Ni, Co, or Fe coating, nanowires, or NPs [28]	Asymmetric geometry, to enable acoustophoresis [35, 36]; thermoresponsive materials [37]	Thermoresponsive material embedded with NIR-sensitive nanomaterials e.g., gold or carbon nanomaterials [31]
Limitations	Lack of biodegradability of magnetic NPs; potential toxicities due to high concentration of magnetic NPs in localized area; risks associated with very high-powered MRI machines [38]	Maximum speeds can be too low to overcome blood flows [39]; some US-controlled MMRs require fuel for locomotion [40]	Limited demonstrations of biocompatibility and biodegradability of NIR-sensitive nanomaterials [41]; poor resolution [27]

Table 18: Methods of extracorporeal control modalities.

A.3 Functionality

When it reaches a target location, the MMR carries out a function, and we present four typical functions: sensing, drug delivery, cell delivery, and gripping for surgical excision. Most current sensing applications for MMRs occur within *in vitro* applications, such as for detecting analyte concentration based on luminescence or fluorescence concentration, but future *in vivo* sensing applications include as biocompatible electrodes for neural recordings [150]. For therapeutic applications, MMRs have potential applications for both small molecule drug delivery, such as by incorporating drug-loaded responsive hydrogels in the MMR, and for delivery of cells to targeted locations via the blood stream [151]. Finally, MMRs can assist in microsurgeries by grasping tissue, such as for surgical tissue excision [30].

A.4. Biocompatibility

MMRs can be made of different materials. One subset of microelectronic devices and MMRs, such as digestible smart pills ingested through the gut, incorporate silicon-based electronic elements [152-156]. In contrast, another subset comprises biohybrid-based microdevices use living cells as actuation or locomotion elements [157-159]. To minimize immune responses, which reduce effective mobility and functionality, MMRs can be fabricated in soft materials that mimic the moduli of biological materials [160]. These soft materials are deformable (with similar elastic and rheological properties similar to biological tissue), recover their shape after constriction, and are less likely to damage surrounding tissue than rigid devices [161]. Types of soft materials for MMRs include polymers, hydrogels, and proteins [61, 162].

Hydrogels, three-dimensional, crosslinked polymeric networks with a high-water content, are particularly appealing as biocompatible material for MMRS because they are tunable in terms of pore size, diffusivity, and optical properties, among other characteristics [163]; these materials can also be made to be stimuli-responsive [164]. Although their benefits in the past had come at the expense of mechanical robustness, recent developments in composition and fabrication, including works from our group, have enhanced the mechanical properties (including elastic moduli and stretchability) of hydrogel-based structures to diversify their potential use and functionality [32, 165, 166].

Material & device properties	*Effect on scarring*	*Impact of increased scarring on functionality of implanted device*	*Reference*
Stiffness	Softer – reduced scarring	Higher interfacial impedance results in reduced recording and stimulation efficiency of stiff neural electrodes	[4-6]
	Stiffer – enhanced scarring		
Porosity	Porous – less dense scarring	Reduced diffusivity of released cargo, or of sensed analyte (i.e., glucose) by nonporous implantable drug delivery or sensing devices, respectively	[7, 8]
	Nonporous – more dense scarring		
Biodegradability	Biodegradable/faster degradation of implant – reduced scarring	Reduced mass transfer between implants and surrounding tissue can be detrimental to implant functionality	[9-11]
	Non-biodegradable/ slower degradation of implant – enhanced scarring		
Geometry and size	Larger (1.5mm diameter) alginate microspheres – reduced scarring	Reduced duration of blood-glucose control by islet cells encapsulated in smaller alginate spheres compare	[16]
	Smaller (0.5mm diameter) alginate microspheres – enhanced scarring		
	Smaller polyurethane cylinder – reduced scarring	No demonstrated impact, but increased scarring would be detrimental to implant functionality	[8]
	Larger polyurethane cylinders – enhanced scarring		

Table 19: Material considerations in MMR design. [13]

A.5 Integration

While MMRs have thus far largely demonstrated only individual design components [54, 60], and oftentimes only in *in vitro* environments, the integration of propulsion, wireless communication, and biocompatible material selection will expand potential functional applications and facilitate impact of MMRs in the medical field. Furthermore, as machine learning algorithms advance for biological applications, we anticipate that iterative learning algorithms will enable MMRs that “learn” from their environment.

Appendix B: Responsive hydrogel coatings of catheter balloons for peripheral artery disease application

B.1 Introduction

Over the last decade, percutaneous transluminal coronary angioplasty (PTCA) with drug coated balloons (DCBs) has become a common treatment method for coronary artery disease, particularly in small blood vessels (<4 mm diameter). DCBs are typically coated with the antiproliferative drug paclitaxel, which exhibits high lipophilicity and efficient cellular uptake and retention if effectively delivered to a target blood vessel wall [167, 168]. However, current DCBs have significant drug wash off between insertion and reaching the intended use site, allowing the drug to wash into the systemic circulation, thereby risking embolisms and toxicity to other organs [169], and exhibiting an average transfer rate of only 10-15% to the target site [170]. Given recent cytotoxicity concerns [171] and demonstrated increased patient risks [172] associated with balloons coated with the anti-proliferative drug paclitaxel, there is particular interest in a balloon coated with the relatively-minimally lipophilic drug sirolimus, which unfortunately transfers a comparatively low percentage of the drug coating into the vessel tissue wall and even-lower percentage into tissue [173, 174].

The goal of this project was to develop a simple but powerful coating for DCBs that that will enable efficient release of anti-proliferative drugs “on-demand”, i.e., efficient release of the drug when it is desired, and only during the time the release is triggered (**Fig. 44**). Currently,

DCBs rely on diffusion for drug release, leading to the issues of uncontrolled release resulting in off-target toxicity and low on-target drug transfer. In this project, we aimed to integrate two novel technologies – flexible and stretchable electronics and thermo-responsive hydrogels – to fabricate an improved DCB. The active surface would be capable of efficiently discharging small-molecule or antibody-based drugs by thermal trigger. The specific aims of this research were:

[1] To fabricate an advanced drug-releasing balloon catheter with an electronically actuated system consisting of stretchable electronics (that serve as localized heating elements) and thermo-responsive hydrogel membranes.

[2] To demonstrate and characterize drug release from the balloon into an *in vitro* vessel model for coronary artery disease.

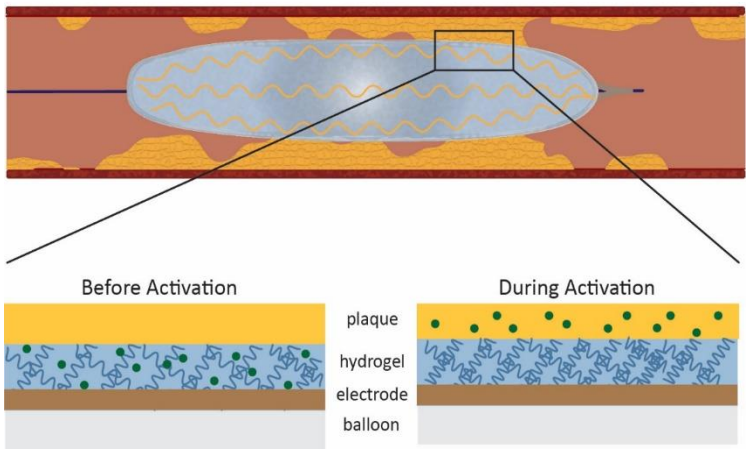

Figure 44: Balloon with electronic activation. Our proposed balloon design has flexible gold electrodes patterned on the balloon surface, as well as a coating of drug embedded in thermo-sensitive hydrogel. Before activation, the drug is encapsulated with the hydrogel layer. However, during activation, the gold electrode acts a heater, raising the local temperature of the hydrogel layer and thereby actively releasing drug into the surrounding tissue.

This project was instrumental for learning hydrogel fabrication techniques, and for exploring methods for integrating electronics and soft polymers for localized drug delivery applications with high spatiotemporal control. It was done in collaboration with the Koh Laboratory at Binghamton University.

B.2 Relevant prior work

B.2.1 Ultrathin, flexible, and stretchable electronics for functional biomedical devices

Soft bioelectronics is a new class of electronics designed to yield conformal contact with human organs, which are curvilinear, soft, wet surfaces of tissue undergoing periodic deformation [175, 176]. Various approaches with material and structural designs have been studied to make substrates not only flexible but stretchable [177]. In addition to using elastomeric polymers (e.g., PDMS) as substrates, the structural design enables non-stretchable materials to absorb the applied strain without fracturing through alteration of the structure of the device. The 2D approach is based on patterning the system with fractal serpentine, wave or wrinkle, origami, and kirigami structures [175, 178-180].

B.2.2. Thermally-responsive polymers

Hydrogels are three-dimensional polymeric network structures which can absorb and retain significant amounts of water [164]. These materials have generated significant attention in the biomedical fields because they are highly biocompatible, capable of high storage capacity,

and responsive to external stimuli such as electric current, pH, or temperature [181]. Researchers have harnessed these material properties to develop a range of hydrogel-based drug delivery devices capable of pulsatile or delayed delivery [62]. Of particular note are thermally-responsive hydrogels that undergo a phase change corresponding to a lower critical solution temperature (LCST): the mesh structure of the hydrogel is in a swollen state when below the LCST, but collapses in on itself when heated above the LCST. When the heated hydrogel contracts, water molecules are expelled alongside small molecules that have been stored within the hydrogel mesh [62]. Therefore, these heat-sensitive hydrogels can be designed to effectively store molecule drugs while below a LCST and to rapidly release the drug when selectively heated.

B.3 Device concept and initial findings

B.3.1. Fabrication of heaters on a balloon catheter

Conventional balloon catheter systems use either polyester or nylon for non-compliant – inflated by pressure, and used for expanding to a specific diameter to open a blockage or dilate vasculature – balloons, or either polyurethane or silicone for compliant – inflated by volume, for applications requiring conforming to anatomy – balloons, respectively, which have all been used as substrate materials for stretchable bioelectronics. In our preliminary results, we fabricated serpentine gold electrodes on a percutaneous transluminal coronary angioplasty (PTCA) catheter using conventional photolithography and transfer printing. Ultrathin gold electrodes insulated with polyimide (PI) can be processed on top of a sacrificial layer coated on a low-surface-energy substrate (e.g., silicon wafer) and the device can be released after processing with conventional

micro-electromechanical system (MEMS) fabrication. After the sacrificial layer of polymethyl methacrylate (PMMA) is removed by dissolving in acetone, the free-standing electrodes were transferred to the balloon catheter substrate. This transfer procedure involves picking up the resulting electrodes with water-soluble tape and integrating them with the polymeric substrate using covalent bonding between the silicon oxide layer on the donor tape and the activated functional group on the polymeric receiver substrate. The sensors were designed to be located on the neutral mechanical plane (NMP) where the active components are not under compression or tension stress, which allows the creation of robust, flexible, and stretchable devices. Thus far, we have not seen a demonstration in literature on printing of electronics on DCBs. We obtained a Mozec percutaneous transluminal coronary angioplasty (PTCA) Balloon Dilation Catheter in 3mm and 3.5mm diameters and 20mm length from Meril Life Sciences. **Figure 45B** shows ultrathin gold electrodes (~1.45 μm thickness) which were laminated on top of inflated balloon catheter, the first such demonstration to our knowledge.

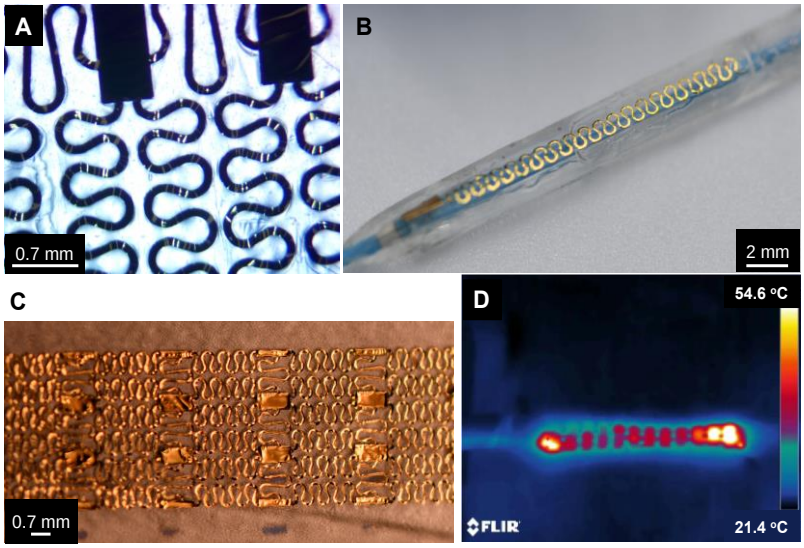

Figure 45: Successful patterning of electronic thermal actuators on balloon catheter. a) Optical images of the microfabricated gold electrodes on the polymetric films (b) Electronics assembled to PTCA balloon catheter. c) Electronics on the water-soluble tape which allow the integration of electronics on a curved surface. d) Thermal IR image of electronically induced thermal actuator. (Image source: Koh Laboratory.)

In our preliminary results, we designed the heater with Peano-based serpentine structures. Theoretically, the Peano curve is capable of achieving 75% uniaxial stretching and >30% biaxial stretching depending on the order of the repeat units per area and unit cell orientation [180]. The photolithographically defined gold electrodes are shown in **Figures 45A** and **45D**. The voltage is applied across a positive temperature coefficient (PTC) resistive heater and then current flows, which begins to heat the part. The heating profile can be modified based on resistivity of the filaments, which can be well tuned by altering thickness, width, and length of conductive parts. The thin metal PTC heater exhibits self-limiting temperature characteristics, thus enhancing the biosafety of the system. In our preliminary results, the micropatterned gold films shows temperature increments up to 142^{o}C under 0.5 V determined by real-time thermal IR camera (**Fig. 45D**).

B.3.2 Balloon coating with hydrogel

The typical coating composition of a DCB incorporates the drug and an excipient, a material intended to assist in the transfer of drug from the balloon surface to the vessel wall; traditionally, excipients have counteracted the hydrophobicity of the drug itself and have assisting in binding drugs to hydrophobic binding sites of vessel walls [171]. These various excipient-based coatings are applied via dipping, micro-pipetting, or spraying; most industrial facilities rely on micro-spraying to produce homogeneously coated DCBs [182]. In our preliminary trials, we employed micro-pipetting techniques to coat nylon balloons with an excipient of thermoresponsive hydrogel and a model drug of fluorescein diacetate.

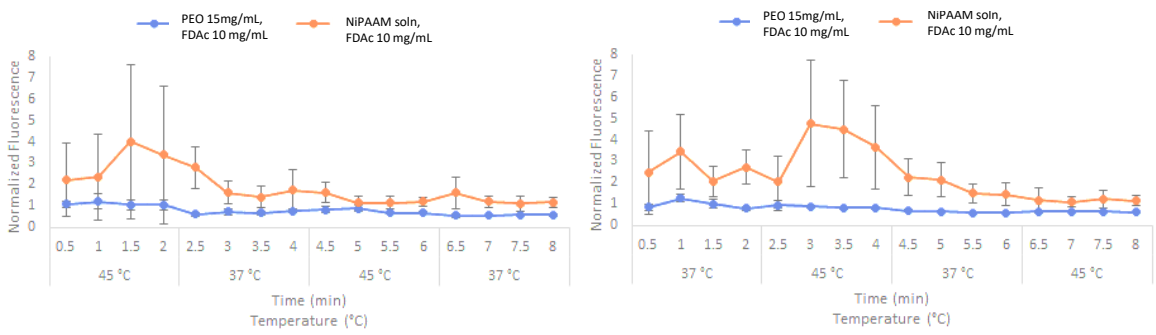

Figure 46: Initial release profiles of FDAC from excipient into surrounding solution, with effect of beginning at 45˚C (left), compared to elevating from body temperature to 45˚C. (n = 10)

We have found that the viscosity of the excipient is a significant factor in successfully applying a coating of homogenous thickness. We have begun to tune the viscosity of the

hydrogel coating, so that it can adhere sufficiently to the nylon balloon's surface. Our initial applications of our experimental coating already have demonstrated significantly increased drug release when heated, as compared to the unheated experimental material and to control coatings of polyethylene glycol (PEO) (**Fig. 46**). While our coating requires additional refinement to ensure homogeneity, these initial experiments support our hypothesis that these materials can be successfully thermally triggered.

B.4 Future work and potential impact

Additional *in vitro* and *in vivo* experimentation would provide demonstration of the DCB's performance with respect to flexibility, coating adhesion, and drug delivery. An *in vitro* testing environment would model how the DCB navigates to distant vessel locations by forcing the balloon to maneuver through narrow and sharply angled channels before reaching the target site. At the target site, our ability to precisely trigger delivery could allow for tuning of the dosage release by the hydrogel, i.e., we can significantly increase the amount of drug delivered to compensate for low lipophilicity of drugs such as sirolimus, without encountering the off-target drug wash-off in passive release systems. The hydrogel-based exterior coating should reduce surface friction between the device and the pathway walls, allowing the balloon to maneuver smoothly. The ideal outcome would be that the balloon successfully navigates the pathway without losing any large particulate, and transfers the significant majority of its drug payload into alginate phantom vessel wall. Pending these results, an eventual *in vivo*

demonstration would measure the effectiveness of this DCB to provide treatment for a vascular disease model of the iliac artery of a New Zealand white rabbit.

A significant advancement in DCBs could bring a fundamental paradigm change for percutaneous coronary interventions, by eliminating the need for permanently implanted devices such as stents. Accordingly, this project has sought to be the first demonstration of a drug-coated balloon with truly on-demand release capacities. This technique differs significantly from current variations on DCBs, which rely on either a simple paclitaxel-excipient solution or, more recently, coatings containing nano-encapsulating carriers. This project provided a preliminary demonstrated of a fundamental change from current DCB technology, from current passive delivery mechanisms that rely primarily on diffusion and hydrophilic excipients to an active delivery mechanism that spatiotemporally controls drug release at the interface between the device and tissue. This DCB with a controllable release mechanism could facilitate the loading of balloons with larger drug dosages, allowing for interventions with improved long-term impacts in terms of maintaining vessel clearance and reducing risks of restenosis and accompanying complications.